REPUBLIC OF TÜRKİYE

YILDIZ TECHNICAL UNIVERSITY

GRADUATE SCHOOL OF SCIENCE AND ENGINEERING

CFD ANALYSIS OF A MISSILE FOR UNMANNED AERIAL VEHICLE

Emine Çağla KIVRAK

MASTER OF SCIENCE THESIS

Department of Chemical Engineering

Chemical Engineering Program

Supervisor

Prof. Dr. Hasan SADIKOĞLU

Co-Supervisor

Assist. Prof. Dr. Özgün YÜCEL

February, 2024

REPUBLIC OF TÜRKİYE

YILDIZ TECHNICAL UNIVERSITY

GRADUATE SCHOOL OF SCIENCE AND ENGINEERING

CFD ANALYSIS OF A MISSILE FOR UNMANNED AERIAL VEHICLE

A thesis submitted by Emine Çağla KIVRAK in partial fulfillment of the requirements for the degree of MASTER OF SCIENCE is approved by the committee on 19.02.2024 in Department of Chemical Engineering, Chemical Engineering Program.

Prof. Dr. Hasan SADIKOĞLU
Yıldız Technical University
Supervisor

Assist. Prof. Dr. Özgün YÜCEL
Gebze Technical University
Co-supervisor

Approved By the Examining Committee

Prof. Dr. Hasan SADIKOĞLU, Supervisor
Yildiz Technical University _____

Doç. Dr. Nil ACARALI, Member
Yildiz Technical University _____

Prof. Dr. Mustafa ÖZİLGEN, Member
Yeditepe University _____

I hereby declare that I have obtained the required legal permissions during data collection and exploitation procedures, that I have made the in-text citations and cited the references properly, that I haven't falsified and/or fabricated research data and results of the study and that I have abided by the principles of the scientific research and ethics during my Thesis Study under the title of "CFD ANALYSIS OF A MISSILE FOR UNMANNED AERIAL VEHICLE" supervised by my supervisor, Prof. Dr. Hasan SADIKOĞLU. In the case of a discovery of false statement, I am to acknowledge any legal consequence.

Emine Çağla KIVRAK

Signature

Dedicated to my family…

ACKNOWLEDGEMENTS

I want to sincerely thank Prof. Dr. Hasan Sadıkoglu, one of my advisors, for his contributions to this work and to my life in general.

From the day I met Assist. Prof. Dr. Özgün YÜCEL during the completion of my master's program, I have been inspired by his experiences and wisdom. His warm personality and expertise serve as an example to me. I am also grateful to my friend Can KARGI, who works at ROKETSAN, for his understanding, support and help.

My mother, Şehbal KIVRAK, my father, Tuncer KIVRAK, and my brother, Volkan KIVRAK, are the three most important people in my life, and I have always felt their financial and moral support. They also patiently helped me, kept me motivated, never skipped prayers and never gave up their rights to me.

My sincerest gratitude.

Emine Çağla KIVRAK

TABLE OF CONTENTS

LIST OF ABBREVIATIONS **xi**
LIST OF FIGURES **xii**
LIST OF TABLES **xvi**
ABSTRACT **xvii**
ÖZET **xix**
1 INTRODUCTION **1**
1.1 Literature Review 1
1.1.1 CFD Analysis of Supersonic Missile Literature Review 2
1.1.2 CFD Analysis of Supersonic Nozzle Literature Review 4
1.2 Objective of the Thesis 5
1.3 Hypothesis 6
2 SUPERSONIC MISSILE AERODYNAMICS **7**
2.1 Definition of Missiles 7
2.2 Newton's Laws 10
2.2.1 The First Law of Newton 10
2.2.2 The Second Law of Newton 10
2.2.3 The Third Law of Newton 11
2.3 Aerodynamic of Supersonic Missiles 11
2.3.1 Lift Coefficient to Drag Coefficient Ratio (C_L/C_D) 12
2.3.2 Missile Mobility 13
2.3.3 Missile Stability 14
2.3.4 Flight Control Systems 16
2.4 Mach Number According to Flow Regimes 18
2.4.1 Subsonic flow 19
2.4.2 Transonic flow 19
2.4.3 Supersonic flow 19
2.4.4 Hypersonic flow 20
3 SUPERSONIC ROCKET ENGINE AND NOZZLES AERODYNAMICS **21**
3.1 Supersonic Rockets Engines and Nozzles 21
3.1.1 Cone Nozzles 23
3.1.2 Bell-Shaped Nozzles 24
3.1.3 Rocket's Flight Performance Criteria 26

3.2 Propulsion Systems 29
3.2.1 Rocket Propulsion Using Chemicals 30
3.2.2 Electric Propulsion Sysrems 35
3.2.3 Solar Thermal Propulsion (STP) 35
4 NUMERICAL MODELLING **36**
4.1 Equations of Governing 36
4.1.1 The Mass Conservation Equation 36
4.1.2 The Momentum Conservation Equation 36
4.1.3 The Energy Conservation Equation 38
4.1.4 Equations for Boundary Layers 38
4.2 Turbulence Models 39
4.2.1 Direct Numerical Simulation (DNS) 40
4.2.2 Large Eddy Simulation (LES) 40
4.2.3 Reynolds Averaged Navier-Stokes (RANS) Equations 40
5 MATERIAL AND METHOD **48**
5.1 CFD Methodology 48
5.1.1 Mesh Generation 49
5.2 Supersonic Missile Geometry Design, Mesh Generation and Performing CFD Analysis 50
5.2.1 Supersonic Missile Design 50
5.2.2 Supersonic Missile Stability Ratio by OpenRocket Tool 52
5.2.3 Supersonic Missile Meshing 53
5.2.4 Performing CFD Analysis for Supersonic Missile Using ANSYS Fluent 56
5.3 Supersonic Nozzle Geometry Design, Mesh Generation and Performing CFD Analysis 65
5.3.1 Supersonic Nozzle Design 65
5.3.2 Supersonic Nozzle Meshing 66
5.3.3 Performing CFD Analysis for Nozzle Using ANSYS Fluent 68
6 RESULTS AND DISCUSSION **73**
6.1 Supersonic Missile Analysis Results 73
6.1.1 Determining Number of Mesh Elements 74
6.1.2 CFD Results 76
6.2 Supersonic Nozzle Analysis Results 109
7 CONCLUSION **121**
REFERENCES **123**

PUBLICATIONS FROM THE THESIS **127**

LIST OF SYMBOLS

a	Acceleration
c_{w1}, c_{w2}	Adjustable Constants
α	Angle of Attack
P_a	Atmospheric Pressure
f_{v1}	Auxiliary Relations
$\overline{u_i'}$	Average Velocity
F_A	Axial Force
I	Bending Point
x, y, z	Carthesian Coordinate Axes
C_G	Center of Gravity
C_P	Center of Pressure
σ_k	Closure Coefficient
J	Conversion Constant
λ	Correction Factor
°	Degree
ρ	Density of the Fluid
∇	Divergence Operator
C_D	Drag Coefficient
D	Drag Force
q_∞	Dynamic Pressure
μ	Dynamic Viscosity of The Fluid
S	Eddy Viscosity Magnitude
V_{eff}	Effective Exhaust Velocity
c_{b1}, c_{b2}	Empirical Constants in The Turbulence Model
E	Energy
A_e	Exit Area
P_e	Exit Pressure
u_i'	Fluctuating Velocity
f	Force
A	Front View Area
g	Gravitational Acceleration
Q_R	Heat of The Combustion Reaction

$\tilde{S}$	Intermediate Variables
n_{int}	Internal Efficiency
Kg	Kilogram
Km	Kilometer
v_T	Kinematic Eddy Viscosity
k	Kinetic Energy
$\boldsymbol{\delta}_{ij}$	Kronecker's Delta
l_{ref}	Reference Length
C_L	Lift Coefficient
L	Lift Force
M*	Linear Momentum
M	Mach Number
$\dot{m}$	Mass Flow Rate
m	Meter
C_M	Moment Coefficient
N_2	Nitrogen
y+	Non-Dimensional Distance from Wall to First Mesh Center
F_N	Normal Force
θ	Nose Angle
α*	Nozzle Cone Divergence Half Angle
O_2	Oxigen
∂	Partial Derivative
Pa	Pascal
%	Percent
m	Pitching Moment
P_{chem}	Power of Chemical Propellants
P_{rocket}	Power of Rocket
Pr	Prandtl Number
S_{ref}	Reference Area
l_{ref}	Reference Length
Re	Reynolds Number
τ_{ij}	Reynolds Stress Tensor
Ω_{Ij}	Rotation Tensor
s	Second
Isp	Specific Impulse

S_{ij}	Strain-Rate Tensor
T	Temperature
3D	Three-Dimensional
T	Thrust Force
~	Tilde
t	Time
β	Turbulence Model Coefficient
ε	Turbulent Dissipation
ω	Turbulent Frequency
σ	Turbulent Prandtl Number
2D	Two-Dimensional
u	Vehicle Speed
u_e	Velocity
u	Velocity in x-Direction
v	Velocity in y-Direction
w	Velocity in z-Direction
$\vec{V}$	Velocity Vector
τ	Viscous Stress Tensor
S	Wing Area
ϕ	Workfunction

LIST OF ABBREVIATIONS

AAM	Air-to-Air Missile
ASM	Air-to-Surface Missile
AoA	Angle of Attack
BVR	Beyond Visual Range
CFD	Computational Fluid Dynamics
CFL	The Courant–Friedrichs–Lewy
DNS	Direct Numerical Solution
HAD	Hesaplamalı Akışkanlar Dinamiği
SI	International System of Units
LES	Large Eddy Simulation
MOGA	Multi-Objective Genetic Algorithm
RANS	Reynolds Average Navier-Stokes
RNG	Re-Normalisation Group
SST	Shear Stress Transport
STP	Solar Thermal Propulsion
SAM	Surface-to-Air Missile
SSM	Surface-to-Surface Missile
TVC	Thrust Vector Control

LIST OF FIGURES

Figure 2.1 AGM-114 Hellfire Missile **8**

Figure 2.2 The AIM 120 AMRAAM Missile **9**

Figure 2.3 The AIM 120 AMRAAM Missile configuration **10**

Figure 2.4 Moments and forces in aerodynamics **12**

Figure 2.5 Pitch, Roll and Yaw axis in a missile **14**

Figure 2.6 Stable missile configuration **16**

Figure 2.7 Conventional missile control system **17**

Figure 2.8 Flow fields with the Mach Numbers **18**

Figure 2.9 Aerodinamic flow diagram **20**

Figure 3.1 Different nozzle configurations and their flow effects **22**

Figure 3.2 Comparing the lengths of several nozzle types **22**

Figure 3.3 Design dimensions for Bell-Shaped and Cone-Shaped nozzles **26**

Figure 3.4 Combustion-Nozzle thrust effect **27**

Figure 3.5 Rocket types according to propulsion systems **30**

Figure 3.6 Chemical rocket structure **31**

Figure 3.7 Solid rocket engine **32**

Figure 3.8 Monopropellant rocket engine **33**

Figure 3.9 Bi-propellant liquid rocket engines **33**

Figure 3.10 Thrust chamber **34**

Figure 5.1 The AIM 120 AMRAAM Missile model **50**

Figure 5.2 AIM 120 AMRAAM missile variation solid model **51**

Figure 5.3 Three-Dimensional view of the fluid environment **52**

Figure 5.4 Supersonic rocket on axis of flight using OpenRocket tool **53**

Figure 5.5 Mesh creation in a fluid environment **54**

Figure 5.6 Mesh creation on missile **54**

Figure 5.7 Distributions of Aspect Ratio and Skewness values belonging to the solution mesh of missile **55**

Figure 5.8 Material properties definition screen for missile in Ansys Fluent **56**

Figure 5.9 Spalart-Allmaras turbulence model settings view for missile in Ansys Fluent **58**

Figure 5.10 k-ω, SST turbulence model settings view for missile in Ansys Fluent **59**

Figure 5.11 k-ε, Realizable turbulence model settings view for missile in Ansys Fluent **60**

Figure 5.12 k-ω, SST solver settings for missile in Ansys Fluent **62**

Figure 5.13 k-ε, Realizable solver settings for missile in Ansys Fluent **63**

Figure 5.14 Spalart-Allmaras solver settings for missile in Ansys Fluent **64**

Figure 5.15 Axi-symmetric nozzle design **65**

Figure 5.16 Nozzle dimensions **66**

Figure 5.17 Mesh generation on nozzle **67**

Figure 5.18 Distributions of Aspect Ratio and Skewness values belonging to the solution mesh of nozzle **68**

Figure 5.19 Material properties definition screen fot nozzles in Ansys Fluent . **69**

Figure 5.20 Solver settings for nozzles in Ansys Fluent **70**

Figure 5.21 k-ω, SST turbulence model settings view for nozzles in Ansys Fluent **71**

Figure 5.22 k-ε, Realizable turbulence model settings view for nozzles in Ansys Fluent **72**

Figure 6.1 The first layer heights of the missile **75**

Figure 6.2 Residual values of angles of attack at Mach 1.5 in the Spalart - Allmaras turbulence model (AoA values; a: 0°, b: 6°, c: 12°, d: 18°) **77**

Figure 6.3 Residual values of angles of attack at Mach 2 in the Spalart-Allmaras turbulence model (AoA values; a: 0°, b: 6°, c: 12°, d: 18°) **78**

Figure 6.4 Residual values of angles of attack at Mach 2.5 in the Spalart - Allmaras turbulence model (AoA values; a: 0°, b: 6°, c: 12°, d: 18°) **79**

Figure 6.5 Residual values of angles of attack at Mach 1.5 in the k-ω, SST turbulence model (AoA values; a: 0°, b: 6°, c: 12°, d: 18°) **80**

Figure 6.6 Residual values of angles of attack at Mach 2 in the k-ω, SST turbulence model (AoA values; a: 0°, b: 6°, c: 12°, d: 18°) **81**

Figure 6.7 Residual values of angles of attack at Mach 2.5 in the k-ω, SST turbulence model (AoA values; a: 0°, b: 6°, c: 12°, d: 18°) **82**

Figure 6.8 Residual values of angles of attack at Mach 1.5 in the k-ε, Realizable turbulence model (AoA values; a: 0°, b: 6°, c: 12°, d: 18°) **84**

Figure 6.9 Residual values of angles of attack at Mach 2 in the k-ε, Realizable turbulence model (AoA values; a: 0°, b: 6°, c: 12°, d: 18°) **85**

Figure 6.10 Residual values of angles of attack at Mach 2.5 in the k-ε, Realizable turbulence model (AoA values; a: 0°, b: 6°, c: 12°, d: 18°) **86**

Figure 6.11 Comparison of the C_D at 0° AoA for the k-ε, Realizable, Spalart-Allmaras, k-ω, SST turbulence models at Mach Numbers 1.5, 2, 2.5 ..... **88**

Figure 6.12 Comparison of the C_D at 6° AoA for the k-ε, Realizable, Spalart-Allmaras, k-ω, SST turbulence models at Mach Numbers 1.5, 2, 2.5 ..... **88**

Figure 6.13 Comparison of the C_D at 12° AoA for the k-ε, Realizable, Spalart-Allmaras, k-ω, SST turbulence models at Mach Numbers 1.5, 2, 2.5 ..... **89**

Figure 6.14 Comparison of the C_D at 18° AoA for the k-ε, Realizable, Spalart-Allmaras, k-ω, SST turbulence models at Mach Numbers 1.5, 2, 2.5 ..... **89**

Figure 6.15 Comparison of the C_L at 6° AoA for the k-ε, Realizable, Spalart-Allmaras, k-ω, SST turbulence models at Mach Numbers 1.5, 2, 2.5 ..... **91**

Figure 6.16 Comparison of the C_L at 12° AoA for the k-ε, Realizable, Spalart-Allmaras, k-ω, SST turbulence models at Mach Numbers 1.5, 2, 2.5 ..... **91**

Figure 6.17 Comparison of the C_L at 18° AoA for the k-ε, Realizable, Spalart-Allmaras, k-ω, SST turbulence models at Mach Numbers 1.5, 2, 2.5 ..... **92**

Figure 6.18 Comparison of the C_M at 6° AoA for the k-ε, Realizable, Spalart-Allmaras, k-ω, SST turbulence models at Mach Numbers 1.5, 2, 2.5 ..... **93**

Figure 6.19 Comparison of the C_M at 12° AoA for the k-ε, Realizable, Spalart-Allmaras, k-ω, SST turbulence models at Mach Numbers 1.5, 2, 2.5 ..... **93**

Figure 6.20 Comparison of the C_M at 18° AoA for the k-ε, Realizable, Spalart-Allmaras, k-ω, SST turbulence models at Mach Numbers 1.5, 2, 2.5 ..... **94**

Figure 6.21 Mach contours of angles of attack at Mach 1.5 in the Spalart-Allmaras turbulence model (AoA values; a: 0°, b: 6°, c: 12°, d: 18°) **96**

Figure 6.22 Mach contours of angles of attack at Mach 2 in the Spalart- Allmaras turbulence model (AoA values; a: 0°, b: 6°, c: 12°, d: 18°) **97**

Figure 6.23 Mach contours of angles of attack at Mach 2.5 in the Spalart-Allmaras turbulence model (AoA values; a: 0°, b: 6°, c: 12°, d: 18°) **98**

Figure 6.24 Mach contours of angles of attack at Mach 1.5 in the k-ω, SST turbulence model (AoA values; a: 0°, b: 6°, c: 12°, d: 18°) **99**

Figure 6.25 Mach contours of angles of attack at Mach 2 in the k-ω, SST turbulence model (AoA values; a: 0°, b: 6°, c: 12°, d: 18°) **100**

Figure 6.26 Mach contours of angles of attack at Mach 2.5 in the k-ω, SST turbulence model (AoA values; a: 0°, b: 6°, c: 12°, d: 18°) **101**

Figure 6.27 Mach contours of angles of attack at Mach 1.5 in the k-ε, Realizable turbulence model (AoA values; a: 0°, b: 6°, c: 12°, d: 18°) **102**

Figure 6.28 Mach contours of angles of attack at Mach 2 in the k-ε, Realizable turbulence model (AoA values; a: 0°, b: 6°, c: 12°, d: 18°) **103**

Figure 6.29 Mach contours of angles of attack at Mach 2.5 in the k-ε, Realizable turbulence model (AoA values; a: 0°, b: 6°, c: 12°, d: 18°) **104**

Figure 6.30 C_L/C_D in the Spalart-Allmaras turbulence model for 6°, 12° and 18° AoA at 1.5, 2, 2.5 Mach numbers **105**

Figure 6.31 C_L/C_D in the k-ω, SST turbulence model for 6°, 12° and 18° AoA at 1.5, 2, 2.5 Mach numbers **106**

Figure 6.32 C_L/C_D in the k-ε, Realizable turbulence model for 6°, 12° and 18° AoA at 1.5, 2, 2.5 Mach numbers **106**

Figure 6.33 C_M/C_D in the Spalart-Allmaras turbulence model for 6°, 12° and 18° AoA at 1.5, 2, 2.5 Mach numbers **107**

Figure 6.34 C_M/C_D in the k-ω, SST turbulence model for 6°, 12° and 18° AoA at 1.5, 2, 2.5 Mach numbers **108**

Figure 6.35 C_M/C_D in the k-ε, Realizable turbulence model for 6°, 12° and 18° AoA at 1.5, 2, 2.5 Mach numbers **108**

Figure 6.36 Residuals values in the the k-ω, SST turbulence model in nozzle (throat width (mm); a: 30, b: 40, c: 50) **110**

Figure 6.37 Residuals values in the the k-ε, Realizable turbulence model in cone nozzles (throat width (mm); a: 30, b: 40, c: 50) **111**

Figure 6.38 Contours of Mach Number in the k-ε, Realizable (a) and k-ω, SST (b) turbulence models in the nozzle with 30 mm throat width **112**

Figure 6.39 Contours of Mach Number in the k-ε, Realizable (a) and k-ω, SST (b) turbulence models in the nozzle with 40 mm throat width **113**

Figure 6.40 Contours of Mach Number in the k-ε, Realizable (a) and k-ω, SST (b) turbulence models in the nozzle with 50 mm throat width **114**

Figure 6.41 Contours of Static Temperature in the k-ε, Realizable (a) and k-ω, SST (b) turbulence models in the nozzle with 30 mm throat width **115**

Figure 6.42 Contours of Static Temperature in the k-ε, Realizable (a) and k-ω, SST (b) turbulence models in the nozzle with 40 mm throat width **116**

Figure 6.43 Contours of Static Temperature in the k-ε, Realizable (a) and k-ω, SST (b) turbulence models in the nozzle with 50 mm throat width **117**

Figure 6.44 Contours of Static Pressure in the k-ε, Realizable (a) and k-ω, SST (b) turbulence models in the nozzle with 30 mm throat width **118**

Figure 6.45 Contours of Static Pressure in the k-ε, Realizable (a) and k-ω, SST (b) turbulence models in the nozzle with 40 mm throat width **119**

Figure 6.46 Contours of Static Pressure in the k-ε, Realizable (a) and k-ω, SST (b) turbulence models in the nozzle with 50 mm throat width **120**

LIST OF TABLES

Table 1.1 C_L/C_D result according to Mach numbers **4**

Table 3.1 Correction factor according to nozzle angle deviation half angle for conical nozzles **24**

Table 5.1 The AIM 120 AMRAAM Missile dimensions **50**

Table 5.2 AIM 120 AMRAAM Missile variation solid model dimensions **52**

Table 5.3 Sembology of C_P and C_G at OpenRocket **53**

Table 6.1 Near wall treatment **74**

Table 6.2 Grid independence **76**

ABSTRACT

CFD Analysis of a Missile for Unmanned Aerial Vehicle

Emine Çağla KIVRAK

Department of Chemical Engineering

Chemical Engineering Program

Master of Science Thesis

Supervisor: Prof. Dr. Hasan SADIKOĞLU

Co- supervisor: Assist. Prof. Dr. Özgün YÜCEL

Understanding object drag in supersonic flows is crucial for fluid mechanics. Energy savings and improved flight and spacecraft performance are both possible with decreased friction. The main aerodynamic coefficients required to assess a missile's performance are drag, lift and moment coefficients. Since CFD analysis is suitable in terms of cost and labor, these coefficients can be evaluated numerically with CFD. Based on the AIM 120 AMRAAM Missile shape, a supersonic missile was constructed for use in unmanned aerial vehicles in this thesis. The lift, moment and drag coefficients, lift/drag ratio and moment/drag ratio were calculated using the k-ω, SST turbulence model, the Spalart-Allmaras turbulence model and the k-ε, Realizable turbulence model with CFD using Ansys Fluent software at 0°, 6°, 12°, and 18° angles of attack at 1.5, 2, 2.5 Mach numbers. The purpose of the analysis for the supersonic missile is to examine the aerodynamic suitability of the designed geometry and to determine the optimum turbulence model. When the results were evaluated, the optimum turbulence model was determined as k-ω, SST turbulence model.

CFD analyses were carried out on the cone nozzle model in the rocket nozzle design. As the rocket nozzle throat diameter decreases, the air becomes more

compressed and Mach number is seen that the increases. If the number of Mach in the rocket nozzle exceeds Mach 4.5, hypersonic flow can be observed in the rocket nozzle. In this thesis, cone nozzles with throat three different diameters which are 30, 40, and 50 mm were created and optimization studies of throat diameters were carried out with CFD analyzes in the k-ε, Realizable turbulence model and k-ω, SST turbulence model. Consequently, CFD research was used to determine the cone nozzles applicability in the supersonic flow domain with a throat diameter of 50 mm.

Keywords: CFD analysis, supersonic missile, supersonic nozzle, ansys fluent, turbulence models

ÖZET

İnsansız Hava Aracı için Tasarlanan bir Füzenin HAD Analizi

Emine Çağla KIVRAK

Kimya Mühendisliği Anabilim Dalı

Yüksek Lisans Tezi

Danışman: Prof. Dr. Hasan SADIKOĞLU

Eş-Danışman: Dr. Öğr. Üyesi Özgün YÜCEL

Akışkanlar mekaniğinde süpersonik akışlarda nesnelerin sürüklenmesinin bilgisi çok önemlidir. Sürtünme azaltılarak uçuş ve uzay araçlarının performansı artırılabilir, enerji tasarrufu sağlanabilir. Bir füzenin performansını değerlendirmek için gereken ana aerodinamik katsayılar; sürükleme, kaldırma ve moment katsayılarıdır. HAD analizi maliyet ve işçilik açısından uygun olduğundan bu katsayılar HAD ile sayısal olarak değerlendirilebilir. Bu çalışmada, AIM 120 AMRAAM Füze şekli esas alınarak insansız hava araçlarında kullanılmak için süpersonik bir füze oluşturulmuştur ve Ansys Fluent yazılımı kullanılarak HAD ile Spalart-Allmaras, k-ω, SST ve k-ε, Gerçekleştirilebilir türbülans modellemelerinde 1.5, 2, 2.5 Mach sayılarında 0°, 6°, 12°, 18° hücum açılarındaki moment, kaldırma ve sürükleme katsayıları, ayrıca kaldırma/sürükleme oranı ve moment/sürükleme oranı hesaplanmıştır. Süpersonik füze için yapılan analizlerdeki amaç, tasarlanan geometrinin aerodinamik uygunluğunu incelemek ve optimum türbülans modelini belirlemektir. Sonuçlar değerlendirildiğinde optimum türbülans modeli k-ω, SST olarak belirlenmiştir.

Roket lüle tasarımında koni nozzle modelinde HAD analizleri gerçekleştirilmiştir. Roket lüle boğaz çapı azaldıkça hava daha fazla sıkışmaktadır ve Mach sayısının arttığı görülmektedir. Roket lülesinde Mach sayısının 4.5 Mach'ı geçmesi durumunda roket lülesinde hipersonik akış gözlenebilmektedir. Bu tezde, boğaz çapı 30 mm, 40 mm ve 50 mm olan koni lüleler tasarlanmıştır ve k-ε, Gerçekleştirilebilir türbülans modeli ve k-ω, SST türbülans modelinde HAD analizleri ile optimizasyon çalışması gerçekleştirilmiştir. Sonuç olarak 50 mm boğaz çapına sahip koni lülenin süpersonik akış rejiminde kullanılabilirliği HAD analizi ile belirlenmiştir.

Anahtar Kelimeler: HAD analizi, süpersonik füze, süpersonik lüle, ansys fluent, türbülans modelleri

1
INTRODUCTION

The global defense sector produces a wide variety of rockets and missiles. Missile types can be customized for a variety of uses, ranging from intercontinental ballistic missiles to short-range cruise missiles [1]. Because combustible chemicals placed at their base propel them, many missiles double as rockets. However, rockets and missiles are designed for different purposes. The distinction between a rocket and a missile lies in the fact that the former is launched towards an object with the specific intention of destroying it. Furthermore, missiles are guided. On the other hand, a rocket is self-propelled, and it can usually be shipped by anything using the flammable material stored inside [2].

Range, speed, and maneuverability are the flight performance metrics used to assess a missile's efficacy. The launch/propulsion mechanism, aerodynamic properties, and environmental circumstances are the primary determinants of a missile's range and speed [1].

Undoubtedly, the primary objective of a missile's aerodynamic design is to achieve high lift coefficient (C_L) and low drag coefficient (C_D). These coefficients can be characterized as the high lift to drag ratio (C_L/ C_D) that is brought about by the dimensions and form of the rocket's body and nose. In addition, the C_L/ C_D is influenced by the size, position, and form of the tail, fins and canards [1].

In order to accomplish a supersonic flow in the missile nozzle, the narrowness of the throat of a cone nozzle and the angle of the termination part also affect the flow and designs must be made according to this purpose.

1.1 Literature Review

In this section, a survey of the literature on studies on CFD analyzes on different flow regimes in missile design and the development of different nozzle designs and CFD analyzes on these nozzles is presented.

1.1.1 CFD Analysis of Supersonic Missile Literature Review

Srivastava, B. (1997) worked on CFD simulations of a missile equipped with lateral jet thrusters for control. At angles of attack ranging from two and twenty-five degrees and Mach number 3.94, three different wing designs were simulated. Both downwind and upwind jet orientations were considered. As a result of the simulations, it was noted that the angles of attack and Mach number were in full accordance with the data of wind tunnel for the physics of the flow around the missile and the performance of the jet interaction, as well as the forces and moments. Low amplification factors were observed for upwind jets due to pressure losses on the upwind surfaces of the jet [3].

Lópeza, D., Domíngueza, D. and Gonzalo, J. (2014) researched into the significance of turbulence modeling in supersonic flow simulations and its impact on the accuracy of results in rocket aerodynamics. The investigation focuses on examining several turbulence models and their influence on the accuracy of external supersonic flow field simulations. Their research aims to provide guidelines for the setup of rocket aerodynamics Computational Fluid Dynamics (CFD) using Reynolds-Averaged Navier–Stokes. The study assesses how well various turbulence models perform, including Spalart–Allmaras, Re-Normalisation Group (RNG) k–ε and Shear Stress Transport (SST) k–ω, for external supersonic flow fields. It includes the analysis of numerical schemes, boundary conditions and time parameters for specific turbulence models. The results show that out of all the models, the SST k–ω model shows the highest degree of concordance with experimental data, making it the most appropriate model for this type of flow [4].

Shah, V. K., Ateeb, K., Razzaq, M., Varun, C. and Avinash, B. (2022) designed at supersonic speeds, nose cone forms are subjected to strong aerodynamic loads in compressible flows, thus moving at different speeds and altitudes for optimum performance. In the research, nose cone shapes were designed as Conical and Ogival, and aerodynamic characteristics such as downflow Mach number, temperature ratio, density ratio, pressure ratio and aerodynamic coefficients in these two nose shapes without being exposed to a certain angle of attack at Mach 2.0 speed were used in the computational fluid dynamics solution method by Ansys. Flow characterization was made using the Fluent program, and the Standard k–ω model with two equations from the RANS turbulence models was chosen to ensure

that the flow was close to the wall. The findings were conceptually contrasted with the notion of oblique shock, and the conclusion confirmed that the oval nose shape had minimum aerodynamic C_D ratio within a deviation of %10 [5].

Meng, Y. S., Yan, L., Huang, W. and Tong, X. Y. (2020) investigated the effect of missile configuration on aerodynamic properties during supersonic flight using CFD numerical methods. The study evaluates two-dimensional and three-dimensional models, focusing on the impact of head shape and slenderness ratio on the C_D. The missile is subjected to powerful shock waves as the Mach number rises from 2 to 4.5 during supersonic flight. As the airflow speed drops, an increase in nose pressure is seen and the C_D ratio correspondingly drops. The research emphasizes that as the Mach number and slenderness ratio increase, the C_D decreases and the stagnation temperature increases. It has also been observed that shock waves and aerodynamic heating create vortices by triggering viscous friction on the missile performance at different angles of attack [6].

Şumnu, A., Güzelbey, İ. H., and Öğücü, O. (2020) focused on the optimizing the aerodynamic form of a missile, specifically the N1G model, using a Multiobjective Genetic Algorithm (MOGA). The study aims to demonstrate the impact of shape optimization on missile performance at supersonic speeds. In this study, the selection of missile models, implementation of Computational Fluid Dynamics (CFD) models, and experimental validation was discussed. Aerodynamic coefficients at 4° and 6° angles of attack (AoA) and supersonic Mach numbers 1.4, 2, and 2.5 were predicted and validated using CFD solutions using three turbulence models: the SST k–ω model, the Realizable k–ε model, and the Spalart-Allmaras model. In this study compared CFD results with existing experimental data, emphasizing the effectiveness of the SST k–ω turbulence model. The results of the optimization process showed that the lift-to-drag coefficient ratio, a critical indicator of missile performance, improved by approximately 11% to 17% with Mach speeds over supersonic. In addition, it presented a detailed analysis of the impact of design variables on drag and lift coefficients, highlighting the major factors influencing the missile's aerodynamic performance. The authors also discussed the Computational Fluid Dynamics (CFD) solutions employed using ANSYS Fluent, as well as the validation of the results and the process of multiobjective optimization in order to attain the necessary aerodynamic

performance. The paper provides detailed findings about the improvements in the C_L/C_D and points to the effectiveness of the optimization process in enhancing missile aerodynamic performance [1]. As a result of the analysis, the C_L/C_D result according to Mach numbers is shown in Table 1.1.

Table 1.1 C_L/C_D result according to Mach numbers [1]

Mach number	**C_L/C_D**
1.4	1.794
2	1.475
2.5	1.411

1.1.2 CFD Analysis of Supersonic Nozzle Literature Review

Foelsch (1949) carried out a study to simplify difficult graphic studies, based on Prandtl and Busemann's method and using analytical methods. In this study, an approach to the configuration of an axially symmetric nozzle that can achieve uniform nozzle exit flow is described. A flat nozzle profile shape was determined by assuming the perturbation approach and the mass flow across each surface in the nozzle as constant. What makes this method advantageous is that it is an analytical solution method [7].

A method for planar two-dimensional nozzle design was developed by A.E. Puckett. An axially symmetric profile can be obtained with this method. In this study, Puckett pointed out that expansion angles smaller than the maximum were possible. According to Puckett, with this method it is longer; However, a nozzle with a smoother exit flow can be obtained. Puckett also hypothesized a radial and uniform flow where the cross-sectional area reaches its maximum slope [8].

Madhu, B. P., Mahendramani G., Bhaskar K., designed nozzles with expansion angles of 9 °, 11 ° and 13 ° and analyzed these nozzles in ANSYS Fluent tool. In this study, they primarily stated that the closest outcomes to the experimental model were provided by the k-ε model. They found that the distance of the first shock

increased with the divergence angle. For nozzles with divergent and conical profiles, the shock formation intensity is higher in those with low divergence angle. A higher Mach number was obtained at the exits of contour nozzles than conical nozzles. It has been stated that there is no shock formation in contour and conical nozzles with a large divergence angle, and more turbulence and flow separation is observed in contour nozzles than in conical nozzles with similar geometry [9].

In the study conducted by Ande, R. and Kumar Yerraboina V. N., the effects of expansion angle on exit Mach number and static pressure were investigated. It has been stated that the entry conditions were obtained through some experimental studies. Expansion angles are taken as 9°, 12°, 15° and 18°, respectively. Analyzes were carried out on these designs and the optimum design was tried to be determined by comparing the analysis results. According to these results, it was stated that the best exit Mach number value was 2.6 Mach for an angle of 15° and as the expansion angle increased, the nozzle's static pressure dropped [10].

In their study, P.P. Nair, A. Suryan and H.D. Kim numerically examined the effects of different conical plug nozzles on flow. One of the nozzles they worked on is a cone nozzle with a cut off top, while the other is a cone nozzle with a pointed tip. In order to compare with experimental data on these nozzles, utilizing the k-ω SST method, which was created for Reynolds-Averaged Navier-Stokes equations, numerical analyses were performed. Boundary conditions for these analyses were established with different nozzle pressure ratios. As a result of the studies, it was determined that the place where the plug used in the nozzle is cut affects the performance of the nozzle. It has been stated that the highest performance is achieved when the flow occurs outside the top of the plug [11].

1.2 Objective of the Thesis

This thesis aims to do the CFD analysis and aerodynamic design of a missile for unmanned aerial vehicle with varying dimensions based on the AIM 120 AMRAAM Missile shape, according to different angles of attack and different Mach numbers, to be used in supersonic flows. In addition, it is also to ensure optimization by designing a supersonic nozzle based on rocket aerodynamic analysis.

In present study, a draft of the missile geometry was firstly created using the OpenRocket program to inspect the suitability of the center of gravity (C_G) and center of pressure (C_P) of the three-dimensional supersonic missile geometry. Afterwards, ANSYS SpaceClaim program was used for the actual designs of the rocket and supersonic nozzle geometry. The mesh structure of the geometries designed in the ANSYS Mesh program was created and prepared for CFD analysis. The mesh structure is generated in 3D for the missile and in 2D for the nozzle. ANSYS Fluent simulation program was used for computational fluid dynamics analysis.

One of the aims of present study, at the end of the analyzes carried out for the missile, the friction, lift and moment forces were calculated according to various Reynolds-Averaged Navier-Stokes turbulence models which are the k-ω, SST, the Spalart-Allmaras and the k-ε, Realizable depending on the attack angles of 0°, 6°, 12°, 18° at Mach numbers 1.5, 2, 2.5 in supersonic flow, and the design was verified according to the most suitable model of turbulence.

The other of the aims of present study, as a result of the analyzes made for the nozzle, the aim is to design a suitable cone shaped nozzle for the designed supersonic missile. In order to capture the supersonic speed at the nozzle outlet, computational fluid dynamics analysis was performed at different throat widths and the k-ω, SST and the k-ε, Realizable Reynolds-Averaged Navier-Stokes turbulence models.

1.3 Hypothesis

This thesis aims to investigate the missile design's aerodynamic characteristics based on the AIM 120 AMRAAM Missile for unmanned aerial vehicle for use in supersonic flows, according to different angles of attack and various supersonic Mach numbers, and to determine the optimum turbulence model.

Additionally, it is aimed to achieve optimization by designing a supersonic nozzle based on missile aerodynamics analysis.

2
SUPERSONIC MISSILE AERODYNAMICS

2.1 Definition of Missiles

The defense and aerospace industries depend heavily on missiles, and several studies are being conducted to advance missile aerodynamics and technology. Because combustible chemicals placed at their base propel them, many missiles double as rockets. However, the intended uses of rockets and missiles are different. The distinction between a rocket and a missile is that a missile is something fired at an object for a specific goal and intended to destroy it. In addition, missiles have a guidance. On the other hand, a rocket is self-propelled, and it can usually be shipped by anything using the flammable material stored inside [2].

The effectiveness of rockets is determined by three flight performance criteria: maneuverability, speed, and range. The launch/propulsion mechanism, aerodynamic properties and environmental circumstances are the primary determinants of a missile's range and speed [1].

Rocket and missile science began in 1687 when Isaac Newton published her studies on the laws of motion.

The application of rockets is listed as follows [12]:

- Space
- Military (may use missiles or rockets)
- Aircraft propulsion, turbo- and ramjet-rocket engines
- Weather or sounding
- Booster
- Retro-rockets
- Sustainer

A chamber containing a gas under pressure surrounds rockets and missiles. The rocket is propelled in the opposite direction by a tiny aperture at one end of the chamber that lets gas out. Burning propellant gases which can be gaseous, solid, or liquid, or a combination of the three allows rockets and missiles to take off [13].

Missiles have subgroups according to their mission areas. These include [14]:

- Surface-to-Surface Missile (SSM)
- Surface-to-Air Missile (SAM)
- Air-to-Surface Missile (ASM)
- Air-to-Air Missile (AAM)

Each group is also categorized according to range, type of targets captured by the missiles, and mission conditions [14].

AAM and ASM, generally described as short-range with ranges of less than 25 km, are usually fired from an aircraft. Air-launched systems such as the IRIS-T missile produced by Diehl BGT Defense [15], the AIM 9X missile produced by Raytheon [16], the AGM-114 Hellfire missile (Figure 2.1) produced by Lockheed Martin [17] and the Brimstone missile produced by MBDA [18] include Thrust Vector Control (TVC) which will provide greater agility to attack targets behind the aircraft.



Figure 2.1 AGM-114 Hellfire Missile [19]

Missiles such as the AIM-120 AMRAAM missiles [20] and AIM-7 Sparrow [21] produced by Raytheon used for Beyond Visual Range (BVR) scenarios, which have radar seekers, larger warheads, and larger rocket engines, are medium and long-range AAM missiles and ASM missile systems, and their range exceeds 30 km.

Missile systems such as the Javelin Weapon System missile [22] produced by Raytheon and the Tomahawk missile [23] range produced by Raytheon and General Dynamics are fired from SSM and SAM land vehicles or ships.

Missile groups also have other subcategories related to the range and type of targets the missiles capture.

Beyond Visual Range (BVR) missile systems are the category of missiles operating in the supersonic regime.

BVR missiles are a class of guided missiles that include subcategories of medium and long-range missiles and are systems operating in the supersonic regime with a range of 40 km to 48 km [24]. AIM 120 AMRAAM and Meteor missiles which have radar guidance systems and ramjets that enable it to reach a range of 100 km and a speed of over Mach 4, can be given as examples of these missile systems [25] [26].

The AIM 120 AMRAAM missile was chosen as the basis for the conceptual missile design in this study, as shown in Figure 2.2 and Figure 2.3.



Figure 2.2 The AIM 120 AMRAAM Missile [27]

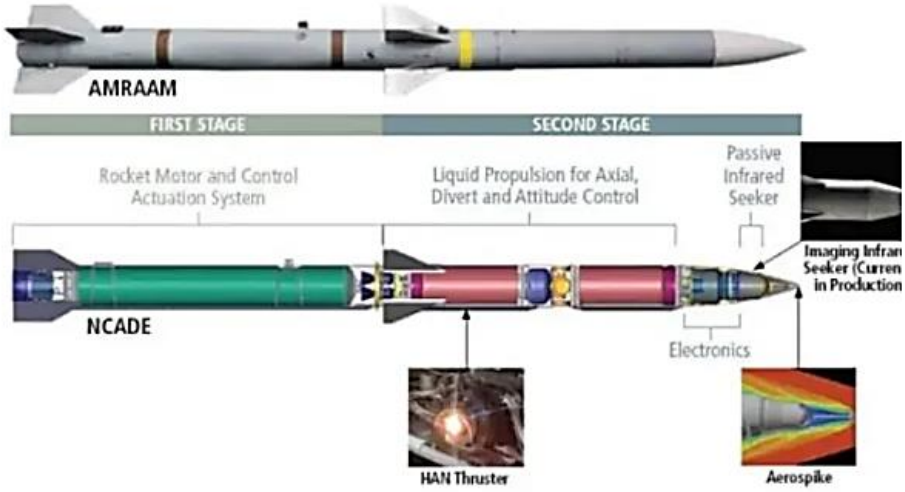


Figure 2.3 The AIM 120 AMRAAM Missile configuration [28]

2.2 Newton's Laws

Rocket science began in 1687 when Isaac Newton published her studies on the laws of motion.

2.2.1 The First Law of Newton

The law of motion is another name for this law, which changes position relative to the environment, ignoring the mobility of all matter in the universe. While the rocket is in a balanced position before flying, it becomes unstable due to the thrust force and the gravitational force when the rocket engine is fired [13].

2.2.2 The Second Law of Newton

This law is the mathematical expression of the law of motion consisting of mass (m), acceleration (a) and force (f) as shown in equation (2.1).

$$f = ma \tag{2.1}$$

The rocket's propulsion force keeps going as long as its engines are ignited and throughout the flight, the mass of the rocket's engines, propellant tanks, payload, control system and propellant gases decreases and accordingly, its acceleration increases [13].

2.2.3 The Third Law of Newton

This law is the law of inertia. When an engine runs out of gas, a rocket will take action, which is the rocket moving in the opposite direction [13].

2.3 Aerodynamic of Supersonic Missiles

Theory of supersonic aerodynamics after World War II, there were many doubts about the possibility of breaking the sound barrier with manned aircraft and the first to break the sound barrier was Chuck Yeager's X-1 aircraft in 1947. Basic theoretical developments regarding fuselages, wings and wing-fuselage combinations are now reviewed for rockets and missiles [29].

The solution for the zero angle of attack (AoA) for a rocket in the supersonic flow solution was revealed by Von Karman and Moore in 1932 [30] and the solution corresponding to the angle of attack was revealed by Tsien in 1938 [31]. AoA is the angle formed by the body on the x-axis during the flight of the rocket.

Supersonic wing flows are generally achieved by superimposing conical flows which is a flow that has constant flow variables along each ray from a vertex.

Aerodynamic parameters used for other aircraft such as planes and jets are used in rockets and missiles, but the fact that they are unmanned and expendable significantly increases the speed, altitude and maneuver range of missiles and causes aerodynamic problems different from other aircraft. For instance, in missiles with high maneuverability, high Mach number and high AoA can cause the change in the aerodynamic coefficient to progress nonlinearly. Additionally, exposure to high linear acceleration may cause high wing loads. Missile bodies generally have cylindrical geometry. Therefore, the slender-body theory and the methods derived from this theory are very useful for missiles [29].

The main aerodynamic parameters evaluated in missiles are lift/drag ratio, stability, maneuverability and control effectiveness.

2.3.1 Lift Coefficient to Drag Coefficient Ratio (C_L/C_D)

(Lift Coefficient)/(Drag Coefficient) ratio is one of the most important parameters that determine missile range. It is the ratio of rocket lift to rocket drag. Equation (2.2) expresses the relationship between the coefficient of axial force and the coefficient of normal force [14]. Figure 2.4 displays the aerodynamic forces and moments [32].

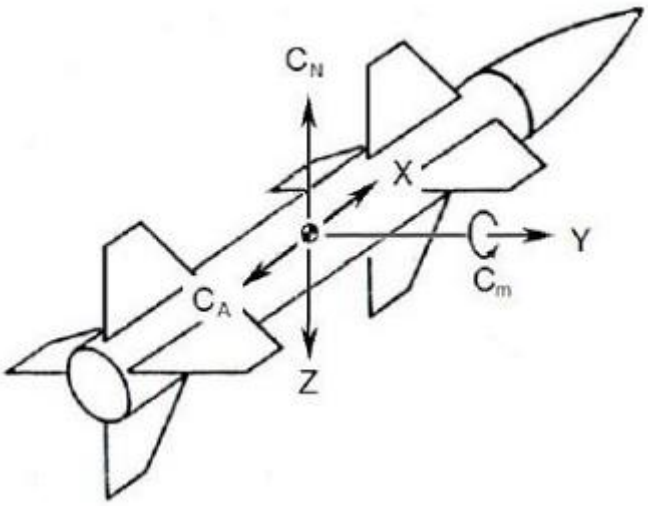


Figure 2.4 Moments and forces in aerodynamics [32]

An object's drag coefficient depends on its shape, Reynolds, and Mach numbers. Equation (2.2) illustrates how the inertia and friction forces acting on an object are connected to the Reynolds number [33].

$$Re = \frac{\rho . u . l}{\mu} \tag{2.2}$$

$$C_A = \frac{F_A}{q_\infty S_{ref}} \tag{2.3}$$

$$C_N = \frac{F_N}{q_\infty S_{ref}} \tag{2.4}$$

$$C_m = \frac{m}{q_\infty S_{ref} l_{ref}} \tag{2.5}$$

$$q_\infty = \frac{1}{2}\rho v^2 \tag{2.6}$$

In Equations (2.3), (2.4), (2.5), (2.6); m is the pitching moment, F_A is the axial force, F_N is the normal force and these are the forces and moment used in performance investigations in this study. q_∞ is the dynamic pressure, S_{ref} is the reference area and l_{ref} is the reference length.

$$C_D = C_N sim\alpha + C_A cos\alpha \tag{2.7}$$

$$C_L = C_N cos\alpha + C_A sim\alpha \tag{2.8}$$

The α specified in Equations (2.7) and (2.8) refers to the angle of attack. According to the Breguet range equation (2.9), rocket range is a function of the C_L/C_D ratio [14].

$$R = (vI_{sp}).\left(\frac{C_L}{C_D}\right).\ln\left(\frac{W_{BC}}{W_{BC} - W_P}\right) \tag{2.9}$$

The cruising speed stated in the equation (2.9), specific thrust, and pre-flight weight and fuel weight, respectively.

2.3.2 Missile Mobility

There are two directions on the Earth which is forwards and backwards. These two directions are named as degrees of freedom. There is a third degree of freedom, which is up and down, according to missiles. It has six degrees of freedom in space.

Considering a linear line, it can be thought the three degrees of freedom (left, right, up, down, forward and backward), in addition objects can also rotate [34].

Usually, the missile can be rotate around the three axes which are yaw (y), pitch (z) and roll (x) axes. When missiles rotate in the vertical axis, it is the yaw which move from up to down on the plane. When missiles rotate in the longitudinal axis moves through the plane from nose to canard and wing, it is pitch. When missiles rotate in the lateral axis passes through the plane from airfoil to airfoil, this axis is roll. Pitch, roll and yaw are commanded by the combustion chamber, canards, fins and the angle of launcher system at the time of firing [35]. The figure of pitch, roll and yaw axis in a missile is given in Figure 2.5.

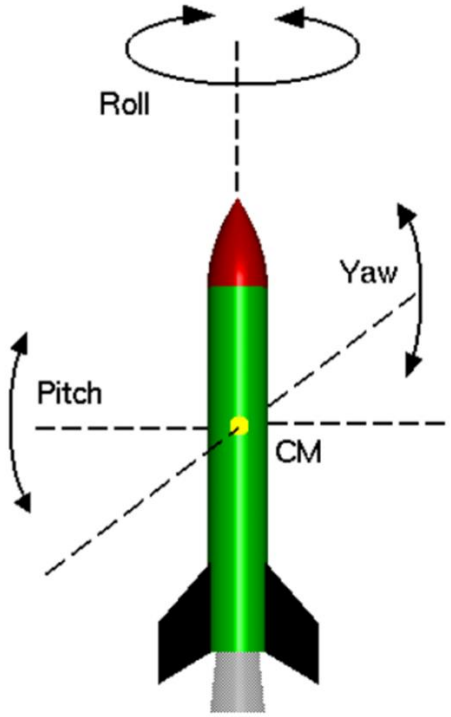


Figure 2.5 Pitch, Roll and Yaw axis in a missile [36]

2.3.3 Missile Stability

A missile has two centers which is the center of gravity (C_G) and the center of pressure (C_P). The center of gravity of a missile is a point of the missile balances. A location in the missile's body's half is known as the center of pressure. The center

of pressure is dissimilar from the center of mass in that case C_P pinpoint is not influenced by inside of the missile which has what parts. C_P position is only affected on the missile's form. On the other hand, center of gravity is too significant for a missile. When a missile is made in unstable, it can be somersault around its center during flight or broken from the nose or fins. When looking from the nose to fins of a missile if the C_G is in front of the C_P, it is stable. On the contrary of this situation, it is unstable [37].

Center of Gravity (C_G) depends on mass generation of missile; Center of Pressure (C_P) depeds on canards and fins of missile.

If designing a missile, it must be stabile which is very significant importance. If any disturbance like wind or turbulance during flight is exposed the missile, this stuation can reason the missile to bend on its oriantation. The missile's centerline and velocity are no longer parallel to one another, which is referred to as flying at an angle of attack (α). An angle of attack is the angle formed by a rocket's velocity vector and centerline [38].

When a missile flies stable at an angle of attack which determines lift to drag force, its canard and fins create a moment force because a missile wants to contuniue its flight properly. The moment produced to correct the missile's flight is created by forces vertical to the axis of the it. The general name of these forces is aerodynamic forces.

The total force point on the missile is defined as the C_P. The corrective moment force is produced only if the C_G is located behind the C_P during missile's flight when flying at a small AoA. If this condition occurs, the missile is statically stable [38]. The stable missile configuration is given in Figure 2.6.

A rocket's stability ratio is computed in calibre and is defined as the separation between the C_P and C_G, where one caliber is obtained by subtracting C_P from C_G which is the maximum diameter of the missile body. This ratio needs to be roughly one to two calibers. Nonetheless, when the angle of attack increases, a missile's C_P usually behaves upward. In case of an angle of attack of only several degrees, 1–2 caliber stability margin might totally evanesce [39].

The dynamic stability of a missile is another stability issue. A missile is aerodinamical stable can still be weak at turn around to the initial alignment of

missile. Model missiles can impact some of dynamic instability which depends on shape, size and mass of the missile [40].

1. Too little oscillation damping: If a missile weight is not enaough heavy, the corrective moment might importantly over-correct that is in the opposite way. In this scenario, there is constant oscillation during flight.

2. Too little time for correction: This oscillation is over-damped, with very little check between the corrective moment and the moment of inertia. The missile was able to adjust its orientation, the engine thrust might have already importantly influenced the flight direction.

3. Roll-pitch coupling: Roll-pitch resonance may arise in the missile design if the usual roll frequency is near the oscillation frequency, causing the design to become unstable.

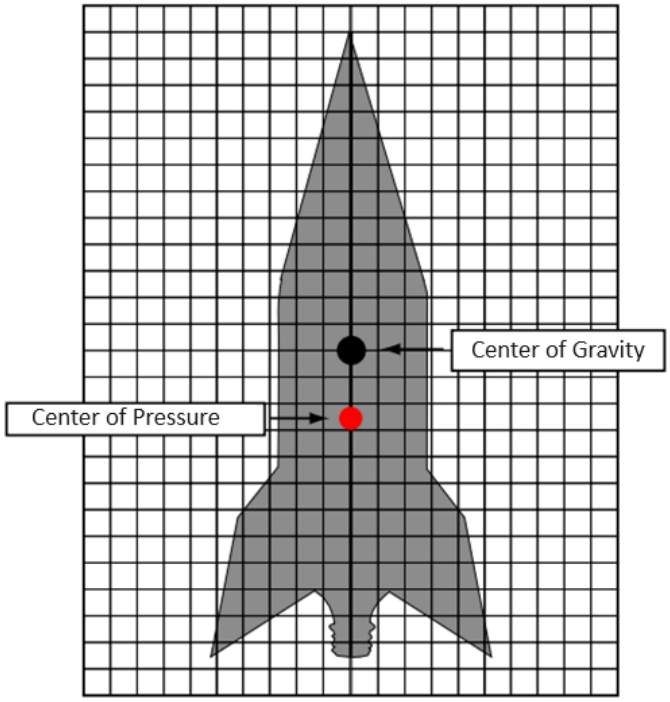


Figure 2.6 Stable missile configuration [37]

2.3.4 Flight Control Systems

Missiles and rockets control their routes during their flights using mechanisms divided into conventional and other control systems. With this kind of control, the aerodynamic control surfaces are deflected in order to create a pressure differential

between their two faces, which in turn generates a force. This pressure difference allows for the control of attitude. Rockets and missiles have three different kinds of control aerodynamic surfaces, depending on the location of the body which are canard, wing and tail. Figure 2.7 depicts these schematically, with wing, canard and tail-controlled missiles arranged from left to right. For a wings-controlled missiles, control panel loads will be greater because the tail must be larger to meet maneuverability requirements. In canard-controlled missiles, owing to the control surfaces' high angle of attack, it may generate a vortex on the missile's fixed lift surfaces in the wing and tail, causing the aft section to roll momentarily. Low control panel loads in tail-controlled missiles will lessen the typical force of a missile in statically stable and prevent the rolling moment from occurring [14].



Figure 2.7 Conventional missile control system [14]

As other control systems, thrust vector control and side jet control can directly produce the desired force even in places where there is no free flow. Thrust vector control is the rocket engine thrust and creates the maneuver component in terms of thrust force vectors. Side jet control, sometimes called lateral (or lateral) jet, response jet, or lateral thruster in the literature, is another type of control system that involves injecting high-pressure, high-speed gases into a free flow in the transverse direction. Faster response and smaller missdistance are achieved inside jet control compared to thrust vector control [14]. Details of the thrust force are given in Chapter 3.

2.4 Mach Number According to Flow Regimes

A Reynolds number in the many tens of millions, which represents the series of magnitudes relating the inertia force to the viscous force, can be used to define aerodynamic flow. When the Reynolds numbers are large, viscous force can be negligible except close to the missile's walls [41].

Aerodynamic flows can also be described in terms of Mach Numbers (M). There are four type of speed regimes that can be identified with Mach numbers. Subsonic, transonic, supersonic, and hypersonic flows are among them in Figure 2.8. The Mach number equation (2.10) is given for compressible gases [33].

$$M = \frac{u}{a} = \frac{u}{\sqrt{k.R.T}} \tag{2.10}$$

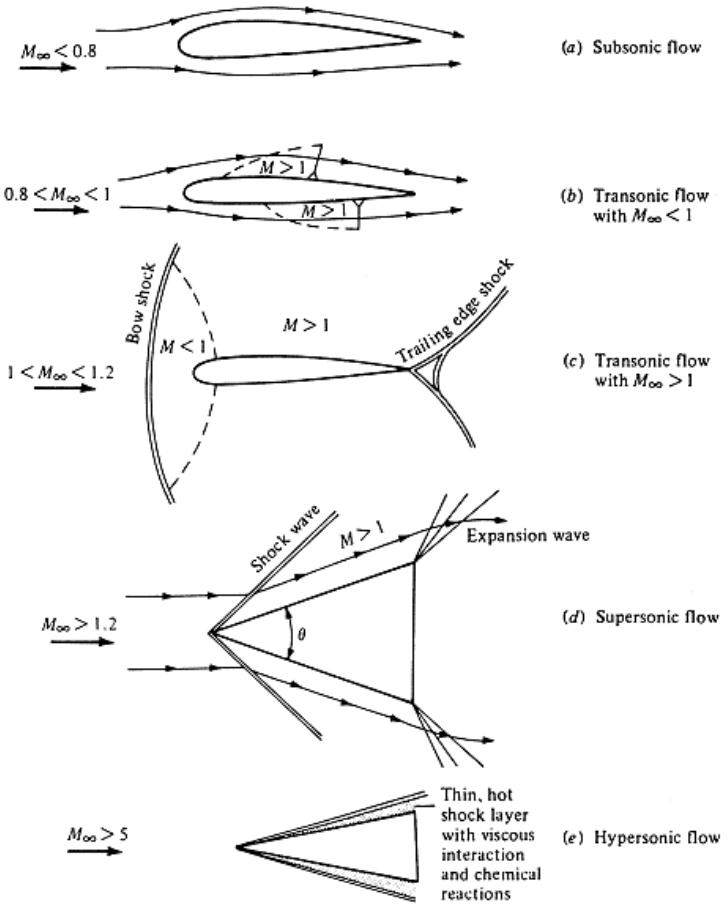


Figure 2.8 Flow fields with the Mach Numbers [42]

2.4.1 Subsonic flow

Subsonic flow regime describes when the Mach number is less than 1 and it is characterized by straight flowlines. In addition, when the velocity of the stream is lower than the sound speed, flow defects increase both upflow and downflow, and the entire stream field is affected [42].

2.4.2 Transonic flow

If Mach number is near to subsonic flow, the stream can turn into supersonic flow. According to Figure (b) supersonic flow across the airfoil's upper and lower planes is putted an end to by impotent shock waves, after this situation the stream get into subsonic flow again. Besides, if Mach number is raised vaguely above 1, a bow shock is occurred in the face of the airfoil which are backward the shock, the stream is subsonic flow as demonstrate in Figure (c). According to Figure (b) and Figure (c) are defined subsonic–supersonic flows and also it is administrated by both types flows which is represent transonic flows become for freestream Mach number $0.8 < M < 1.2$ [42].

2.4.3 Supersonic flow

A flow is considered supersonic if the missile's Mach number exceeds 1 throughout the flow field. In supersonic flows, when streamlines and flow characteristics are continuously changing, shock waves are frequently used to evaluate the flow. This is demonstrated for supersonic flow across a wedge with a pointed nose in Figure (d), where the flow maintains behind the oblique shock wave coming from the tip in its supersonic state. Additionally, different expansion waves common in supersonic flow are also shown in Figure (d). The oblique shock wave does not create a powerful wave when it leaves the wedge tip if the nose angle (θ) is small enough. On the other hand, if θ is made large, it forms a strong wave, and the curves bow of nose cone shock forward the wedge with an important zone of subsonic flow backward the wave.

Consequently, if θ is too large for the number of supersonic vehicles, the completely supersonic flow plotted in Figure (d) is exterminated. Since the local flow speed which is velocity is above sound speed in a supersonic flow, disruptive effects produced at one point in the flow is unable to function upstream. However, subsonic

flows can be affected this situation. It is the main reason, in supersonic flows, shock waves exist, but not in subsonic ones [42].

2.4.4 Hypersonic flow

When the Mach number is high enough, a very thin layer of shock waves forms, and their combined action produces a viscous boundary layer at the surface. Afterwards, the shock layer's temperature increases to a sufficient height to break down O_2 and N_2 molecules in the air. When M is sufficiently large where viscous interplay and/or chemical reactions start to affect the flow which the flow is known hypersonic [42].

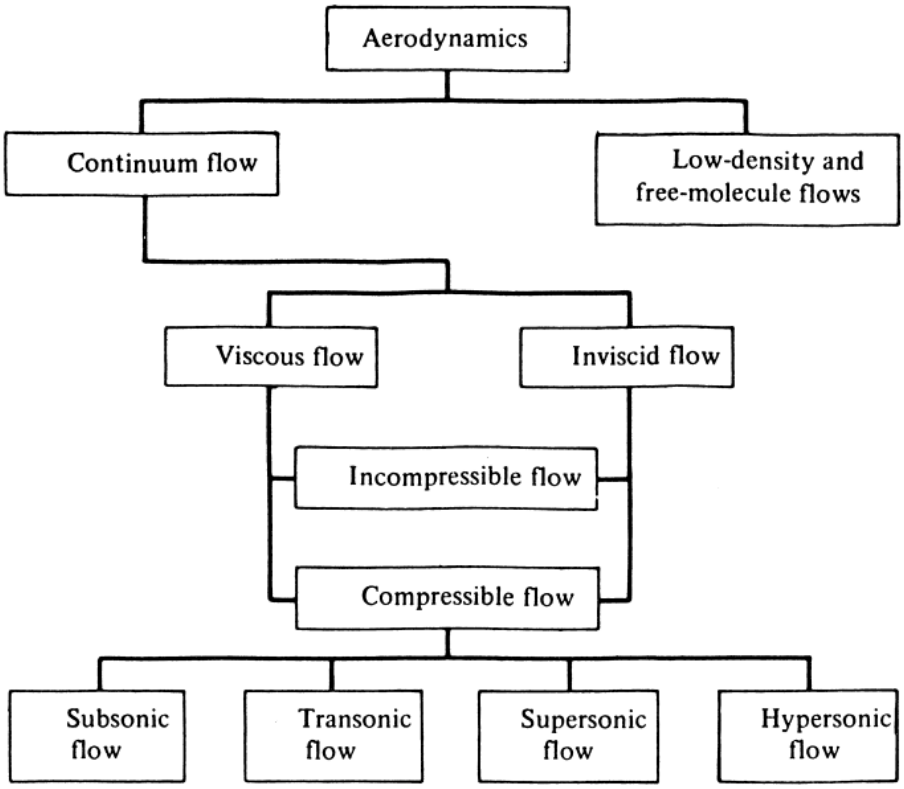


Figure 2.9 Aerodinamic flow diagram [42]

When the aerodynamic design shown in Figure 2.9 is examined, this thesis study was carried out by considering aerodynamic features such as steady flow, viscous flow and compressible flow.

3
SUPERSONIC ROCKET ENGINE AND NOZZLES AERODYNAMICS

3.1 Supersonic Rockets Engines and Nozzles

The high degree of enthalpy conversion into kinetic energy produced by the ratio of the inlet to outlet pressures in the rockets in supersonic flows is what powers supersonic nozzles [43].

Sound is defined as an infinitely small pressure wave and the velocity at which a pressure wave propagates in a medium is referred to as the speed of sound. The nozzle's flow rate and throat speed are unaffected by lowering the exhaust section or outlet pressure, but the nozzle is positioned in the throat rather than the exit plane, the throat width has an influence on the supersonic speed. In the convergent-divergent nozzle, it is not always possible for the fluid used for thrusting to reach supersonic speeds. When designing a nozzle, one of the most basic parameters for the fluid to reach supersonic speeds is how much external pressure or ambient pressure the fluid in question is exposed to near the nozzle's exit. When the operating conditions of the nozzle are exceeded by the ambient pressure, the fluid near the nozzle's exit experiences a slowing down instead of an acceleration [43].

Recently, there are different nozzle configurations that have been proven accurate. The cross-sections of nozzles and chambers are often circular, with a small throat, a divergent cross-section, and a converging cross-section. The nozzles are shown in Figure 3.1.

With extremely little pressure drop and easy rotation at subsonic flow, the part of the nozzle that converges between the nozzle throat and the baffle must be able to handle any shape for the nozzle entrance, wall contour curve, radius, or cone angle. Supersonic nozzle wall surfaces also need to be properly engineered to reduce surface roughness-induced friction, radiation absorption, and convective heat transfer.

Figure 3.1 shows six different nozzle configurations, referred to as cone and bell-shaped nozzles in the first three drawings. The other three offer superior height

correction and have a central stem inside the nozzle. In Figure 3.2, different nozzle types of lengths are compared. A well-designed nozzle layout aims to reduce inert nozzle mass and maximize the practical “Is” value.

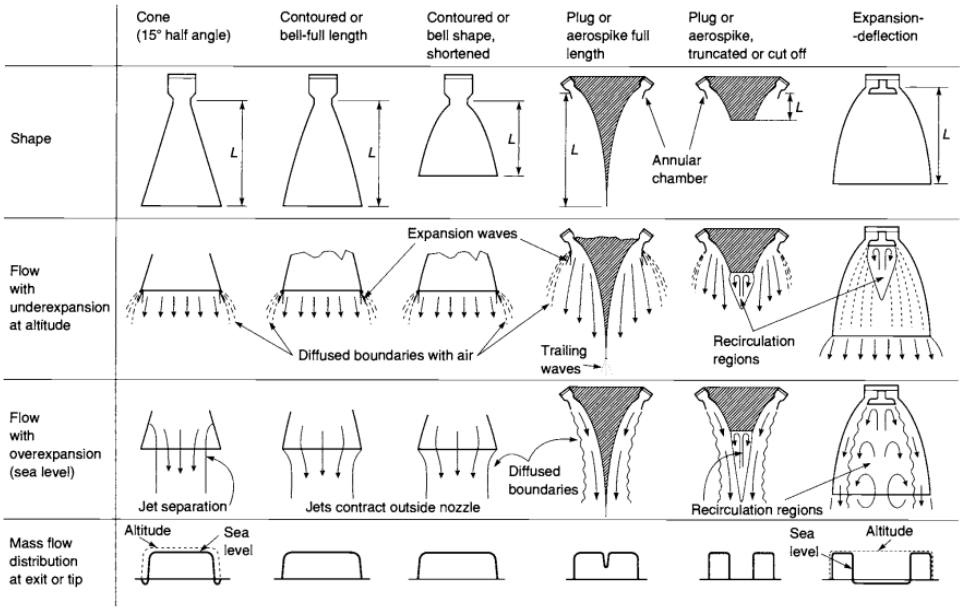


Figure 3.1 Different nozzle configurations and their flow effects [43]

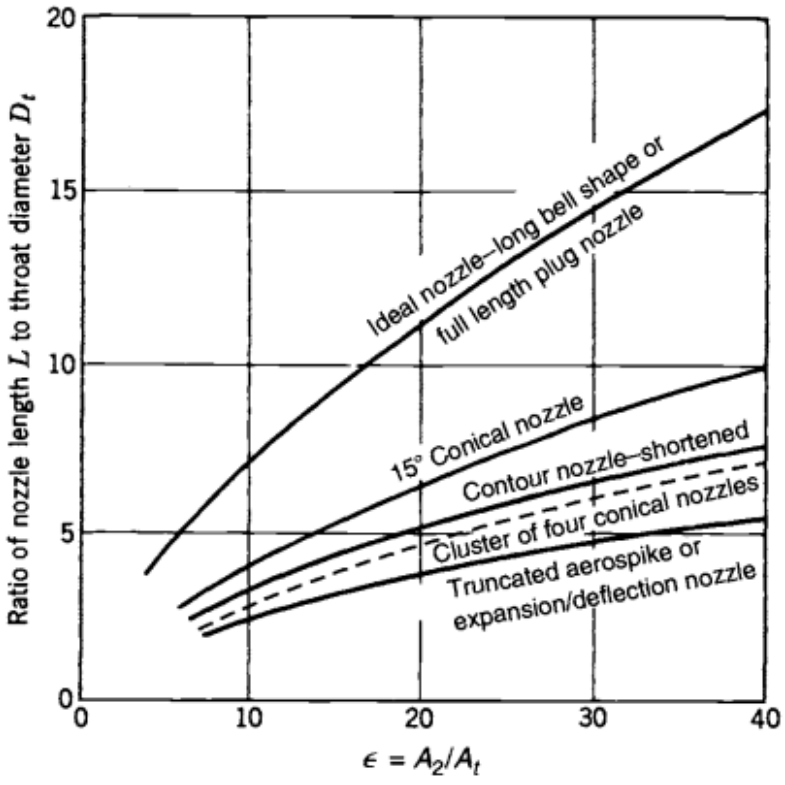


Figure 3.2 Comparing the lengths of several nozzle types [43]

3.1.1 Cone Nozzles

The cone nozzle is still used in many small nozzles today and is described as the oldest and simplest configuration. The optimum rocket's nozzle exit momentum with a conical exhaust nozzle can be used to calculate a theoretical correction factor (λ), which is the proportion of the gases' momentum in a nozzle with a total nozzle angle of the divergent section 2α* and the momentum of an ideal nozzle in which all gases flow in the axial direction. The Correction Factor, λ, corresponding to Nozzle Cone Departure Half Angle, α* (degrees), is in Table 3.1. The formula for this correction factor is as in Equation (3.1). While a small nozzle deflection angle produces a high specific impulse, long nozzle designs and a large deflection angle create disadvantages in terms of, vehicle mass, rocket propulsion system mass and design complexity. The optimum expansion half angle for conical nozzles is between 12 degrees and 18 degrees [43].

$$\lambda = \frac{1}{2}(1 + cos\alpha) \tag{3.1}$$

α is Nozzle Cone Divergence Half Angle and λ is correction factor.

Table 3.1 Correction factor according to nozzle angle deviation half angle for conical nozzles [43]

Nozzle Cone Divergence Half Angle, α* (deg)	Correction Factor, λ
0	1
2	0,9977
4	0,9988
6	0,9972
8	0,9951
10	0,9924
12	0,9890
14	0,9851
15	0,9830
16	0,9806
18	0,9755
20	0,9698

3.1.2 Bell-Shaped Nozzles

Bell-shaped nozzles are the most frequently employed nozzle type today, especially in rocket engines, with a high expansion angle between 20 degrees and 50 degrees after the throat part. Additionally, towards the nozzle's departure, the slope of the nozzle contour can be reversed. Thus, a nozzle expansion half angle of less than 10 degrees can be achieved at the nozzle exit. In these nozzles, flow separation does not occur in the region because high expansion angles occur in the part after the throat. In order to meet this condition, there must be no events such as high relative

pressure, a wide pressure gradient, the working fluid expanding quickly and nozzle contour discontinuities.

Bell-shaped nozzles expand more efficiently under supersonic flow conditions than cone-shaped nozzles because the wall contour of the former is intended to reduce loss. An expansion wave happens when the flow on a thin surface is obliquely angled, the temperature and pressure drop and the flow direction varies slightly and the velocity increases. While the exhaust gas passes through the nozzle throat, it is exposed to the expansion wave that starts from the throat and moves towards point "I" in Figure 3.3, without any energy loss. The flow area grows from the bending point "I" to the nozzle exit "E" and the Contour angle is maximum at the bending position, that is from the throat to point "I". However, the increase in cross-sectional area per length tends to decrease.

The angle at the exit of the last part of the nozzle is a small angle, generally less than 10 degrees, and its purpose is to ensure that the exhaust gas leaves the nozzle with a low deflection loss when leaving the nozzle exit plane. The difference between the angle and the angle of rotation at point "I" and the angle at point "E". Oblique compression waves, which result from reversing the gas flow, are made up of thin surfaces where the flow is twisted, mildly shocked and its velocity actually drops, all of which result in a tiny energy loss. The ratio of the neck to the exit determines the angles at the bending and exit locations. The visual related to these design criteria is as shown in Figure 3.3. In this image, exit angles and nozzle lengths for bell type nozzles are that there is information on what it would be like with a 15 degree semi-angle cone nozzle [43].

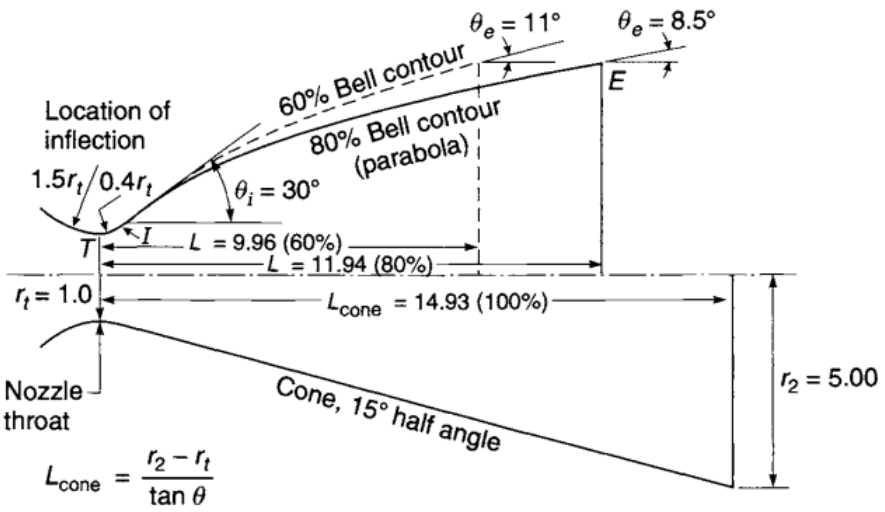


Figure 3.3 Design dimensions for Bell-Shaped and Cone-Shaped nozzles [43]

3.1.3 Rocket's Flight Performance Criteria

Depending on the rocket's intended use, a rocket engine must meet the rocket's flight performance criteria. Rocket performance criteria according to engine are listed as follows [12]:

- Thrust force
- Effective exhaust velocity
- Total impulse
- Thrust coefficient
- Specific impulse
- Characteristic velocity

3.1.3.1 Thrust Force

Thrust is the force that the propulsion system of a rocket produces and is defined as the reaction that the rocket's structure experiences as a result of mass being ejected from the rocket at a high speed [43]. Combustion-Nozzle Thrust Effect is given in Figure 3.4**.**

When evaluating the flow of an ideal rocket, the following presumptions are made [12]:

To analyze the flow in an ideal rocket, the following assumptions are followed:

- The mass flow rate throughout the rocket is a result of the gases in the rocket engine continuously flowing. Every kind of working fluid is a gas. In the nozzle flow, the volume of any condensed phase which is liquid or solid is very small.
- Since there is no heat transfer between the rocket walls, the flow is adiabatic.
- No inlet air is introduced into engines that do not breathe, and the inlet momentum is taken to be zero.

The thrust equation is given in equation (3.2).

$$T = \dot{m}u_e + (P_e - P_a)A_e \tag{3.2}$$

This equation affects the atmospheric pressure (P_a) in addition to the exhaust parameters are pressure (P_e), mass flow rate ($\dot{m}$) and velocity (u_e).

Since the worth of the exit pressure (P_e) is constant for a given nozzle design, the ambient pressure (P_a) continuously decreases during flight and the thrust increases with altitude.

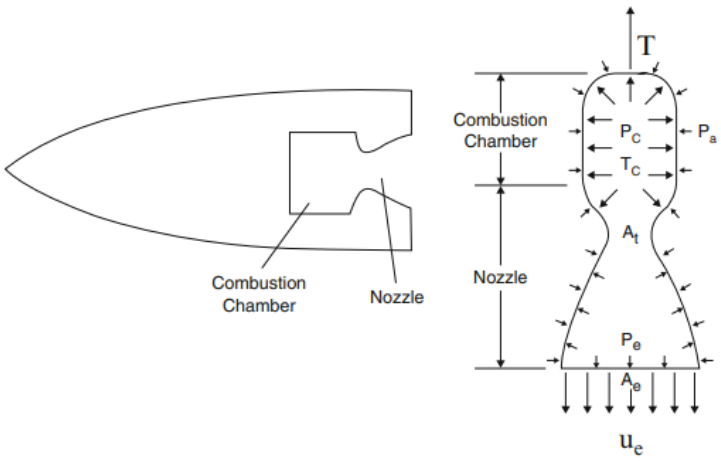


Figure 3.4 Combustion-Nozzle thrust effect [43]

3.1.3.2 Exhaust Velocity Effectiveness (Veff)

Impulse can be related to effective speed.

The mass flow rate is expressed in equation (3.3) and (3.4).

$$T = \dot{m}u_e + (P_e - P_a)A_e = \dot{m}V_{eff} \tag{3.3}$$

Thus;

$$u_e + \frac{(P_e - P_a)A_e}{\dot{m}} = V_{eff} \tag{3.4}$$

3.1.3.3 Energy and Efficiencies

In a propulsion system, there are two different kinds of energy conversion processes which converting stored energy into available energy and then converting it into a form from which a reaction impulse can be received.

It is considered a measure of the mass dissipation of specific power propulsion systems. In rockets with chemical propulsion systems, energy is produced as a result of combustion. The heat of the combustion process, Q_R, is the maximum energy available for chemical propellants per mass unit. The power input of a chemical engine is represented by J, a conversion constant that varies depending on the units employed. The equation for this relationship is given in (3.5). Most of the energy of the exhaust gases cannot be converted into kinetic energy and is separated from the nozzle as enthalpy [43].

$$P_{chem} = \dot{m}Q_R J \tag{3.5}$$

The ratio of the real to the ideal heat of reaction per unit of fuel in chemical rockets is known as combustion efficiency, and it represents between 94% and 99% of the resource efficiency for energy generation [43].

Equation (3.6) defines the power transmitted to the rocket in terms of the vehicle speed u and the propulsion system's thrust force T.

$$P_{rocket} = Tu \tag{3.6}$$

The internal efficiency of a rocket propulsion system is measured by how well the energy input to the system is converted into the kinetic energy of the material being propelled [43]. Internal efficiency can be expressed by equation (3.7).

$$n_{int} = \frac{kinetic\ power\ in\ rocket}{available\ chemical\ power} = \frac{\frac{1}{2}\dot{m}v^2}{n_{comb}P_{chem}} \tag{3.7}$$

3.2 Propulsion Systems

Propulsion systems have three tasks. First of all, they must ensure correct amount of lift force to launch vehicle and its payload, then they carry away from the launcher into the target. Second of all, propulsion systems must provide the payload move around the World. It can insert entering a brief orbit around the Earth or a standing orbit. It is unable to return to the World in this fashion. Maneuvring the cargo into the desired height, location or orbit is the third task. Since the rocket's orbital motion balances the force from gravity and eliminates the need to overcome air resistance, propulsion mechanisms provide a small amount of force or thrust suitable for this third duty. The thrust amount generated by any propulsion system is primarily adjusted exhaust that depends on time and amount leaves the outlet. Specific impulse (Isp) is a measure of a propulsion system's thrust and efficiency when using propellant. The unit of Isp is seconds. Total impulse could be used as a durability metric or in other thinking it is the thrust produced by time and quantity. The entire rocket's thrust is measured by its overall thrust, including the propulsion system and the size of the fuel tanks, since the amount of propellant carried affects the total run time. Propane can be obtained in a variety of ways in order to produce

thrust. The three key techniques are electric propulsion, nuclear reaction propulsion, and chemical reaction propulsion [34].

According to the propulsion system, rockets are examined in two categories as Cruise and Ballistic, as shown in Figure 3.5.

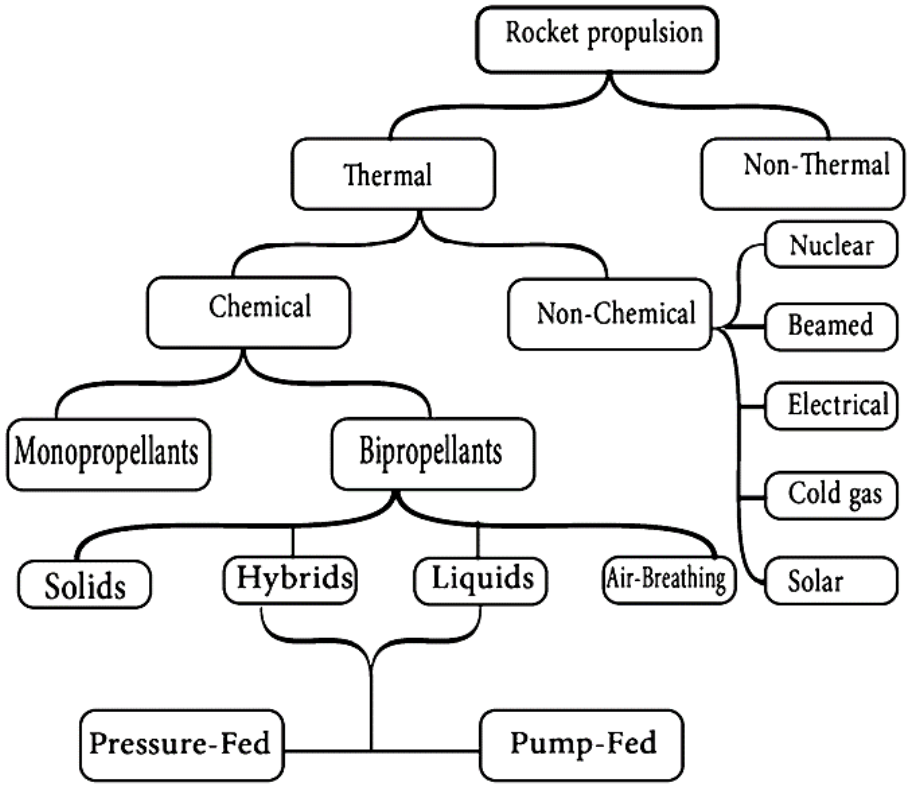


Figure 3.5 Rocket types according to propulsion systems [12]

3.2.1 Rocket Propulsion Using Chemicals

Rocket propulsion using chemicals is the most common method used these days. Chemical propellants are used as solid, liquid or gas in chemical propulsion systems. By using two different types of propellants, this system is called dual propellant. The most suitable propellant chemical types are selected to be used for different purposes and at different ranges. Certain propellants emit harmful gases, while others are difficult to store and unsuitable for extended missions. An oxidizer, which is a component in chemical propellant systems, permits the chemicals to burn or react with the fuel. However, some chemical propellant systems may need a

catalyst to burn before they decompose [34]. Figure 3.6 displays the structure of a general chemical rocket.

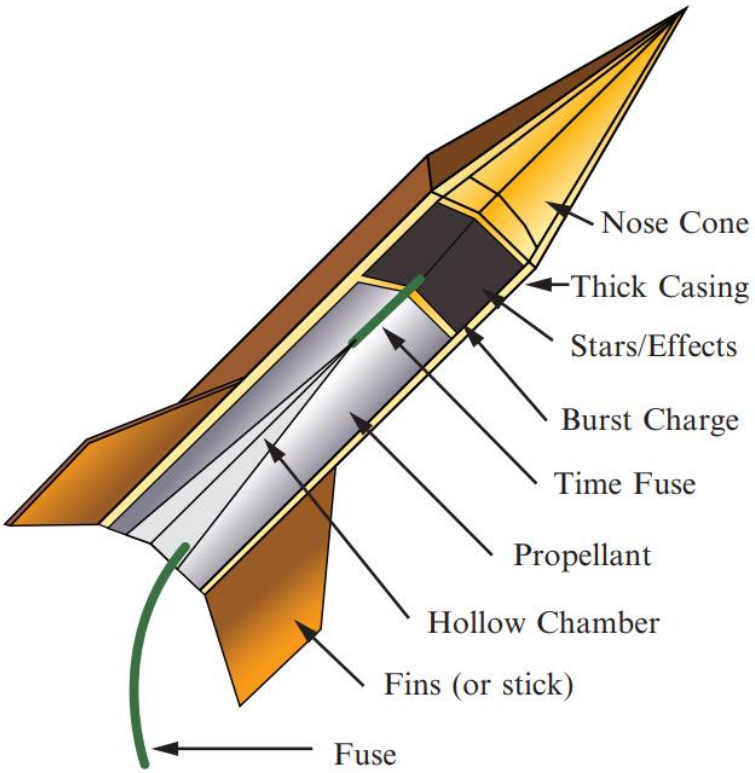


Figure 3.6 Chemical rocket structure [34]

3.2.1.1 Solid Propellants Rocket Motors

Solid propellants have a five to twenty-five year shelf life and are one of the simplest and most widely used rocket propulsion systems that can be easily transported and require an external ignition system. In Figure 3.7 show a cross-section of a firecracker and a simplified solid rocket motor. Two solid rocket engines are mounted on either side of the primary engine of NASA's Space Shuttle, 45 meters long and three meters in diameter, making it's one of the biggest solid-fuel aircraft engines in history [34].

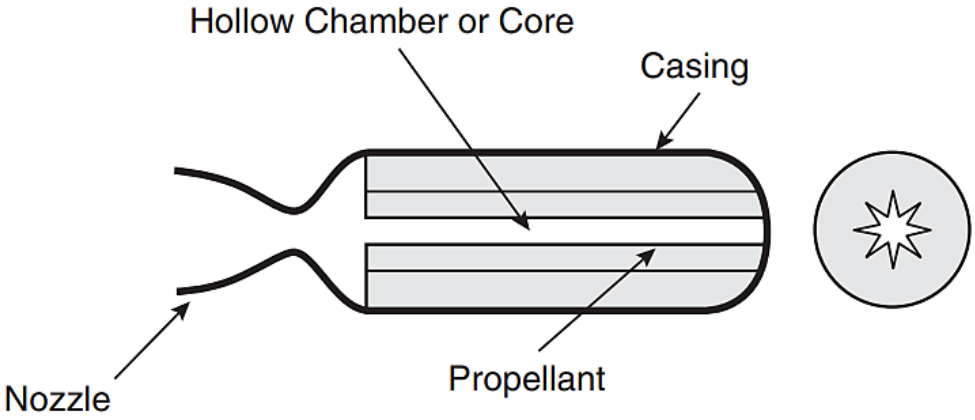


Figure 3.7 Solid rocket engine [34]

3.2.1.2 Rocket Engines with Liquid Propellants

Despite having a more intricate structure than solid rocket engines, liquid fuel engines have many benefits, including the ability to be tested on land prior to launch, the ability to be stored for a maximum of 20 years, the fact that most kinds of liquid fuel engines emit non-toxic exhaust gas and the highest specific impulse power of all propellant systems.

In order for combustion to occur, the propellants are delivered into a combustion chamber via a pressured gas or pump from the rocket's tanks. Systems in which feeding takes place with gas pressure generally have low drive power because they have low total energy. Systems in which feeding is carried out with the help of a pump have higher thrust power due to the presence of larger amounts of propellant gas. Controls are needed for liquid propellant engines in order to fill and empty the propellant and start and stop the engine [34].

- **Monopropellant**

It involves using specific solutions, such as hydrogen peroxide, as the sole fuel in the rocket engine. These liquids can form hot gases through decomposition and decompose into vapor and oxygen using a platinum or silver network catalyst [34]. Figure 3.8 shows the single-fuel rocket engine design.

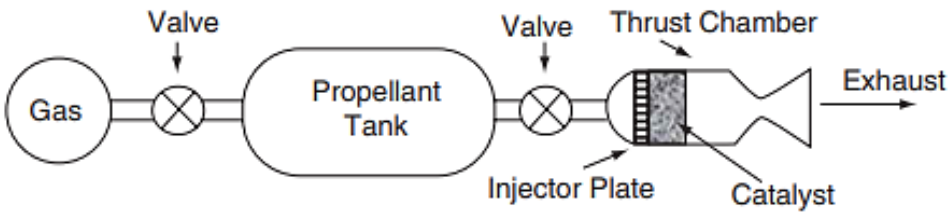


Figure 3.8 Monopropellant rocket engine [34]

- **Bi-propellant**

Dual fuels, such as gasoline, liquid hydrogen, kerosene, and turbojet fuel, which are composed of two distinct liquids “a fuel and an oxidizer”, stored in separate tanks are used in the majority of liquid fuel rocket engines. [34]. Figure 3.9 depicts basic liquid dual-fuel rocket engines that are fed by both pump and pressure.

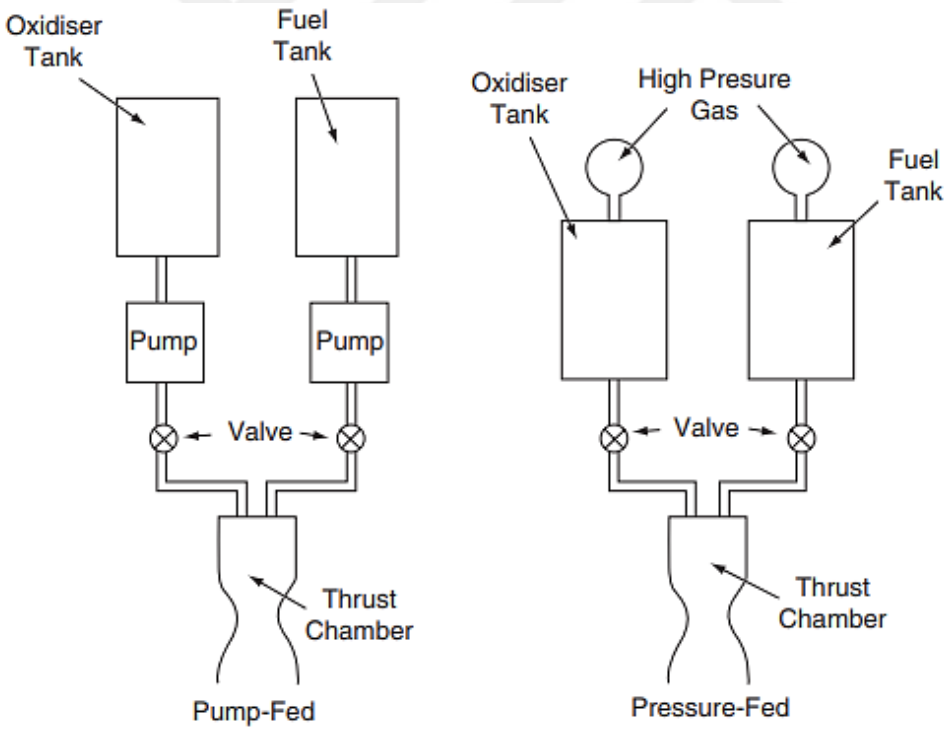


Figure 3.9 Bi-propellant liquid rocket engines [34]

As seen in Figure 3.10, the rocket propulsion chamber is made up of the injector, nozzle and combustion chamber, which is where the fuel and oxidizer combine, ignite and burn. Small pores in the injector plate allow fuel and oxidizer to enter the combustion chamber, separating the liquids into tiny droplets. By narrowing the path that hot gases must take to enter the convergence section, the nozzle's convergent-divergent design allows it to cause the gasses to expand and accelerate to supersonic speeds. In supersonic nozzles, the exhaust gases exit the nozzle at a faster rate than before because they are moving so swiftly through the throat section of the nozzle and because the pressure inside the nozzle is being transformed into kinetic energy [34].

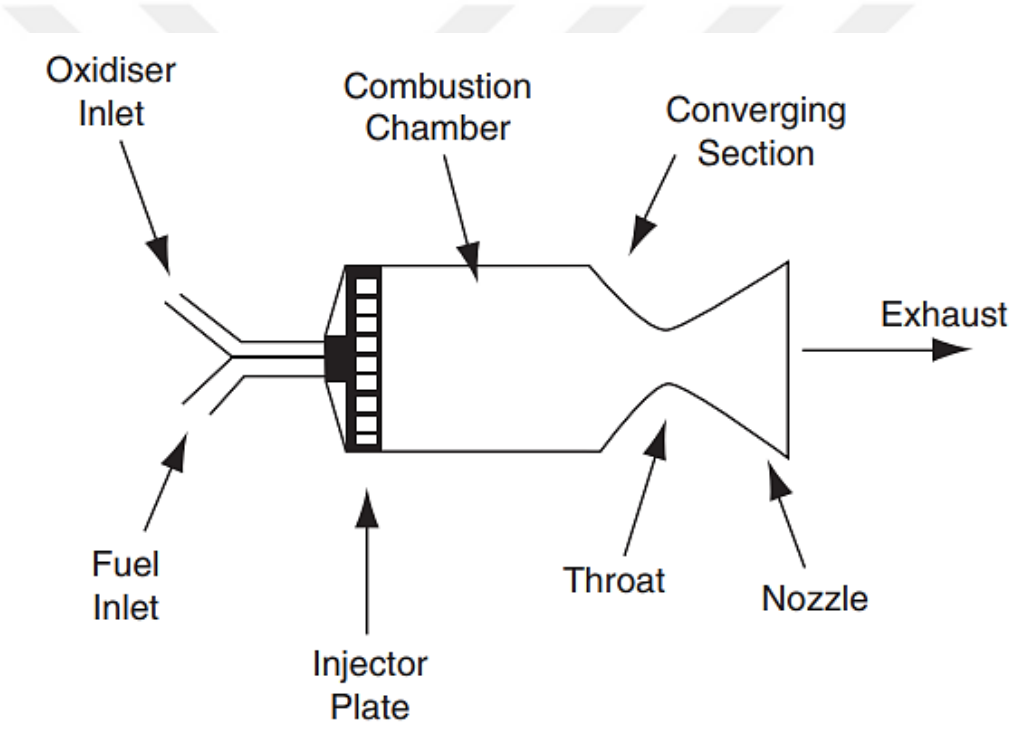


Figure 3.10 Thrust chamber [34]

3.2.1.3 Mixed-Propellant Systems

An example of a hybrid propulsion system is a mixed-propeller system, where the oxidizer is liquid, whereas the fuel is solid. The fuel is ground into a grain, much like in a solid rocket engine and then ignited by an oxidizer. The exhaust that results then passes through a mixing chamber to ensure complete combustion prior to exiting through a nozzle [34].

3.2.2 Electric Propulsion Sysrems

Depending on how the propellant is accelerated, electricity is classified into three main types of propulsion which are thermothermal, electrostatic and electromagnetic, and an electrical power source is required to provide them [34].

3.2.3 Solar Thermal Propulsion (STP)

The relevant propulsion system heats and expands the propellant gases, naturally using the heat coming from the Sun directly [34].

4
NUMERICAL MODELLING

In this chapter, the equations solved by the programs in the background for the Computational Fluid Dynamics (CFD) solutions made in Ansys Fluent, a commercial software program within the scope of the study, are examined.

4.1 Equations of Governing

4.1.1 The Mass Conservation Equation

Equation (4.1) is a general expression of the conservation of mass equation, commonly called the continuity equation. This equation is used during calculation to ensure mass conservation in 2D and 3D models. The mass conservation equation can be written in equation (4.1).

$$\frac{\partial \rho}{\partial t} + \nabla . (\rho V) = 0 \tag{4.1}$$

4.1.2 The Momentum Conservation Equation

The subject called conservation of momentum is also known as second law of Newton in the science of fluid mechanics and is expressed in its most general form in equation (4.2).

$$F = \frac{dM}{dt} = \frac{d(mV)}{dt} = ma \tag{4.2}$$

M is Linear momentum; F is Net force acting on the fluid particle under consideration; a is net acceleration dV/d of the examined fluid particle.

The equation of generalized preservation of momentum with second law of Newton equation and its separate expressions for x, y, z directions are shown in equations (4.3), (4.4) and (4.5).

$$\rho\left[u\frac{\partial u}{\partial x}+v\frac{\partial u}{\partial y}+w\frac{\partial u}{\partial z}\right]=-\frac{\partial p}{\partial x}+\mu\left[\frac{\partial^2 u}{\partial x^2}+\frac{\partial^2 u}{\partial y^2}+\frac{\partial^2 u}{\partial z^2}\right]+\rho g_x \qquad (4.3)$$

$$\rho\left[u\frac{\partial v}{\partial x}+v\frac{\partial v}{\partial y}+w\frac{\partial v}{\partial z}\right]=-\frac{\partial p}{\partial y}+\mu\left[\frac{\partial^2 v}{\partial x^2}+\frac{\partial^2 v}{\partial y^2}+\frac{\partial^2 v}{\partial z^2}\right]+\rho g_y \qquad (4.4)$$

$$\rho\left[u\frac{\partial w}{\partial x}+v\frac{\partial w}{\partial y}+w\frac{\partial w}{\partial z}\right]=-\frac{\partial p}{\partial z}+\mu\left[\frac{\partial^2 w}{\partial x^2}+\frac{\partial^2 w}{\partial y^2}+\frac{\partial^2 w}{\partial z^2}\right]+\rho g_z \qquad (4.5)$$

Equations (4.3), (4.4) and (4.5) are the equations in which the conservation equations of momentum obtained for the assumption of steady and incompressible flow and the states expanded according to x, y, z directions are expressed as partial differentials. These equations are obtained by applying various partial differential equation solution methods mathematically, depending on the type and physics of the flow to be examined.

Navier Stokes equations are used for a Newtonian, incompressible and viscous in equations (4.6).

$$\rho\frac{DV}{Dt}=-\nabla P+\rho g+\mu\nabla^2 V \qquad (4.6)$$

In this equation, ρ refers to fluid density, g gravitational acceleration, μ fluid viscosity, V fluid velocity, t time and P fluid pressure values. Momentum equations for x, y, z directions in steady, compressible and turbulent flows are given in equation (4.7).

$$\rho\vec{B}-\nabla p+\mu\nabla^2\vec{V}+\frac{1}{3}\mu\nabla\left(\nabla.\overrightarrow{V}\right)=\rho\frac{\partial\vec{V}}{\partial t}+\rho\left(\frac{\partial\vec{V}}{\partial t}\right)+\rho\left(\vec{V}.\nabla\right)\vec{V} \qquad (4.7)$$

4.1.3 The Energy Conservation Equation

When viscous forces are greatly outweighed by inertial forces The flow becomes turbulent with high Reynolds numbers and the system's energy conservation equations need to be solved in the proper format. Energy equations can be expressed with the formula given in equation (4.8).

$$\left(\frac{\partial(uE)}{\partial x}+\frac{\partial(vE)}{\partial y}+\frac{\partial(wE)}{\partial z}\right) = -\frac{\partial(uP)}{\partial x}-\frac{\partial(vP)}{\partial y}-\frac{\partial(wP)}{\partial z} + \frac{1}{RePr}\left(\frac{\partial q_x}{\partial x}+\frac{\partial q_y}{\partial y}+\frac{\partial q_z}{\partial z}\right) + \frac{1}{Re}\left(\frac{\partial}{\partial x}\left(u\tau_{xx}+v\tau_{xy}+w\tau_{xz}\right) + \frac{\partial}{\partial y}\left(u\tau_{xy}+v\tau_{yy}+w\tau_{yz}\right)+\frac{\partial}{\partial z}\left(u\tau_{xz}+v\tau_{yz}+w\tau_{zz}\right)\right) \quad (4.8)$$

Density is represented by ρ, pressure by P, viscosity by μ, energy by E, Reynolds number by Re, Prandtl number by Pr and stress tensor by τ.

4.1.4 Equations for Boundary Layers

The Navier-Stokes equations for the thickness of the boundary layer can be reduced and utilized in order to resolve the equations for viscous flow. As boundary layer theory, the equations in these presumptions are obtained. The boundary layer equations, which are shown in equations (4.9) through (4.12), are these [44].

Continuity Equation;

$$\frac{\partial(\rho u)}{\partial x}+\frac{\partial(\rho v)}{\partial y}=0 \quad (4.9)$$

X-Momentum Equation;

$$\rho u \frac{\partial u}{\partial x} + \rho v \frac{\partial v}{\partial y} = -\frac{dP_e}{dx} + \frac{\partial}{\partial y}\left(\mu \frac{\partial u}{\partial y}\right) \tag{4.10}$$

Y Momentum Equation;

$$\frac{\partial P}{\partial y} = 0 \tag{4.11}$$

Energy Equation;

$$\rho u \frac{\partial h}{\partial x} + \rho v \frac{\partial h}{\partial y} = \frac{\partial}{\partial y}\left(k \frac{\partial T}{\partial y}\right) + u \frac{dp_e}{dx} + \mu \left(\frac{\partial u}{\partial y}\right)^2 \tag{4.12}$$

4.2 Turbulence Models

Laminar and turbulent flows are the two types of flows, with the Reynolds number defining the former. Particles frequently move over one another in the laminar flow regime, creating a regular flow. Furthermore, the Navier-Stokes equations and continuity can be used to analytically solve straightforward examples involving laminar flow [45].

In many flows in engineering applications, the interaction between jet and crossflow exhibits turbulent flow behavior. The turbulent flow characteristic is in the three-dimensional velocity vector and the flow has a random behavior with fluctuations that do not move linearly with time. Direct simulations to solve these fluctuations have high computational costs. Because of this, a few numerical techniques have been created to date to be able to seize the significant effects of turbulence. The three categories of these numerical techniques are Reynolds Averaged Navier-Stokes (RANS) Equations, Direct Numerical Simulation (DNS) and Large Eddy Simulation (LES).

4.2.1 Direct Numerical Simulation (DNS)

In the solution process of this numerical modeling, the average flow and all fluctuations are calculated. Since this method causes high computational costs, it is rarely used in today's technology [46].

4.2.2 Large Eddy Simulation (LES)

A bridge between direct numerical simulation and the computation of Reynolds-averaged equations is Large Eddy Simulation (LES). Only the effect of the minimal turbulence scale is calculated in this model. This method is not sufficient to model small eddies and the analyzes are solved as approximations. LES requires fewer meshing elements compared to DNS, but it has high costs for computing meshing elements and is not suitable for engineering applications [46].

4.2.3 Reynolds Averaged Navier-Stokes (RANS) Equations

Turbulence modeling is a fundamental element of Computational Fluid Dynamics (CFD). Using turbulence models that are less precise than real flow, a numerical model that resembles the development of the physical behavior of turbulent flows. In this field, Prandtl, Taylor, and von Karman spent most of their time developing engineering approaches that describe complex physical flows, modeling them, and simplifying mathematical models to avoid complexity [47].

The application of turbulence equations to flow equations began in 1895, as a result of Reynolds' studies in the 19th century, when he applied mathematical expressions of irregularities arising from turbulence effects to the Navier-Stokes equation. Reynolds's research led him to develop the "standard time averaging" turbulence technique, which incorporates the effects of turbulence-induced irregularities into the equations by taking time-dependent averages of these abnormalities. In order to express these irregularities and stresses in a mathematical expression, the terms Bossinesq and eddy viscosity were developed. His studies in the same years led to the growth of the boundary layer approach. In these years, the "mixing length" model, now called the "zero equation model", was developed by Prandtl to calculate the eddy viscosity. It has become increasingly important to be able to express

turbulence-induced irregularities more accurately and put them into mathematical expressions.

For this reason, the effect of eddy viscosities on Prandtl's one equation model, which was established to examine the motion of the fluid particle, was rearranged to be expressed regarding the turbulence wave's kinetic energy oscillations (k). In the 1990s, the zero-equation model was recreated by adding the rate of dissipation (omega) of turbulence energy in relation to time and volume in addition to the turbulence kinetic energy. This resulting equation was brought into a form in which kinetic energy releases and energy dissipation rates were expressed together and began to be called the k-omega (ω) turbulence equation, and over time, this equation was brought into the form of a systematic equation and named "two equation model" [48].

4.2.3.1 One-Equation Models

To resolve specific equations for turbulent transport, such as turbulent kinetic energy, one equation RANS models have been developed. These are the equations that are best known in nuclear and aerospace applications and are widely used by NASA. The most well-known and widely used single-equation models are Baldwin – Barth [49] and Spalart – Allmaras (SA) [50]. The equations of the Spalart – Allmaras model was created and refined for flows through airfoils and wings. This type has many benefits that make it quite popular. An additional equation is required to resolve for the adverse pressure gradient and passing flows for boundary layers.

Spalart-Allmaras Turbulence Model

Three damping functions and eight closure coefficients make up the Spalart – Allmaras model. Its defining equations are in equations (4.13) to (4.20) [50]:

Kinematic Eddy Viscosity:

$$v_T = \tilde{v} f_{v1} \tag{4.13}$$

Kinematic Eddy Viscosity;

$$\frac{\partial \tilde{v}}{\partial t} + U_j \frac{\partial \tilde{v}}{\partial x_j} = c_{b1}\tilde{S}\tilde{v} - c_{w1} f_w \left(\frac{\tilde{v}}{d}\right)^2 + \frac{1}{\sigma}\frac{\partial}{\partial x_k}\left[(v + \tilde{v})\frac{\partial \tilde{v}}{\partial x_k}\right] + \frac{c_{b2}}{\sigma}\frac{\partial \tilde{v}}{\partial x_k}\frac{\partial \tilde{v}}{\partial x_k} \tag{4.14}$$

Closure Coefficients;

$$c_{b1} = 0.1355, c_{b2} = 0.622, c_{v1} = 7.1, \sigma = \frac{2}{3} \tag{4.15}$$

$$c_{w1} = \frac{c_{b1}}{K^2} + \frac{(1 + c_{b2})}{\sigma}, c_{w2} = 0.3, c_{w3} = 2, K = 0.41 \tag{4.16}$$

Auxiliary Relations;

$$f_{v1} = \frac{x^3}{x^3 + c_{v1}^3}, f_{v2} = 1 - \frac{x}{1 + x f_{v1}}, f_w = g\left[\frac{1 + c_{w3}^3}{g^6 + c_{w3}^6}\right]^{1/6} \tag{4.17}$$

$$x = \frac{\tilde{v}}{v}, g = r + c_{w2}(r^6 - r), r = \frac{\tilde{v}}{\tilde{S}K^2 d^2} \tag{4.18}$$

$$\tilde{S} = S + \frac{\tilde{v}}{K^2 d^2} f_{v2}, S = \sqrt{2\Omega_{ij}\Omega_{ij}} \tag{4.19}$$

Rotation tensor;

$$\Omega_{ij} = \frac{1}{2}\left(\frac{\partial U_i}{\partial x_j} - \frac{\partial U_j}{\partial x_i}\right) \tag{4.20}$$

Furthermore, the Spalart-Allmaras model incorporates a transition adjustment that adds two more empirical functions and four more closure coefficients.

4.2.3.2 Two-Equation Models

Two-equation models are generally used to construct two transport equations for two turbulence features, one of which is the kinetic energy of the turbulence (k) and the rate at which its kinetic energy dissipates (ε), also known as the specific distribution ratio (ω) or something similar [51].

This model was first revealed by Kolmogorov and later by Saffmann [52]. Subsequently, Wilcox's [48] modified model proved to be precise for a variety of turbulent flows. Thus, Wilcox's [48] k - ω model could be calculated using the turbulent viscosity equation k and ω.

Researches conducted by Menter in 1992 revealed that velocity and shear stress values closer to reality could be obtained after some innovations in the turbulence viscosity parameters on the previously obtained k-omega turbulence equation [53]. It has been revealed that these innovations directly affect the result in boundary layer flows in a visible way.

The equations of the Two Equation Turbulence Model are given from equations (4.21) to (4.27).

(a_1= 0.3, S = eddy viscosity magnitude, F_2= 0 within outside the boundary layer, F_2= 1 within the subsurface layer).

Two Equation Turbulence Model;

$$R_{i,j} = -\rho\overline{u_i' u_j'} = \mu_T\left(\frac{\partial \bar{u}_i}{\partial x_j} + \frac{\partial \bar{u}_j}{\partial x_i}\right) - \frac{2}{3}\mu_T \frac{\partial \bar{u}_k}{\partial x_k}\delta_{i,j} - \frac{2}{3}\rho k \delta_{i,j} \qquad (4.21)$$

$$\mu_t = a^* \rho \frac{k}{\omega} \qquad (4.22)$$

Dissipation;

$$\varepsilon \sim k^{3/2}/l \tag{4.23}$$

$$\rho \frac{Dk}{Dt} = \tau_{i,j} \frac{\partial \bar{u}_i}{\partial x_j} - \rho \beta^* f_\beta k\omega + \frac{\partial}{\partial x_j}\left[\left(\mu + \frac{\mu_t}{\sigma_k}\right)\frac{\partial k}{\partial x_j}\right] \tag{4.24}$$

$$\rho \frac{D\omega}{Dt} = \alpha \frac{\omega}{t} \tau_{i,j} \frac{\partial \bar{u}_i}{\partial x_j} - \rho \beta f_\beta k\omega^2 + \frac{\partial}{\partial x_j}\left[\left(\mu + \frac{\mu_t}{\sigma_\omega}\right)\frac{\partial \omega}{\partial x_j}\right] \tag{4.25}$$

Reynolds Stress Tensor;

$$\tau_{ij} = 2\mu_T S_{ij} - \frac{2}{3}\rho k \delta_{ij} \tag{4.26}$$

S_{ij} is the mean strain-rate tensor.

Turbulent Transport and Pressure Diffusion;

$$\frac{1}{2}\rho \overline{u_i' u_i' u_j'} + \overline{p' u_i'} = -\frac{\mu_T}{\sigma_k}\frac{\partial k}{\partial x_j} \tag{4.27}$$

σ_k is a closure coefficient.

In CFD simulations, the k–ε model is constantly used as a turbulence model. Extreme turbulent shear stress levels are predicted by this turbulence model, which is known to inhibit separation in reverse pressure gradients [54].

In the near-wall region, the standard k–ω turbulence model outperforms k–ε, but in the far field, it performs worse. For improved performance in remote locations, the

shear stress transfer formulation was created as k–ω, SST. In this thesis, both k–ω, SST and k-ε variant Realizable models were used as two-equation turbulence models used in CFD analyses, and the differences between them were examined.

k–ω, SST Turbulence Model

The k–ω, SST model is a model that solves the analysis using the k–ω turbulence model in areas along the wall and the equations in the k–ε turbulence model in areas distant from the wall. The original k–ω model developed by Wilcox is used in Reynolds stress calculation and k-equations [47], however the ω-equation has a new form developed by Menter, Kuntz, and Langtry [55]. The k–ω, SST model's equations (4.28) through (4.36) are provided.

Viscosity;

$$v_T = \frac{a_1 k}{\max(a_1\omega, SF_2)} \tag{4.28}$$

Kinetic Energy;

$$\frac{\partial k}{\partial t} + U_j \frac{\partial k}{\partial x_j} = P_k - \beta^* k\omega + \frac{\partial}{\partial x_j}\left[(v + \sigma_k v_T)\frac{\partial k}{\partial x_j}\right] \tag{4.29}$$

$$\frac{\partial \omega}{\partial t} + U_j \frac{\partial \omega}{\partial x_j} = \alpha S^2 - \beta\omega^2 + \frac{\partial}{\partial x_j}\left[(v + \sigma_\omega v_T)\frac{\partial \omega}{\partial x_j}\right] + 2(1 - F_1)\sigma_{\omega^2}\frac{1}{\omega}\frac{\partial k}{\partial x_i}\frac{\partial \omega}{\partial x_i} \tag{4.30}$$

$$P_k = min\left(\tau_{i,j}\frac{\partial U_i}{\partial x_j}, 10\beta^* k\omega\right) \tag{4.31}$$

$$F_1 = \tanh\left\{\left\{\min\left[\max\left(\frac{\sqrt{k}}{\beta^* \omega y'}, \frac{500v}{y^2\omega}\right), \frac{4\sigma_{\omega^2}}{CD_{k\omega}y^2}\right]\right\}^4\right\} \tag{4.32}$$

$$\phi = \phi_1 F_1 + \phi_2(1 - F_1) \tag{4.33}$$

$$CD_{k\omega} = \max\ 2\rho\sigma_{\omega^2}\frac{1}{\omega}\frac{\partial k}{\partial x_i}\frac{\partial \omega}{\partial x_j}, 10^{-10} \tag{4.34}$$

Constant Values;

$$\alpha_1 = \frac{5}{9}, \alpha_2 = 0{,}44, \beta_2 = 0{,}0828, \beta^* = \frac{9}{100} \tag{4.35}$$

$$\alpha_{k_1} = 0{,}85, \alpha_{k_2} = 1, \alpha_{\omega_1} = 0{,}5,, \alpha_{\omega_2} = 0{,}856 \tag{4.36}$$

Realizable k–ε Turbulence Model

In the k-ε model, to calculate the turbulent viscosity (μt), k is used as the kinetic energy of turbulence and ε is used in its dissipation rate. This model has been developed and is now known as the k-ε, Realizable model. It yields satisfactory results when used to fluxes in channels and boundary layers, jets and divided streams in high-speed flows [51].

By using the moment of the Navier-Stokes equation in equations (4.37) and (4.38), the precise equation of ε can be obtained.

$$2v\frac{\partial u_i'}{\partial x_j}\frac{\partial}{\partial x_j}[N(u_i)] \tag{4.37}$$

$$\rho\frac{\partial\varepsilon}{\partial t}+\rho U_j\frac{\partial\varepsilon}{\partial x_j}$$
$$=-2\mu\left[\overline{u'_{\iota,k}u'_{j,k}}+\overline{u'_{k,\iota}u'_{k,J}}\right]\frac{\partial U_i}{\partial x_j}-2\mu\overline{u'_k u'_{\iota,J}}\frac{\partial^2 U_i}{\partial x_k x_j}$$
$$-2\mu\overline{u'_{\iota,k}u'_{\iota,m}u'_{k,m}}-2\mu\nu\overline{u'_{\iota,km}u'_{\iota,km}}+\frac{\partial}{\partial x_j}\mu\frac{\partial\varepsilon}{\partial x_j} \quad (4.38)$$
$$-\mu\overline{u'_j u'_{\iota,m}u'_{\iota,m}}-2\nu\overline{p'_{\iota,m}u'_{j,m}}$$

5
MATERIAL AND METHOD

In aerodynamics, the main feature for a missile is the lift forces and drag forces or lift to drag ratio (C_L/C_D) of the geometry designs created by determining the body size, canard or wing position and its sizes and nose shape. The main feature of nozzles in aerodynamics is to design nozzles with appropriate geometry and serve the purpose of the missile.

In this section, missile geometry and nozzle geometry designs, analysis processes, aerodynamic analyzes and results are presented.

5.1 CFD Methodology

CFD software is one of the most practical and affordable ways to assess and explore the flow field; it has been in use since 1983 in numerous sectors all around the world [56].

ANSYS program can be used in various fields for instance, the machinery, chemical, automotive and aviation industries in effective solutions to mechanics, fluid mechanics and heat transfer problems. When faced with financial constraints, intricate model geometry design, measurement constraints or an inadequate test model geometry, CFD offers extremely substantial benefits. With the use of CFD, you can investigate flow characteristics in intricate model geometry designs without being constrained by measurement constraints and without affecting the flow. A solution called ANSYS Workbench integrates simulation technology with parametric CAD tools and enables the verification and development of the product in a virtual environment and helps to understand the suitability of a geometry at the preliminary stage without producing a prototype gives opportunity.

In this study, fluid flow was simulated using the CFD approach, which is predicated on the finite volume approach. In this thesis, ANSYS SpaceClaim Program was used in CAD designs, ANSYS Meshing Program was used to create the mesh structure, ANSYS Fluent Program was used to determine the missile's coefficients

of aerodynamics at various Mach values and angles of attack, and CFD calculations were used to determine the Mach number for the nozzle.

5.1.1 Mesh Generation

The mesh structure is the structure used to discretely solve the flow field defined as an assortment of several distinct points or geometry in aerodynamic engineering problems. To obtain accurate results, the number of mesh elements and the boundary layer of the geometry are important. For this reason, the density of mesh formation may vary regionally and mesh structures may also vary according to geometry. There are two methods for creating meshes: structured and unstructured.

The structured mesh converts the curvilinear mesh into a smooth Cartesian mesh by implementing it as hexagonal components in the 3D model and quadrilateral elements in the 2D model. The unstructured mesh can be implemented as triangular elements for 2D geometries and tetrahedral elements for 3D geometries with complex geometries. This type of mesh provides advantages in terms of mesh adaptability and flexibility, and in comparison, to structured meshing, the meshing process is quicker. However, while unstructured meshes provide advantages in terms of meshing adaptation, they also have disadvantages as they require more computation time.

To reduce calculation time, coarser meshes can be created in unnecessary parts of the flow field. The number of mesh elements can be increased to obtain accurate results by minimizing the numerical error. In this study, mesh was created using the ANSYS Meshing program.

5.2 Supersonic Missile Geometry Design, Mesh Generation and Performing CFD Analysis

5.2.1 Supersonic Missile Design

The missile geometry examined was chosen as the AIM 120 AMRAAM Missile model with body-wing-tail configuration. In the missile geometry, the length was shortened and the wing and tail section depending on the length were reduced, the diameter was used as it and the solid model was created in ANSYS SpaceClaim in order to be used in unmanned aerial vehicles. The fundamental goal is investigation the variation in length-diameter change of the currently approved AIM 120 AMRAAM Missile model [27].

The AIM 120 AMRAAM Missile model is shown in Figure 5.1 and its dimensions are given in Table 5.1.

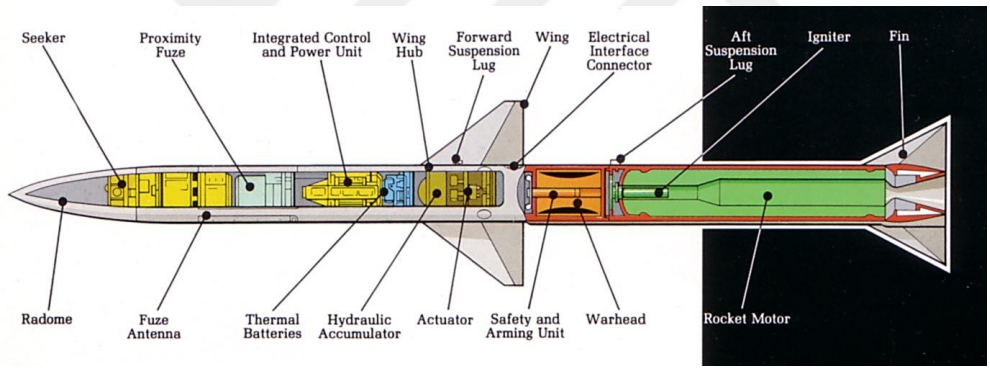


Figure 5.1 The AIM 120 AMRAAM Missile model [57]

Table 5.1 The AIM 120 AMRAAM Missile diamentions [58]

Length of Missile(m)	3,66
Diameter of Missile(m)	0,18
Fin span(m)	0,53
Launch Weight of Missile(kg)	150,75

The solid model of the missile designed in SpaceClaim is shown in Figure 5.2, and its dimensions are given in Table 5.2.

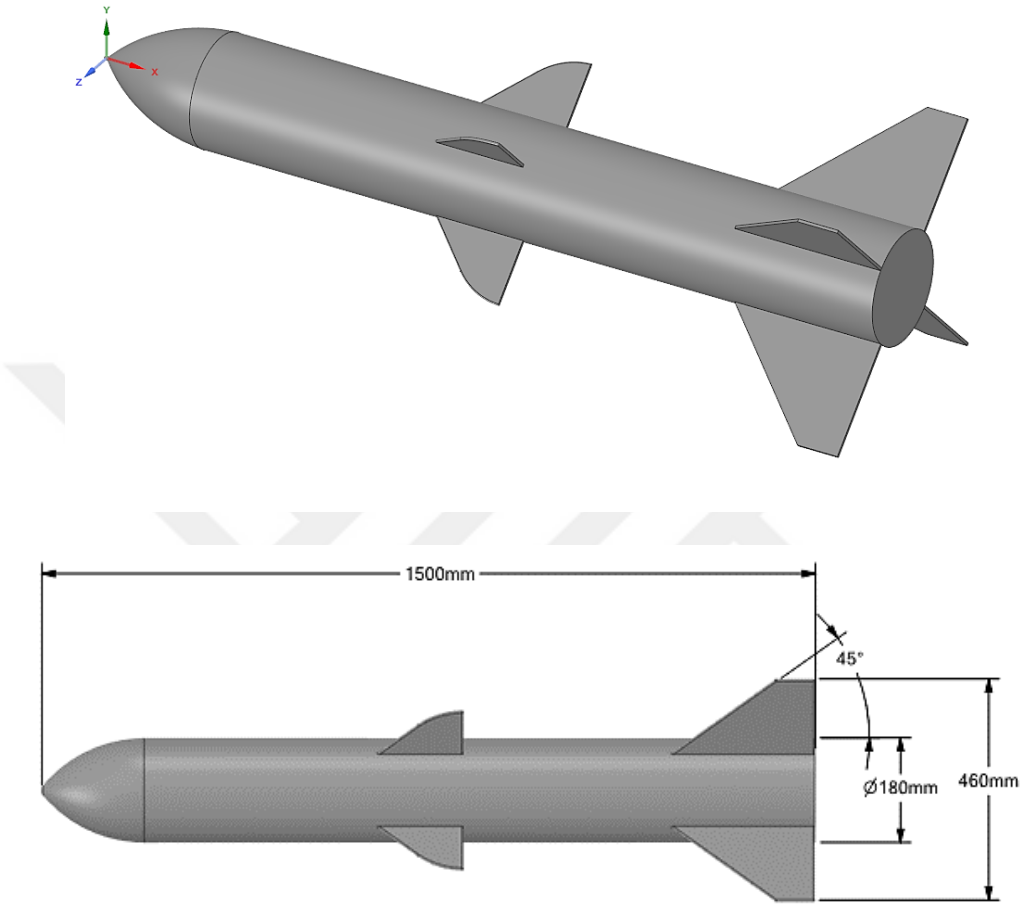


Figure 5.2 AIM 120 AMRAAM missile variation solid model

The computational field is modeled as a rectangular far-field pressure located roughly 20 fuselage lengths downstream from the model in Figure 5.3 and 10 fuselage lengths upstream and sidestream from the tip of the missile nose.

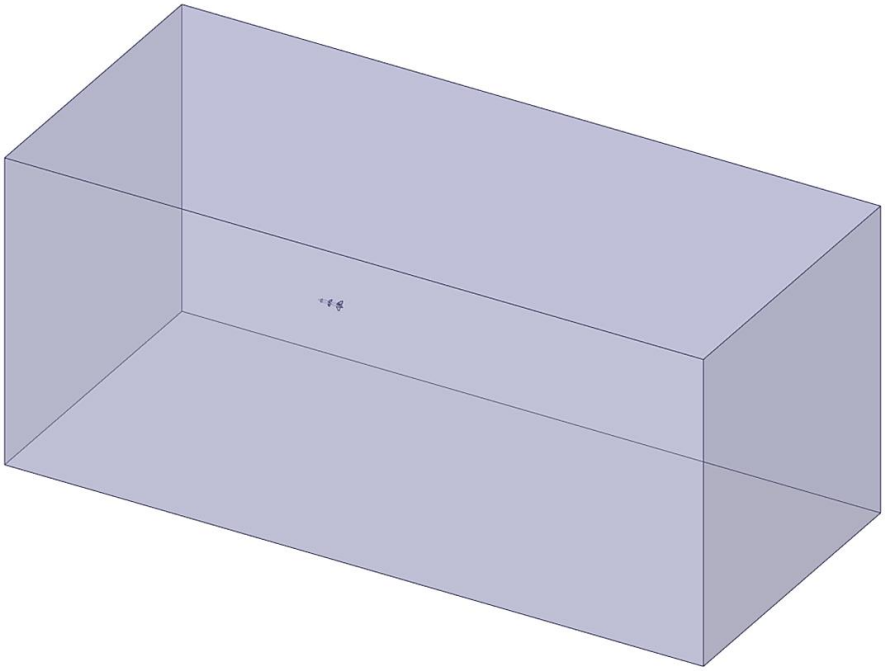


Figure 5.3 Three-Dimensional view of the fluid environment

Table 5.2 AIM 120 AMRAAM Missile variation solid model dimensions

Length of Missile(m)	1,5
Diameter of Missile(m)	0,18
Length of Wing(m)	0,08
Length of Tail(m)	0,14

5.2.2 Supersonic Missile Stability Ratio by OpenRocket Tool

The dimensions of the supersonic missile geometry were designed considering aerodynamic stability according to the C_P-C_G ratio. In the OpenRocket tool, the ratio was found to be stable when the missile was designed according to the measurements in Table 5.3.

Table 5.3 Sembology of C_P and C_G at OpenRocket

	:	C_P
	:	C_G

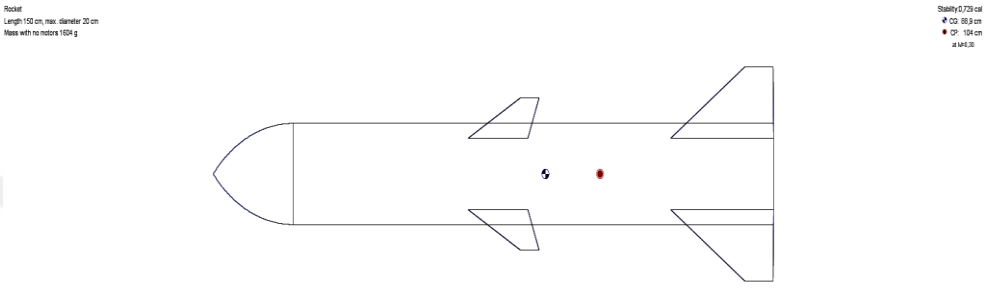


Figure 5.4 Supersonic rocket on axis of flight using OpenRocket tool

The fact that the stability ratio of the missile designed in the OpenRocket program results in a negative value means that the rocket is not stable and needs to be redesigned. When it is used the OpenRocket tool, it is obtained accurate measurement results as the C_G was 88,9 cm, the C_P was 104 cm, and the stability was 0,729 cal which shown in Figure 5.4.

5.2.3 Supersonic Missile Meshing

The three-dimensional calculation area of the designed missile was created using ANSYS SpaceClaim and its mesh was created using ANSYS Meshing programs. The computational model is calculated similarly to supersonic missile data.

In order for the analyzes to be resolved quickly, a mesh structure was created for the axi-symmetric of the geometry and far-field pressure and the analyzes were calculated accordingly. Figure 5.5 depicts mesh generation in the fluid environment, while Figure 5.6 depicts mesh generation on a missile.

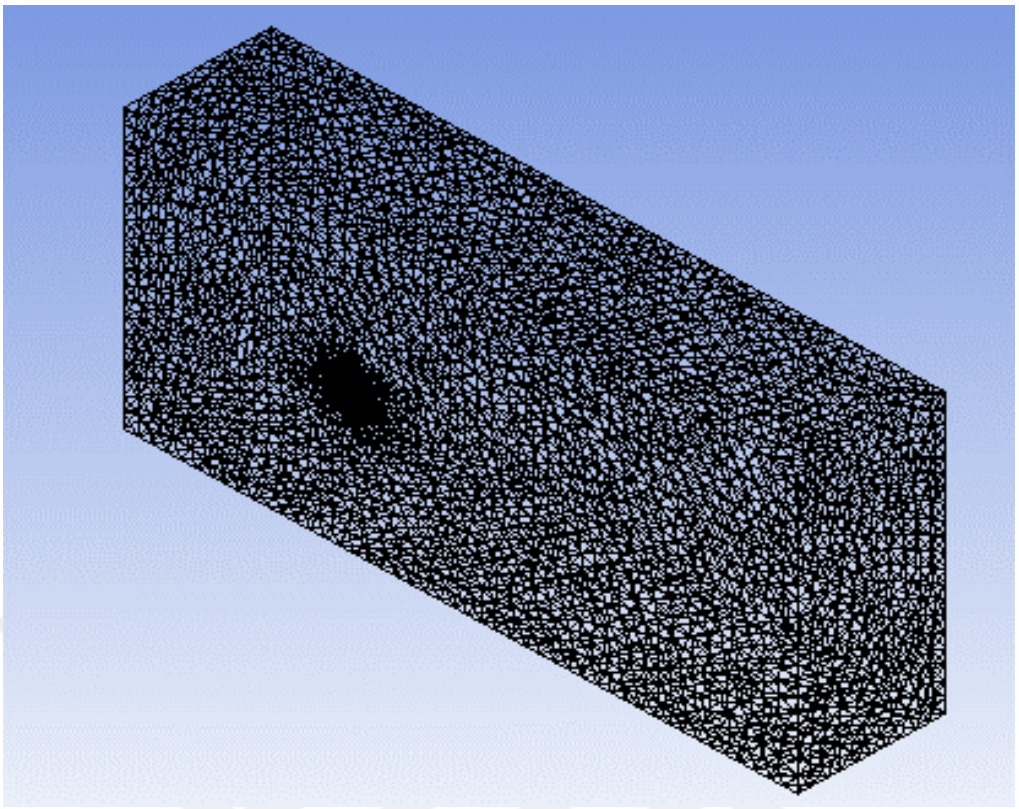


Figure 5.5 Mesh creation in a fluid environment

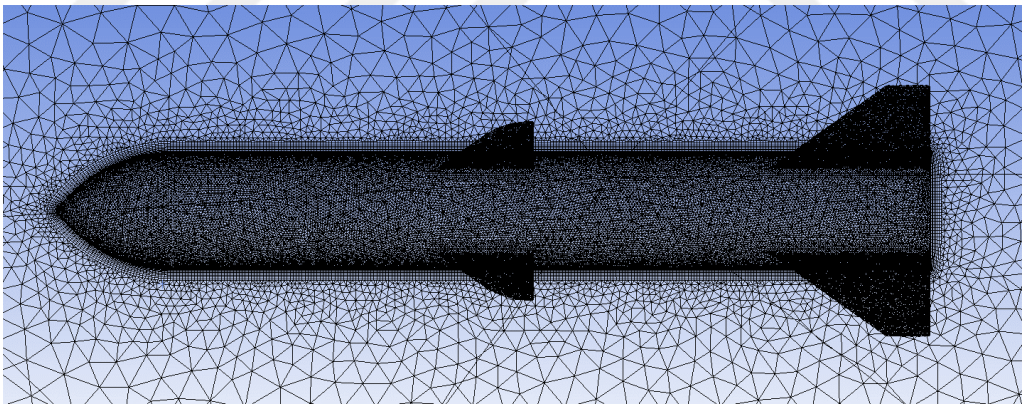


Figure 5.6 Mesh creation on missile

If the skewness criterion, which indicates the suitability of the solution mesh, is above 0,9; there is a possibility that the solution results will be incorrect [48]. The maximum value of this value for the analysis study is approximately 0,86. The Aspect Ratio value, which is the growth rate between the solution mesh elements to be used in the finite element analysis, must be below 200 [48]. The maximum value of this value is approximately 101. These values can be seen graphically in

the "Mesh Metrics" section of ANSYS Fluent. The visuals related to these values are as in Figure 5.7.

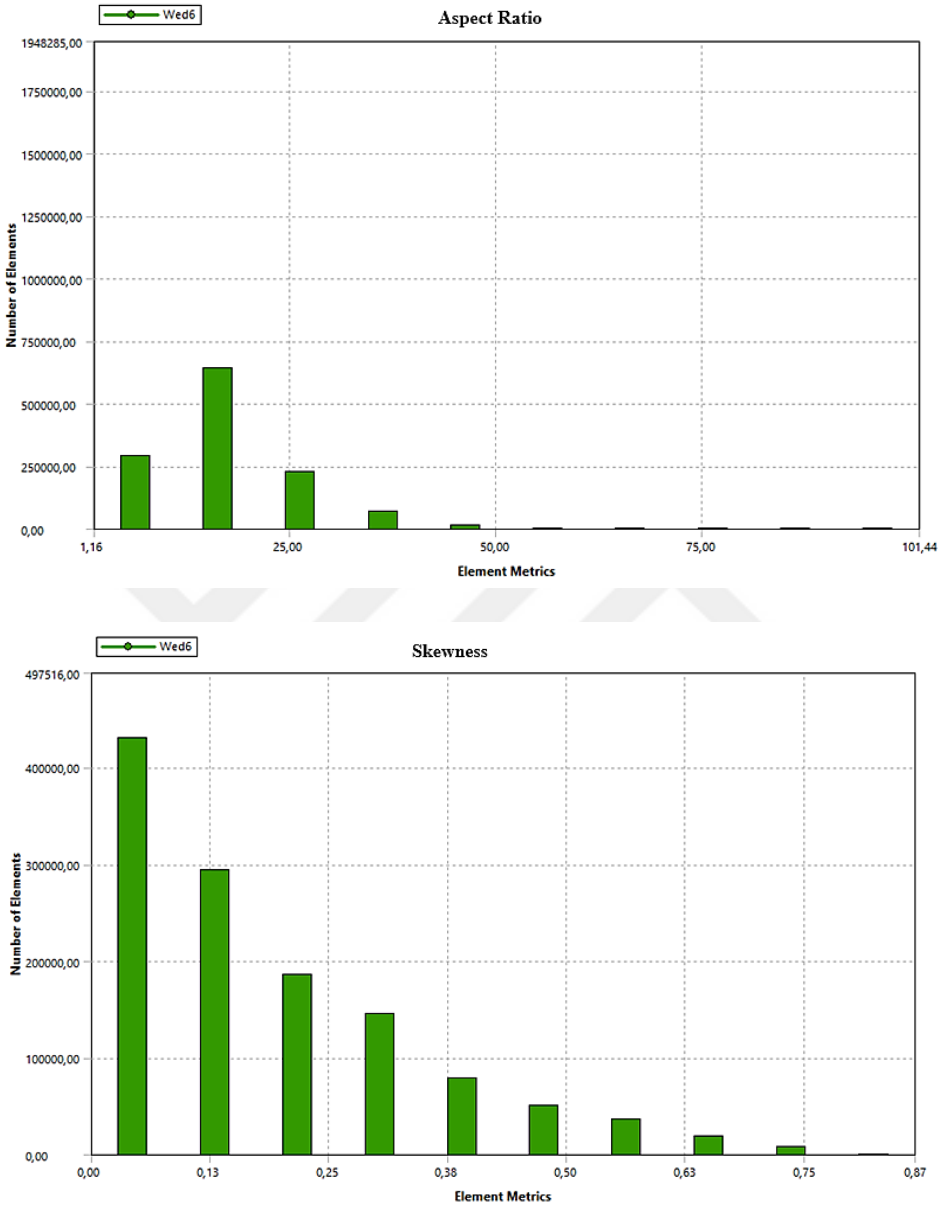


Figure 5.7 Distributions of Aspect Ratio and Skewness values belonging to the solution mesh of missile

5.2.4 Performing CFD Analysis for Supersonic Missile Using ANSYS Fluent

After the solution mesh creation process was completed, the created solution mesh file was transferred to the program using ANSYS Fluent 2020 R2 version. During the analysis phase, unit systems were first converted to the British SI unit system in order to be fully compatible with the experimental conditions. Since the air to circulate in the system will circulate at high speeds (Mach Number> 1), a density-based solver was chosen. Material properties are defined by choosing ideal gas density and Sutherland viscosity as shown in Figure 5.8 depending on high speeds.

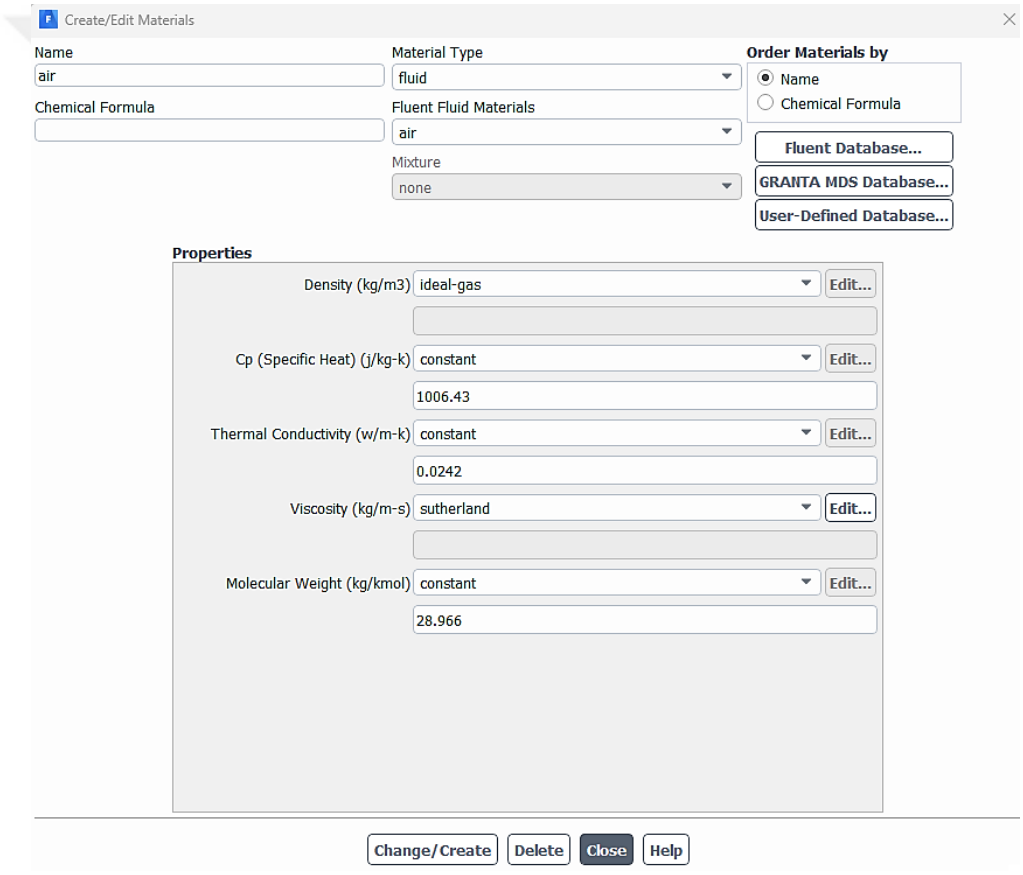


Figure 5.8 Material properties definition screen for missile in Ansys Fluent

The "pressure far field" boundary condition, which will provide free flow to the front quarter circle part and upper parts of the flow field that encounters air, has been defined. For the back portions where the air will separate from the flow area, the boundary condition known as the "pressure outlet" is defined. The flow field's side surfaces define the symmetry boundary condition. The axi-symmetric condition is defined because an axi-symmetric solution will be generated for the edges at the bottom of the flow field.

For CFD solutions, first things must be calculated the dimensionless Reynolds number of the flow and determine whether the flow will be modeled as turbulent or laminar. For the problem solved here, the Reynolds number was calculated as $1.2x10^6$ at its minimum value and all solutions were made in a turbulent regime. In this thesis, Spalart-Allmaras (Figure 5.9), k- ω, SST (Figure 5.10) and k-ε, Realizable (Figure 5.11) models were used to compare Reynolds-Based Navier-Stokes (RANS) turbulence analysis methods.

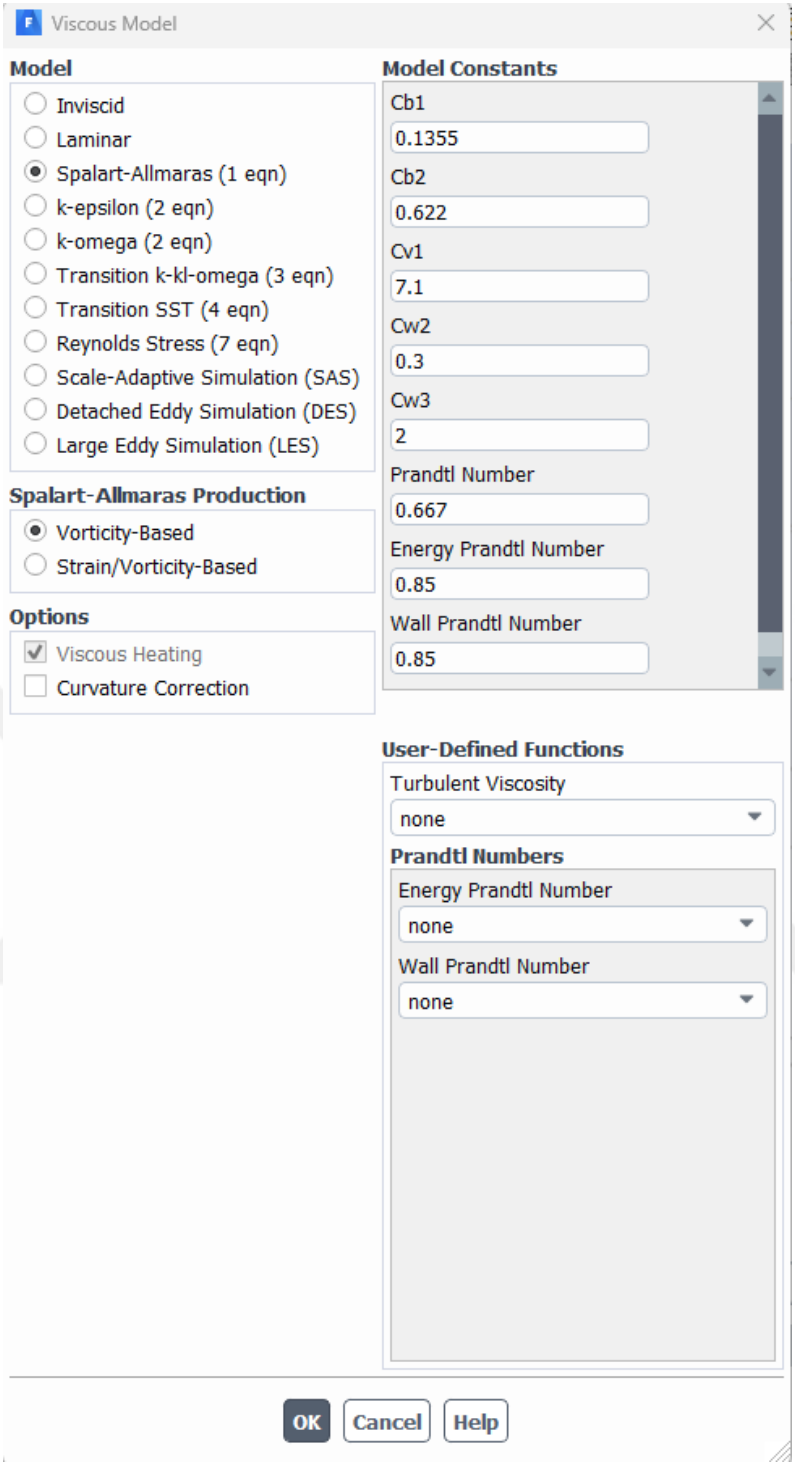


Figure 5.9 Spalart-Allmaras turbulence model settings view for missile in Ansys Fluent

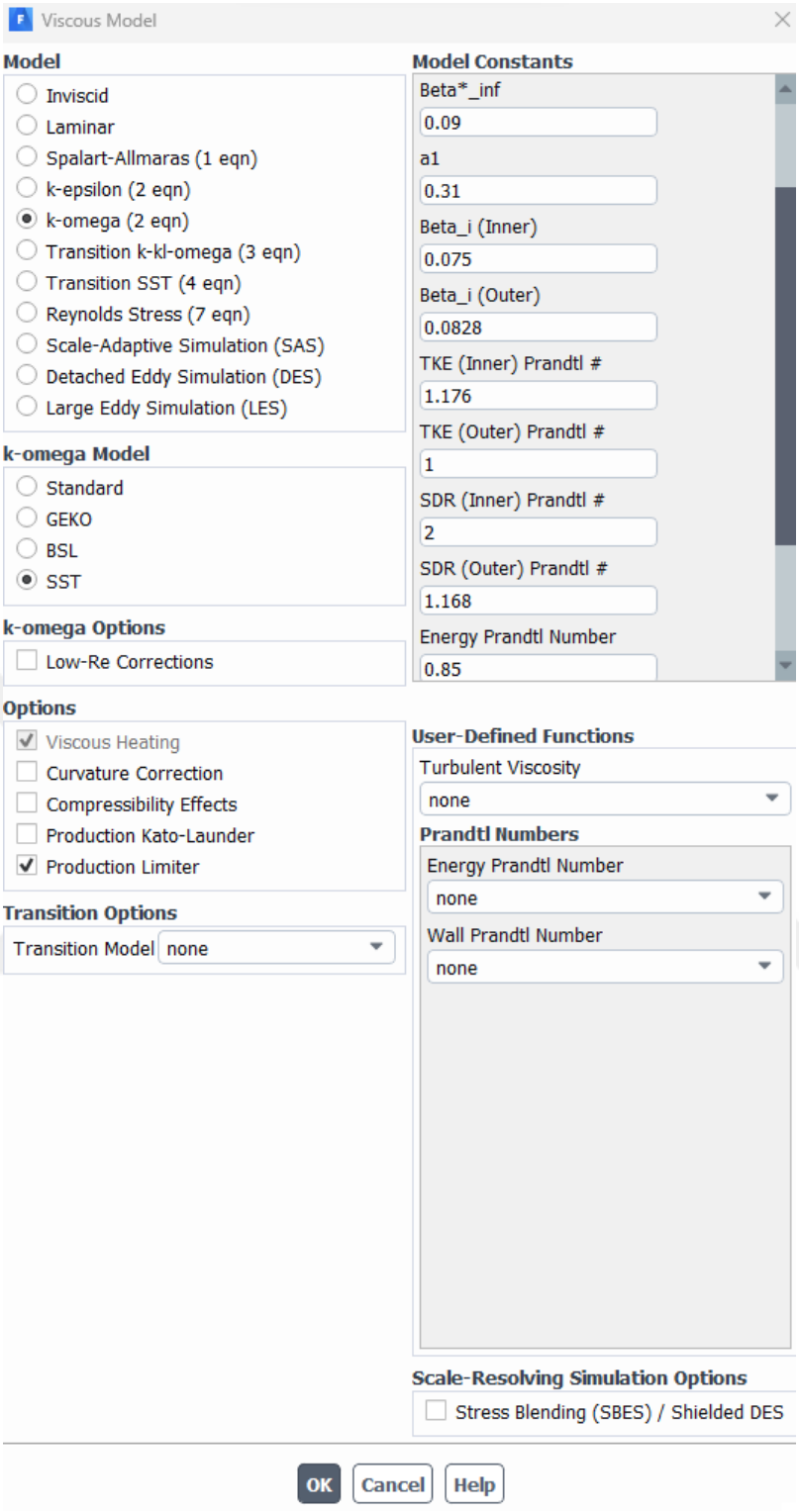


Figure 5.10 k-ω, SST turbulence model settings view for missile in Ansys Fluent

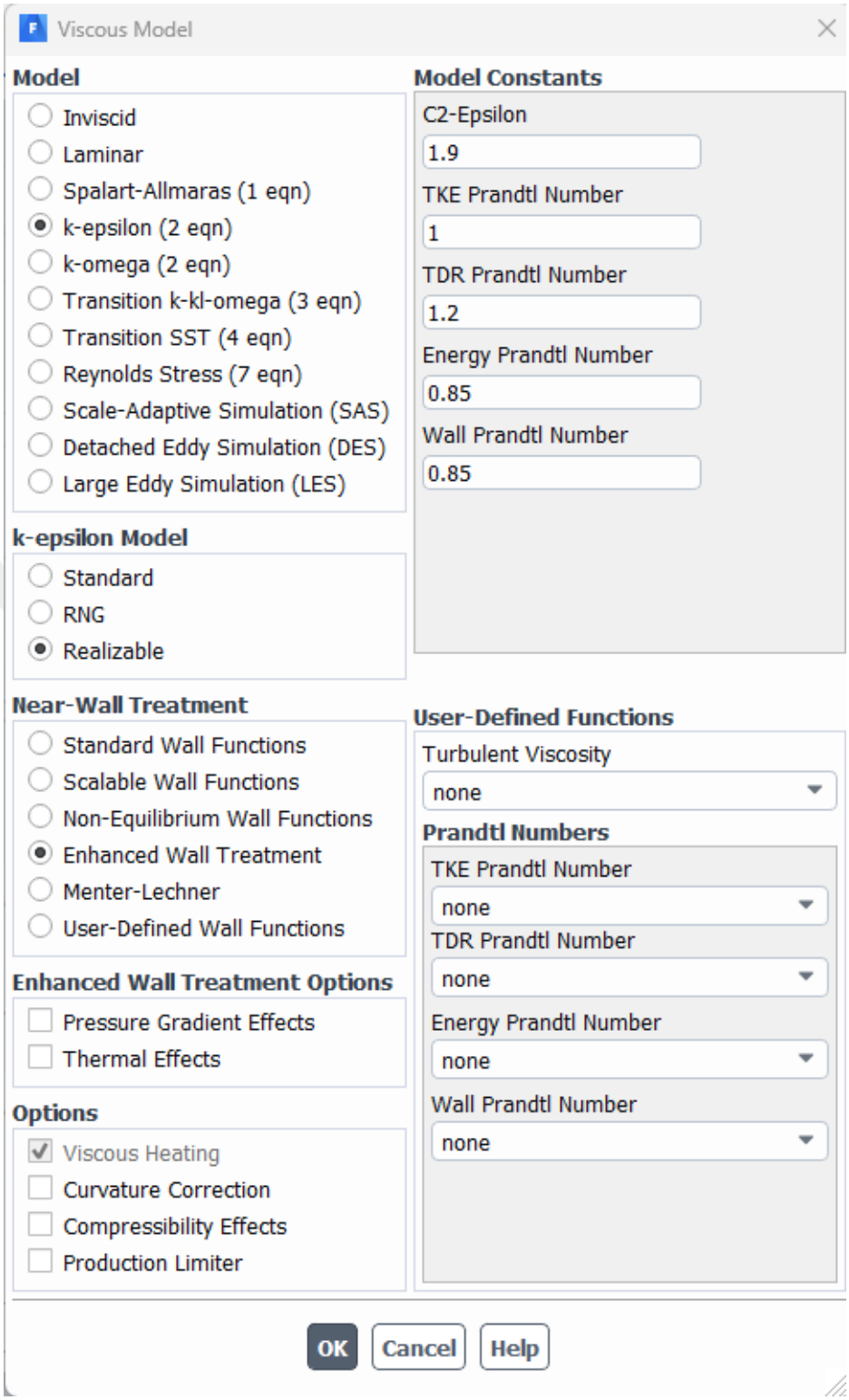


Figure 5.11 k-ε, Realizable turbulence model settings view for missile in Ansys Fluent

There are different methods and solution algorithms that can be used to solve conservation equations in CFD solutions. In density-based solutions, the implicit method was chosen to resolve the conservation equations. The Implicit solution method performs the solution by using the time step and solution mesh size together, based on the dimensionless CFL number, and provides high accuracy for compressible flows. The solution levels of the equations to be solved for the k-ε, Realizable (Figure 5.13) and k-ω, SST models (Figure 5.12) used for turbulence modeling were determined as Second Order Upwind, which provides increased precision for the equations related to flow, temperature and turbulence, but requires longer periods of time for convergence. The Spalart-Allmaras model (Figure 5.14) used in single-equation turbulence modeling is solved as First Order Upwind.

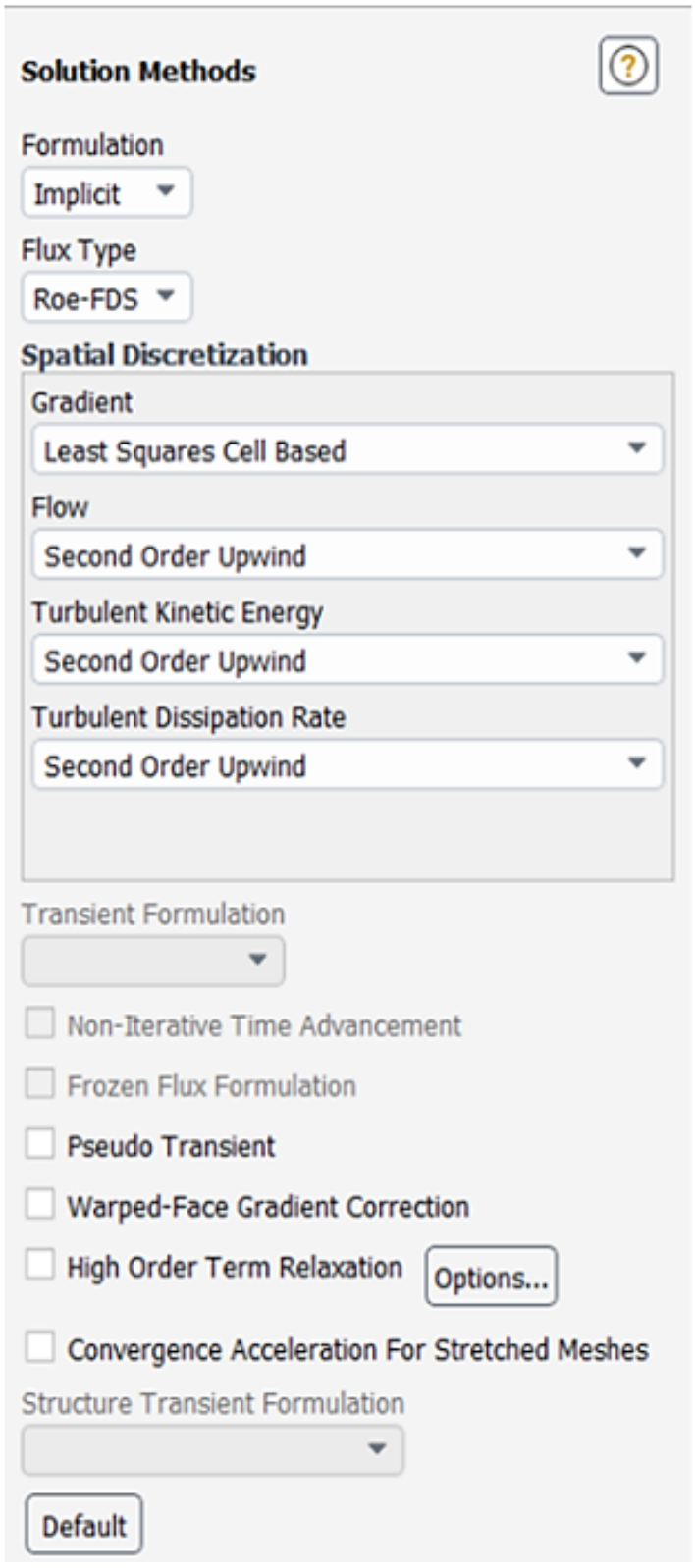


Figure 5.12 k-ω, SST solver settings for missile in Ansys Fluent

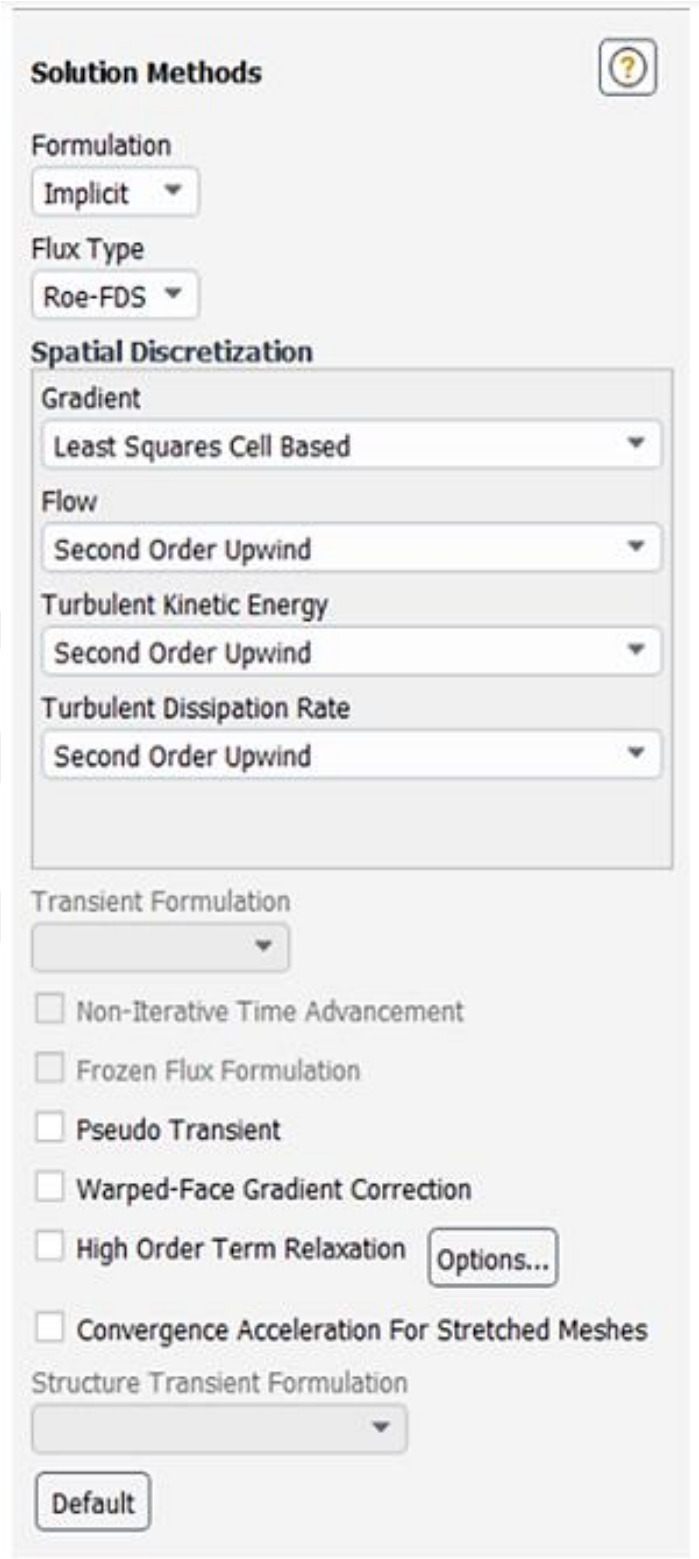


Figure 5.13 k-ε, Realizable solver settings for missile in Ansys Fluent

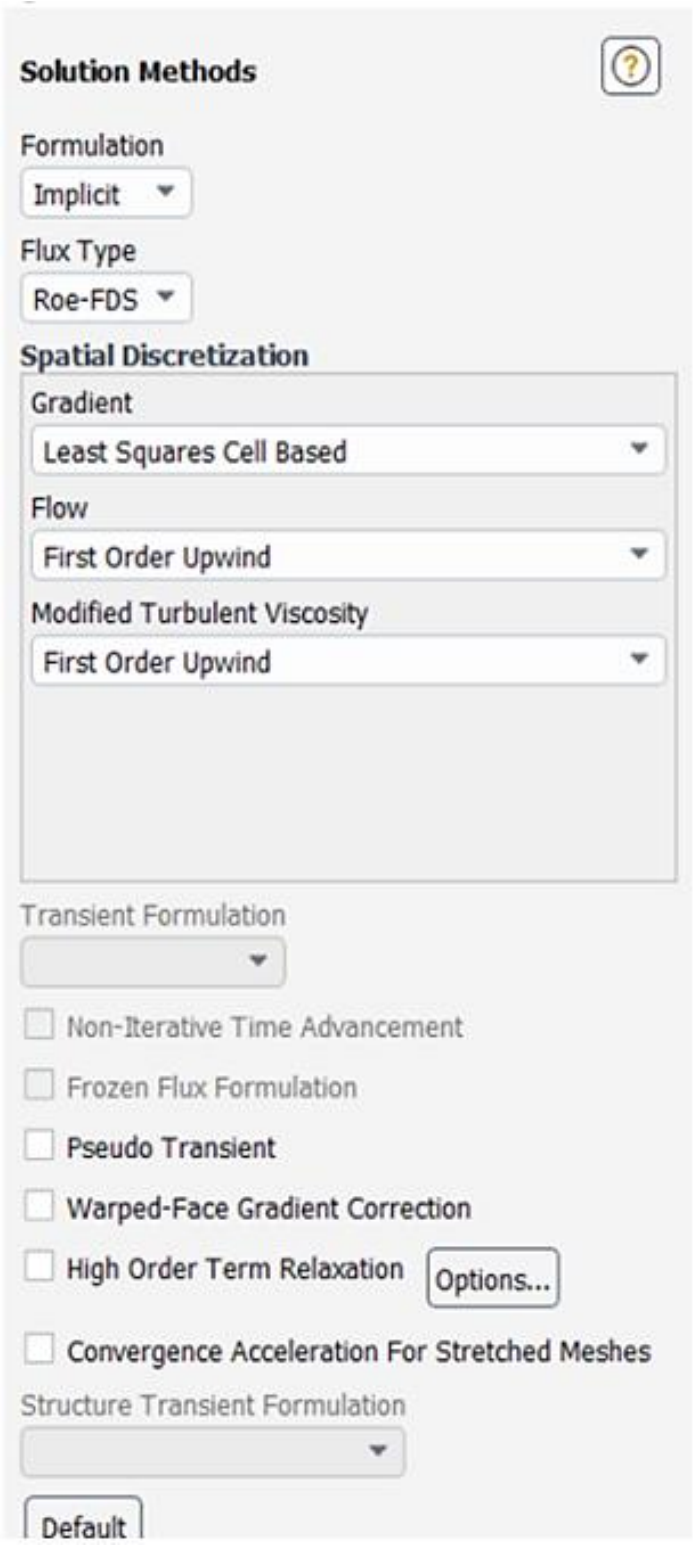


Figure 5.14 Spalart-Allmaras solver settings for missile in Ansys Fluent

5.3 Supersonic Nozzle Geometry Design, Mesh Generation and Performing CFD Analysis

5.3.1 Supersonic Nozzle Design

The cone model of the nozzle geometry examined for use in the supersonic missile designed in this thesis was chosen as the nozzle type.

Cone nozzles with 30 mm, 40 mm and 50 mm throat widths were designed to capture supersonic output in ANSYS Fluent.

The supersonic nozzle drawing was modeled as axi-symmetric in ANSYS SpaceClaim Design Modeler program, the relevant model is shown in Figure 5.15.

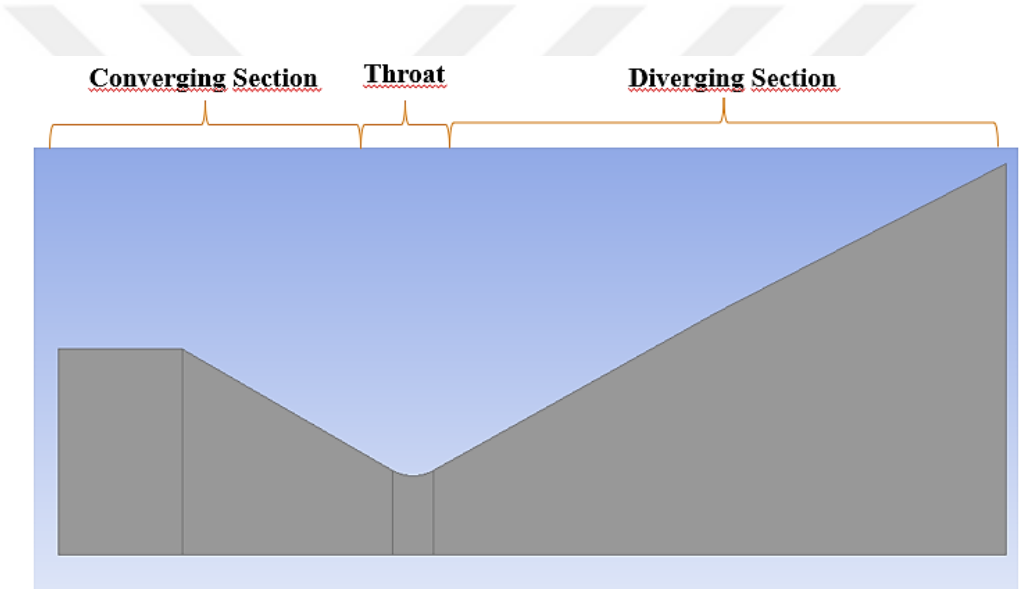


Figure 5.15 Axi-symmetric nozzle design

As shown in Figure 5.16, three nozzles with different throat widths were designed as nozzle sizes. In each nozzle, there are some values are designed as constant values that the inlet length is 100 mm, the outlet length is 180 mm and the half angle is 15 degrees. Throat widths are designed as 30 mm, 40 mm and 50 mm as variable values.

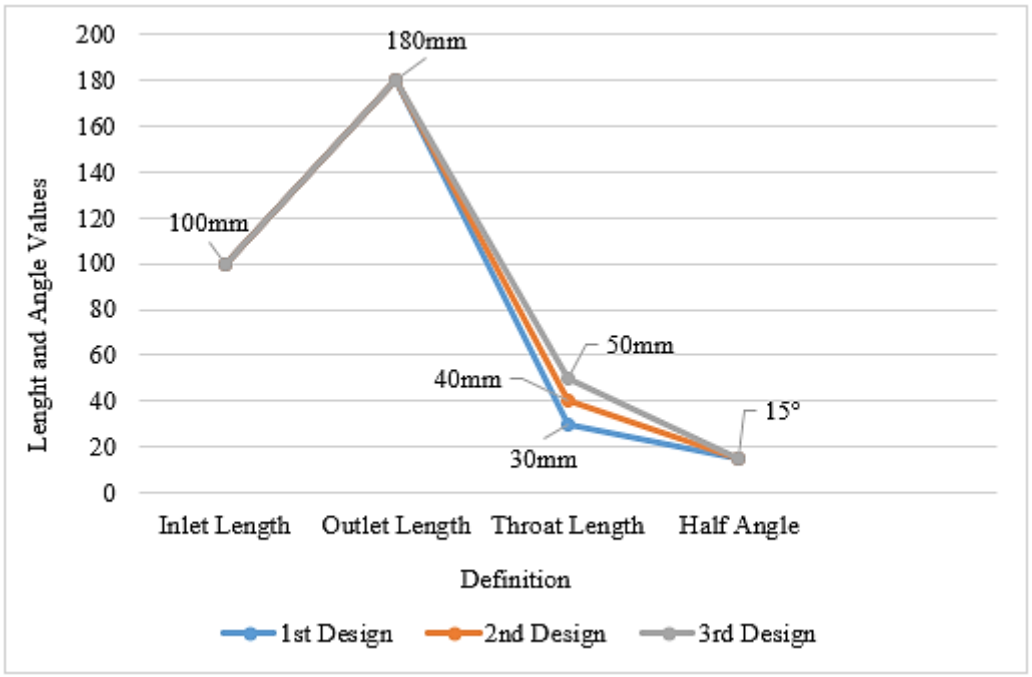


Figure 5.16 Nozzle dimensions

5.3.2 Supersonic Nozzle Meshing

The two-dimensional calculation area of the designed missile was created using ANSYS SpaceClaim and its mesh was created using ANSYS Meshing programs. The computational model is calculated similarly to supersonic nozzle data.

In order for the analyzes to be resolved quickly, a mesh structure was created for the symmetry of the geometry the analyzes were calculated accordingly as shown in Figure 5.17.

The number of mesh elements for the axi-symmetry nozzle was produced 34.293 for the nozzle with 30 mm throat width, 39.026 for the nozzle with 40 mm throat width and 45.092 for the nozzle with 50 mm throat width.

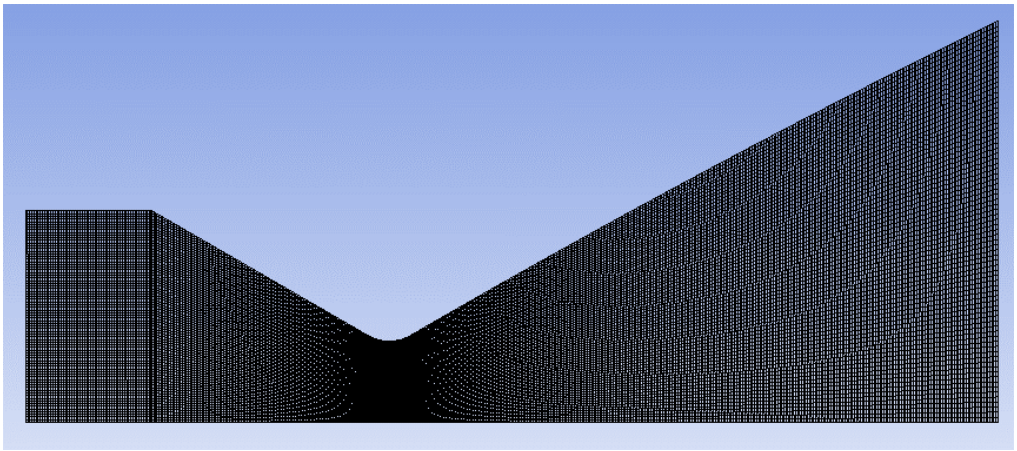


Figure 5.17 Mesh generation on nozzle

If the skewness criterion, which indicates the suitability of the solution mesh, is above 0,9; there is a possibility that the solution results will be incorrect [48]. The maximum value of this value for the analysis study is approximately 0,33. The Aspect Ratio value, which is the growth rate between the solution mesh elements to be used in the finite element analysis, must be below 200 [48]. The maximum value of this value is approximately 2,5. These values can be seen graphically in the "Mesh Metrics" section of ANSYS Fluent. The visuals related to these values are as in Figure 5.18.

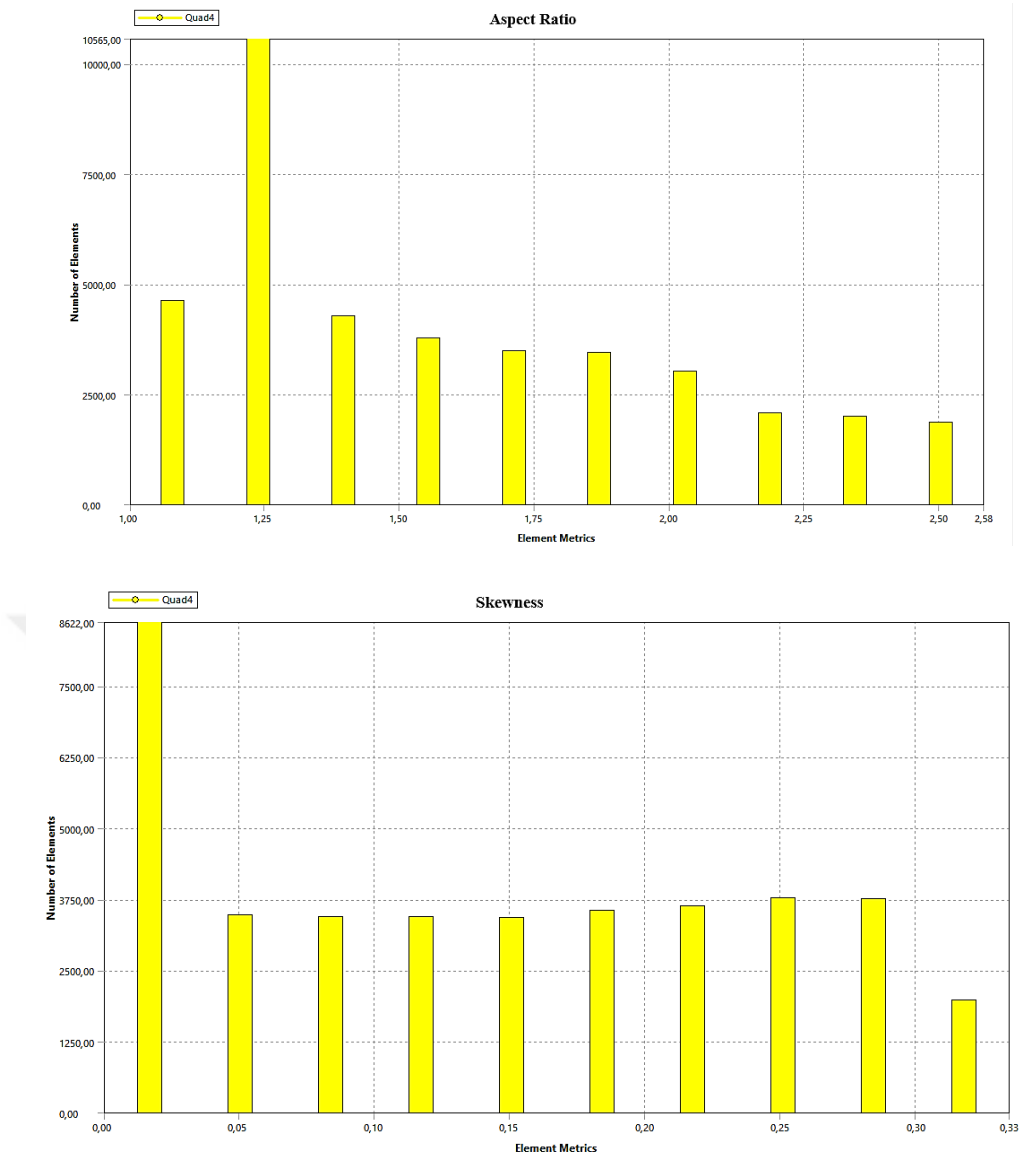


Figure 5.18 Distributions of Aspect Ratio and Skewness values belonging to the solution mesh of nozzle

5.3.3 Performing CFD Analysis for Nozzle Using ANSYS Fluent

After completing the solution mesh creation process, similar to the steps performed in the supersonic missile, the created solution mesh file was transferred to the program using ANSYS Fluent 2020 R2 version and the unit systems were converted to the British SI unit system during the analysis phase. Since it will be a 2D analysis, a density-based solver in the axisymmetric area was chosen. Material properties are defined by choosing the ideal gas density and Sutherland viscosity based on high speeds as shown in Figure 5.19.

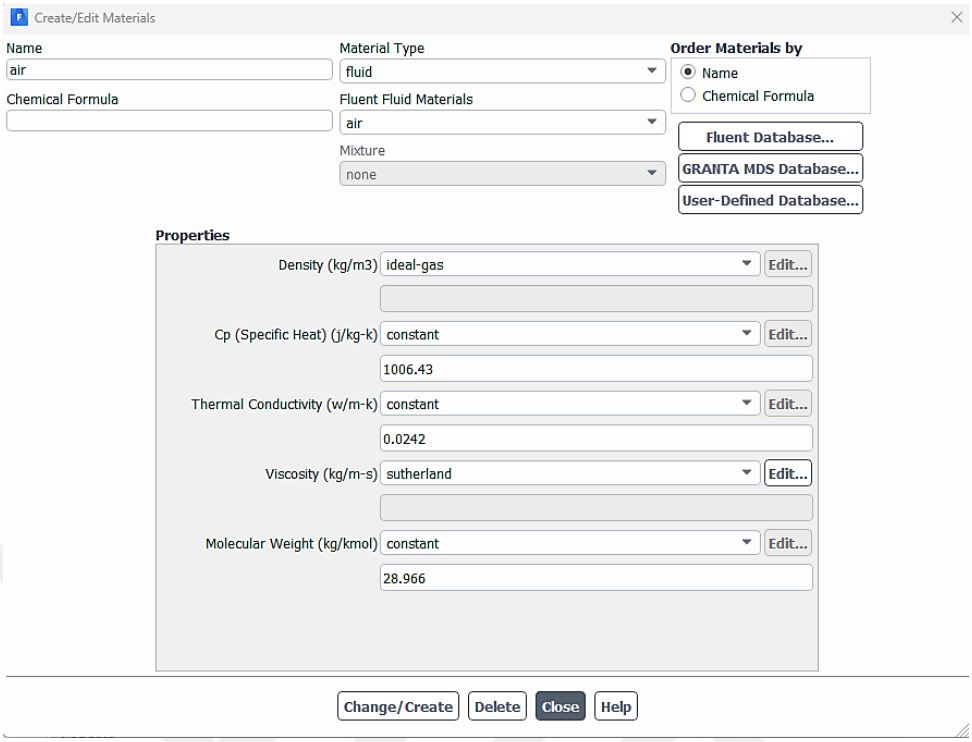


Figure 5.19 Material properties definition screen fot nozzles in Ansys Fluent

There are different methods and solution algorithms that can be used to solve conservation equations in CFD solutions. In density-based solutions, the implicit method was chosen to solve the conservation equations. The Implicit solution method performs the solution by using the time step and solution mesh size together, based on the dimensionless CFL number, and provides high accuracy for compressible flows. The equations that need to be solved at the solution levels for the k-ω, SST, and k-ε, Realizable models that are used to model turbulence were chosen as Second Order Upwind as shown in Figure 5.20, which provides higher accuracy for the equations related to flow, temperature and turbulence, but requires longer periods of time for convergence.

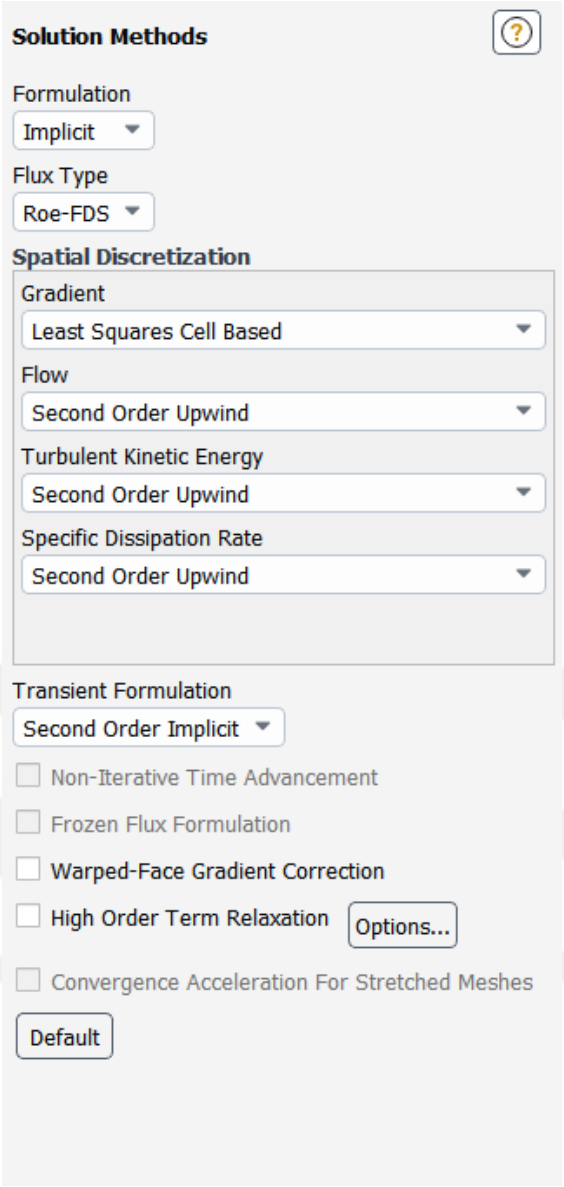


Figure 5.20 Solver settings for nozzles in Ansys Fluent

Calculating the flow's dimensionless Reynolds number and deciding whether to represent the flow as turbulent or laminar are prerequisites for using CFD solutions. For the problem solved here, the Reynolds number was calculated as $1.2x10^6$ at its minimum value and all solutions were made in a turbulent regime. In this thesis, k-ω, SST (Figure 5.21) and k-ε, Realizable (Figure 5.22) models were used to compare Reynolds-Based Navier-Stokes (RANS) turbulence analysis methods.

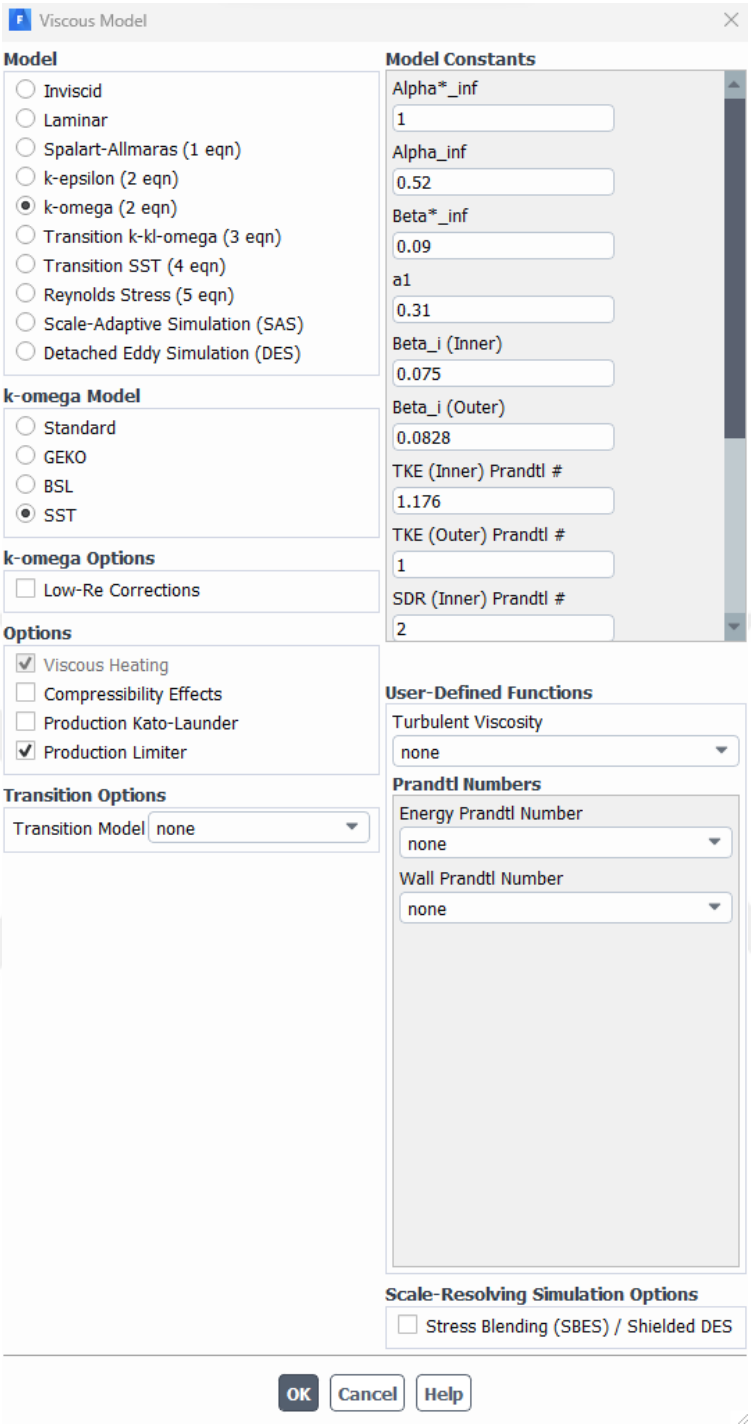


Figure 5.21 k-ω, SST turbulence model settings view for nozzles in Ansys Fluent

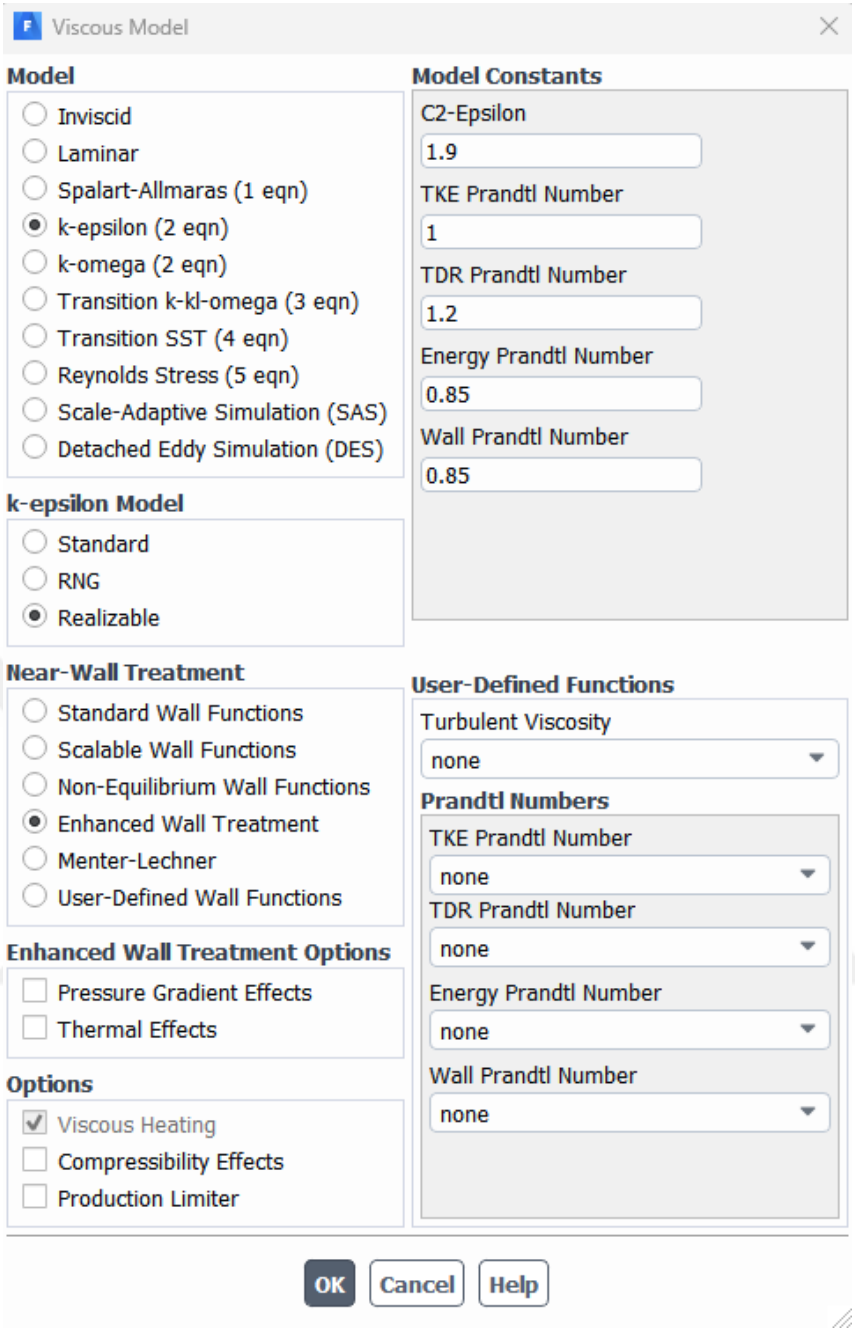


Figure 5.22 k-ε, Realizable turbulence model settings view for nozzles in Ansys Fluent

6
RESULTS AND DISCUSSION

6.1 Supersonic Missile Analysis Results

CFD analyzes are carried out by correctly preparing a series of parameters as mentioned in the previous sections. Within the scope of this study, analyzes were executed using the Ansys Fluent solver program. Analyzes were solved on a workstation with 14 core processor power. Analysis, solution mesh creation and solution processes took approximately 4 hours with Ansys Fluent. After the CFD analyzes are completed correctly, the evaluation and visualization of the results (post processing) is completed. Mach number distribution contours, pressure contours, temperature contours, drag, lift and moment force coefficients and the ratios of these coefficients (C_L/C_D and C_M/C_D) were obtained. The formulas used to calculate drag, lift and moment force coefficients are given in equations (6.1), (6.2) and (6.3).

$$C_M = \frac{M}{qS_C} \tag{6.1}$$

where c is the length of the chord of the wings and tails, S is the wing area, q is the dynamic pressure, and M is the pitching moment.

$$C_D = \frac{D}{\rho V^2 A/2} \tag{6.2}$$

$$C_L = \frac{L}{\rho V^2 A/2} \tag{6.3}$$

Where D is the drag force, ρ is the density, V is the Fluid speed, A is the front view area, L is the lift force.

6.1.1 Determining Number of Mesh Elements

6.1.1.1 Near Wall Treatment

The Mesh environment in ANSYS was used to create the unstructured hybrid mesh. Due to the fact that CFD evaluations were carried out at supersonic flow, the disposition of a missile's mesh is dependent on capturing the shock wave. In order to resolve the missile's boundary layer and capture a viscous sublayer to the wall function that reduced numerical efforts, ten layers of prismatic cells were created around it. A calculating machine was used to calculate the first layer height [59]. The data used in the determining of the boundary layer which is near wall treatment are included in the Table 6.1. Carecteristic lenght is a missile diameter which is 0,18 m. The free stream velocity was calculated as 514.5 m/s for 1.5 Mach number, 686 m/s for 2 Mach number and 857.5 m/s for 2.5 Mach number applied in the pressure-far-field. Density and dynamic viscosity are constant values for air. As a result of the data obtained, the first cell height was calculated as 0,0000016409.

Table 6.1 Near wall treatment [59]

INPUT VALUES	Characteristic Length for External Flow (Ø)	0,18 m
	Velocity of Free Stream U [m/s]	514.5
	Density ρ [kg/m^3]	1,204
	Dynamic Viscosity μ [kg.(m/s) = N.(s/m^2) = Pa.s]	0,00001813
	Desired y+ [dimensionless]	∼1
OUTPUT VALUES	Kinematic Viscosity ν [m^4/s]	0,000015
	Reynolds Number Re_x [dimensionless]	6.150.162,162
	First Cell Height [m]	0,0000016409

The first layer heights created in the mesh structure for the missile are shown in the Figure 6.1.

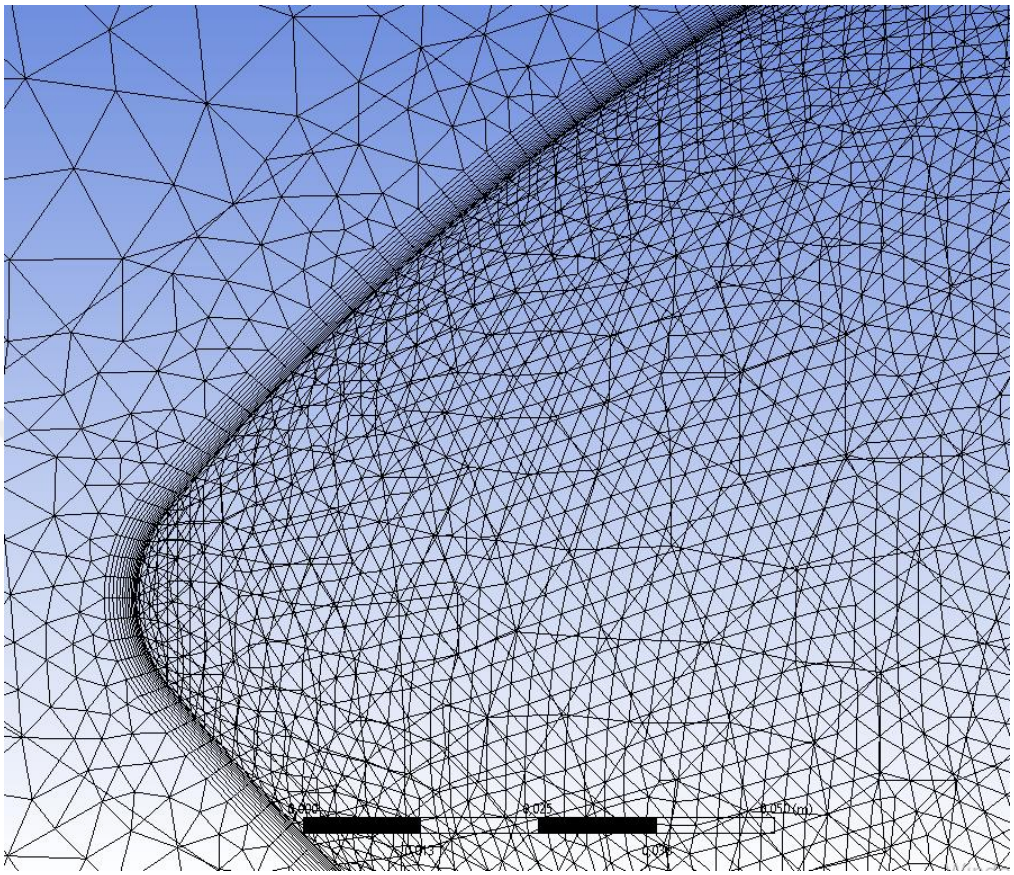


Figure 6.1 The first layer heights of the missile

6.1.1.2 Grid independence

In order to exhibit mesh independence, between one million and four million mesh components were generated for axi-symmetric misile. The friction coefficients on the geometry at 0° angle of attack were examined in ANSYS Fluent and the data are shown in the Table 6.2. As a result, the mesh element, which is the last value at which the friction coefficient at 0,01475 does not change, was determined as 2,717,498 in the 5th attempt.

Table 6.2 Grid independence

#Attempts	Number of Elements	Number of Nodes	C_D Coefficient
#1	1.572.006	473.751	0,01467
#2	1.847.265	565.858	0,01471
#3	1.979.990	549.980	0,01473
#4	2.311.444	705527	0,01474
#5	2.717.498	781.382	0,01475
#6	3.884.866	1.204.144	0,01475

6.1.2 CFD Results

These three turbulence models which are k-ω, SST, Spalart-Allmaras and k-ε, Realizable at AoA of 0°, 6°, 12°, 18° for Mach number 1.5, 2, 2.5, had their CFD results solved.

In the solution with used Spalart-Allmaras turbulence model at 0°, 6°, 12°, 18° AoA for Mach number 1.5, 2, 2.5, the residuals values are generated as x-y-z velocity, continuity, energy and nut which stands for Spalart-Allmaras turbulence model. The residuals values are shown in the Figure 6.2 for Mach number 1.5, in the Figure 6.3 for Mach number 2 and in the Figure 6.4 for Mach number 2.5.

Since the residual values remained constant at a certain sine wave for all data and were below 10^{-3}, they were deemed sufficient for the solution.

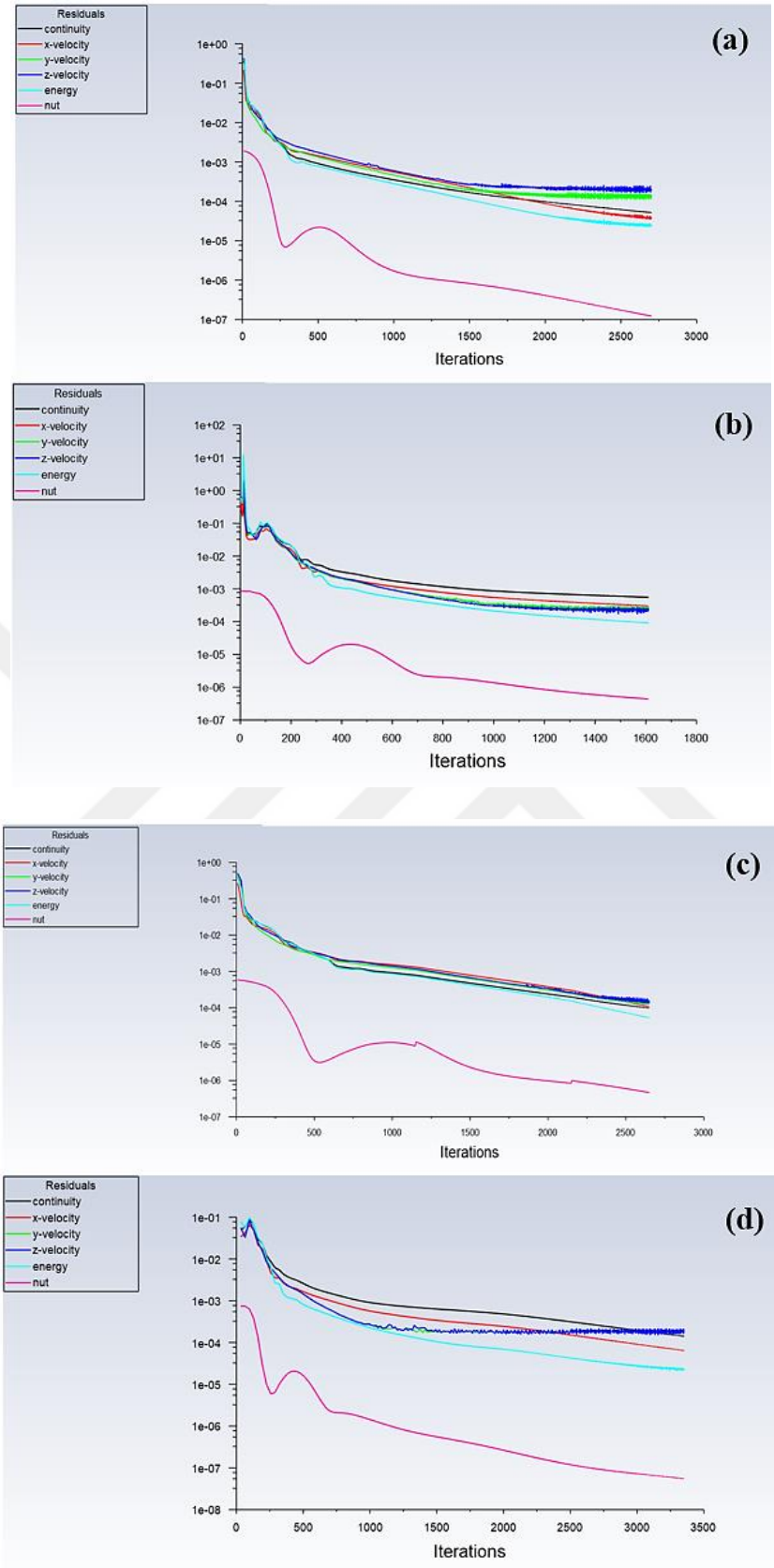


Figure 6.2 Residual values of angles of attack at Mach 1.5 in the Spalart-Allmaras turbulence model (AoA values; a: 0°, b: 6°, c: 12°, d: 18°)

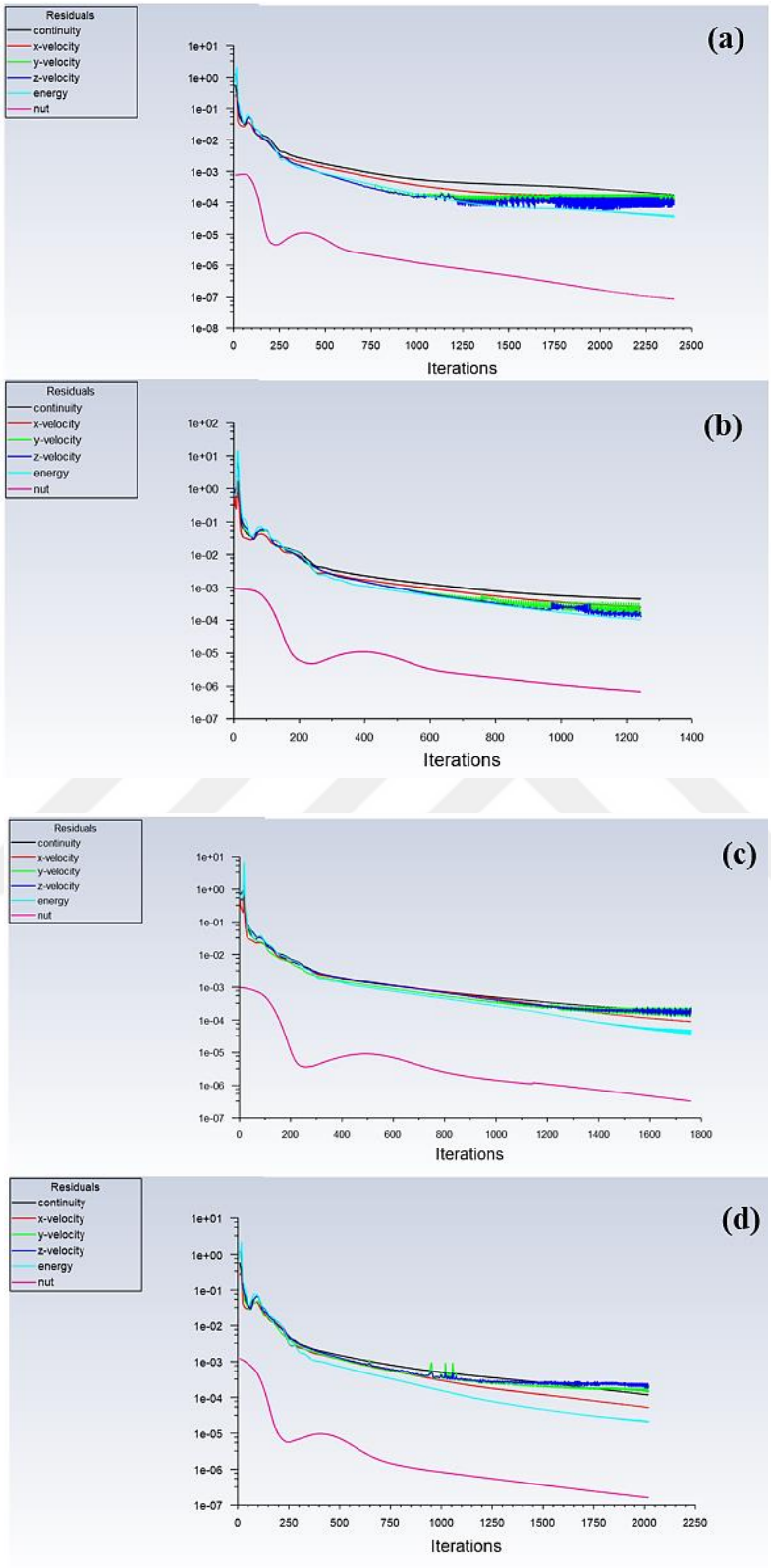


Figure 6.3 Residual values of angles of attack at Mach 2 in the Spalart-Allmaras turbulence model (AoA values; a: 0°, b: 6°, c: 12°, d: 18°)

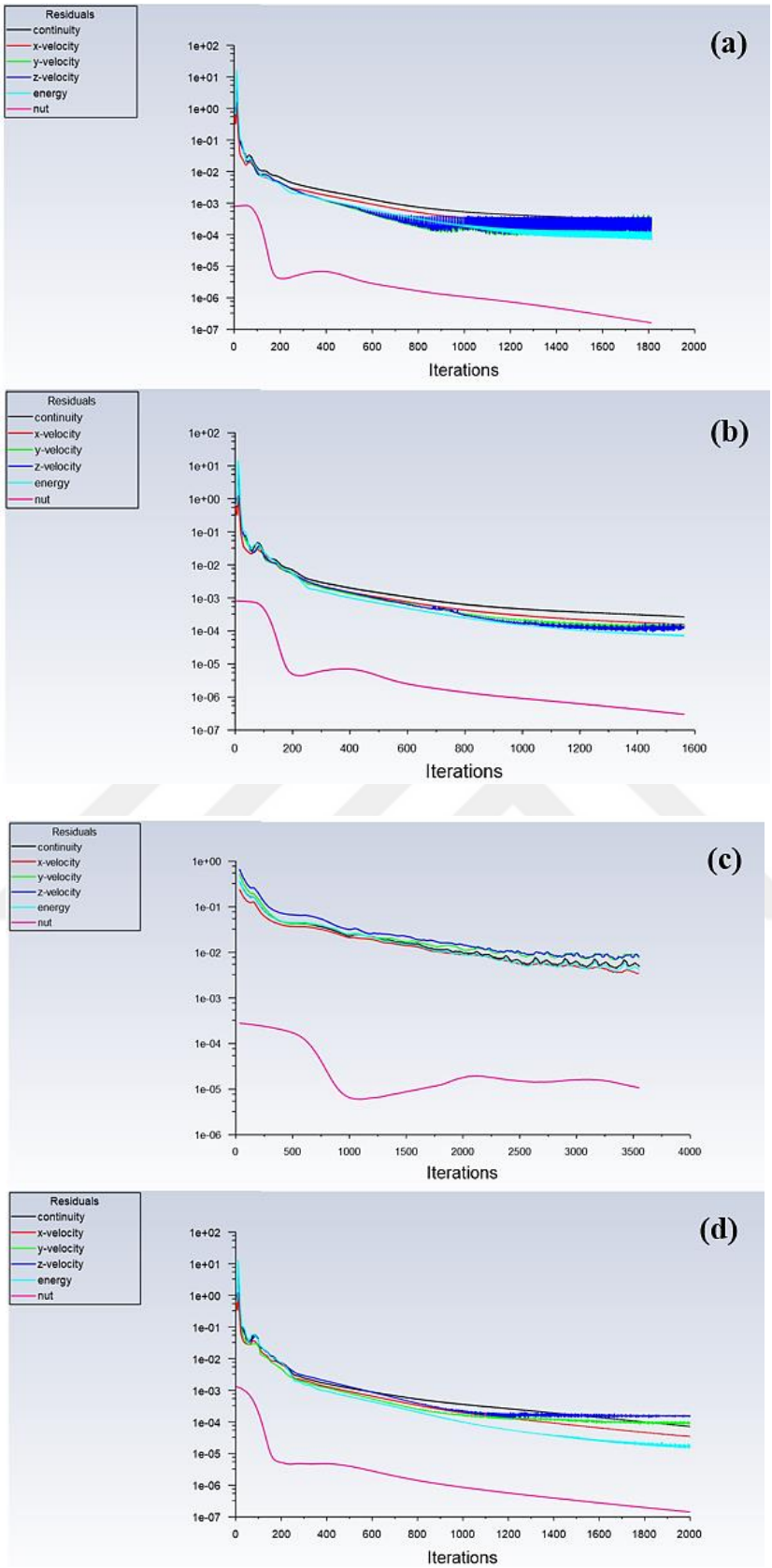


Figure 6.4 Residual values of angles of attack at Mach 2.5 in the Spalart-Allmaras turbulence model (AoA values; a: 0°, b: 6°, c: 12°, d: 18°)

In the solution with used k-ω, SST turbulence model at 0°, 6°, 12°, 18° AoA for Mach number 1.5, 2, 2.5, the residuals values are generated as x-y-z velocity, continuity, energy, k and ω. The residuals values are shown in the Figure 6.5 for Mach number 1.5, in the Figure 6.6 for Mach number 2 and in the Figure 6.7 for Mach number 2.5. Since the residual values remained constant at a certain sine wave for all data and were below 10^3, they were deemed sufficient for the solution.

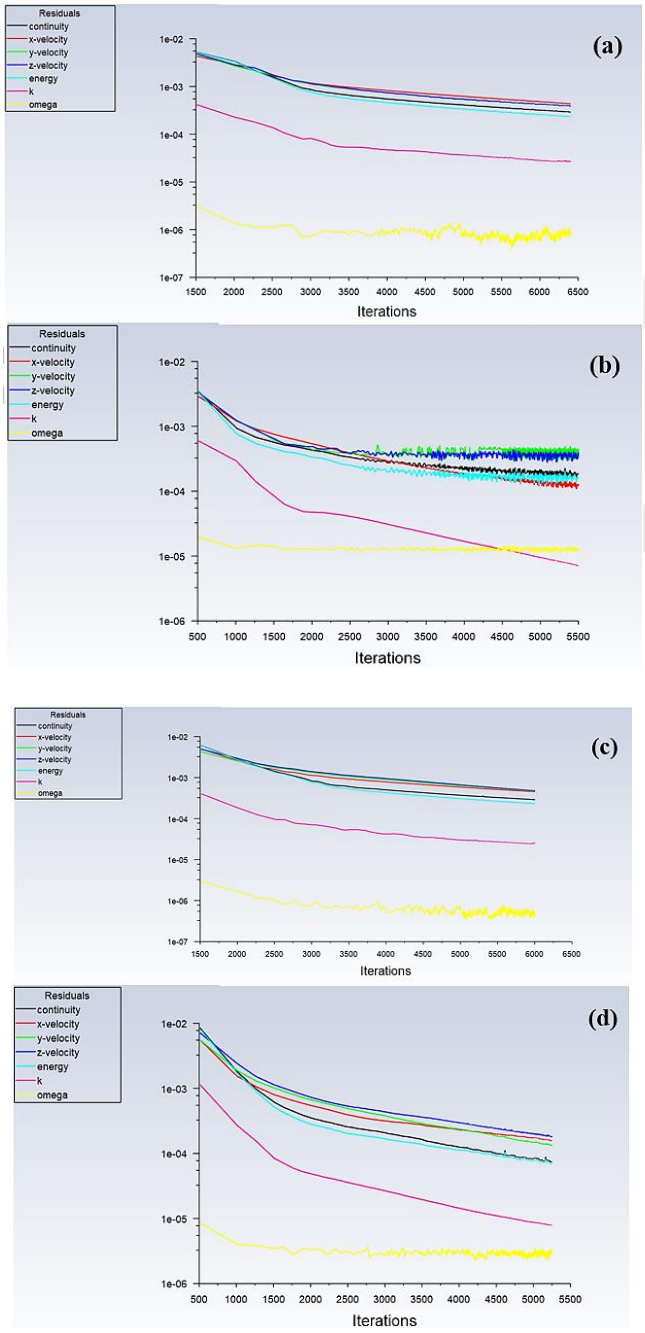


Figure 6.5 Residual values of angles of attack at Mach 1.5 in the k-ω, SST turbulence model (AoA values; a: 0°, b: 6°, c: 12°, d: 18°)

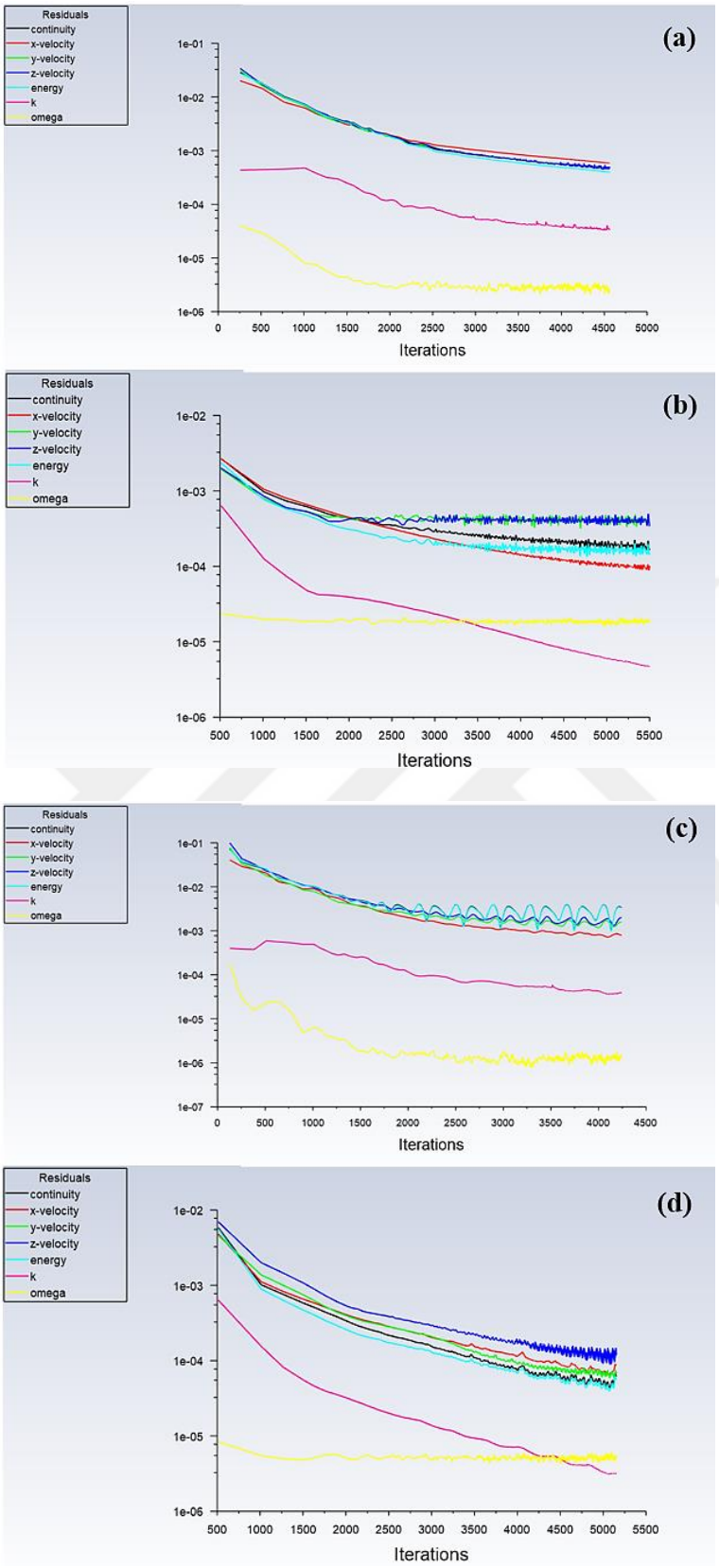


Figure 6.6 Residual values of angles of attack at Mach 2 in the k-ω, SST turbulence model (AoA values; a: 0°, b: 6°, c: 12°, d: 18°)

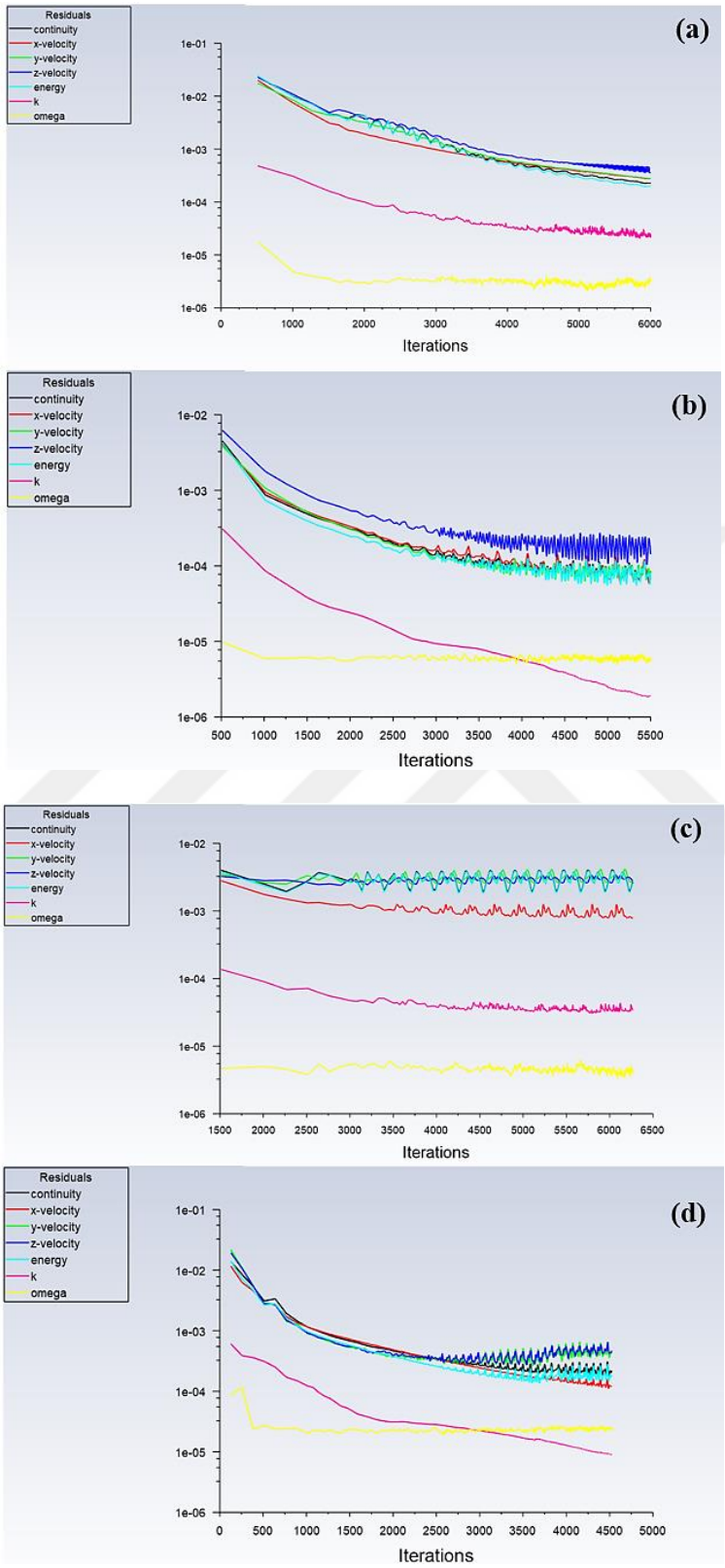


Figure 6.7 Residual values of angles of attack at Mach 2.5 in the k-ω, SST turbulence model (AoA values; a: 0°, b: 6°, c: 12°, d: 18°)

In the solution with used k-ε, Realizable turbulence model at 0°, 6°, 12°, 18° AoA for Mach number 1.5, 2, 2.5, the residuals values are generated as x-y-z velocity, continuity, energy, k and ε. The residuals values are shown in the Figure 6.8 for Mach number 1.5, in the Figure 6.9 for Mach number 2 and in the Figure 6.10 for Mach number 2.5. Since the residual values remained constant at a certain sine wave for all data and were below 10^3, they were deemed sufficient for the solution.

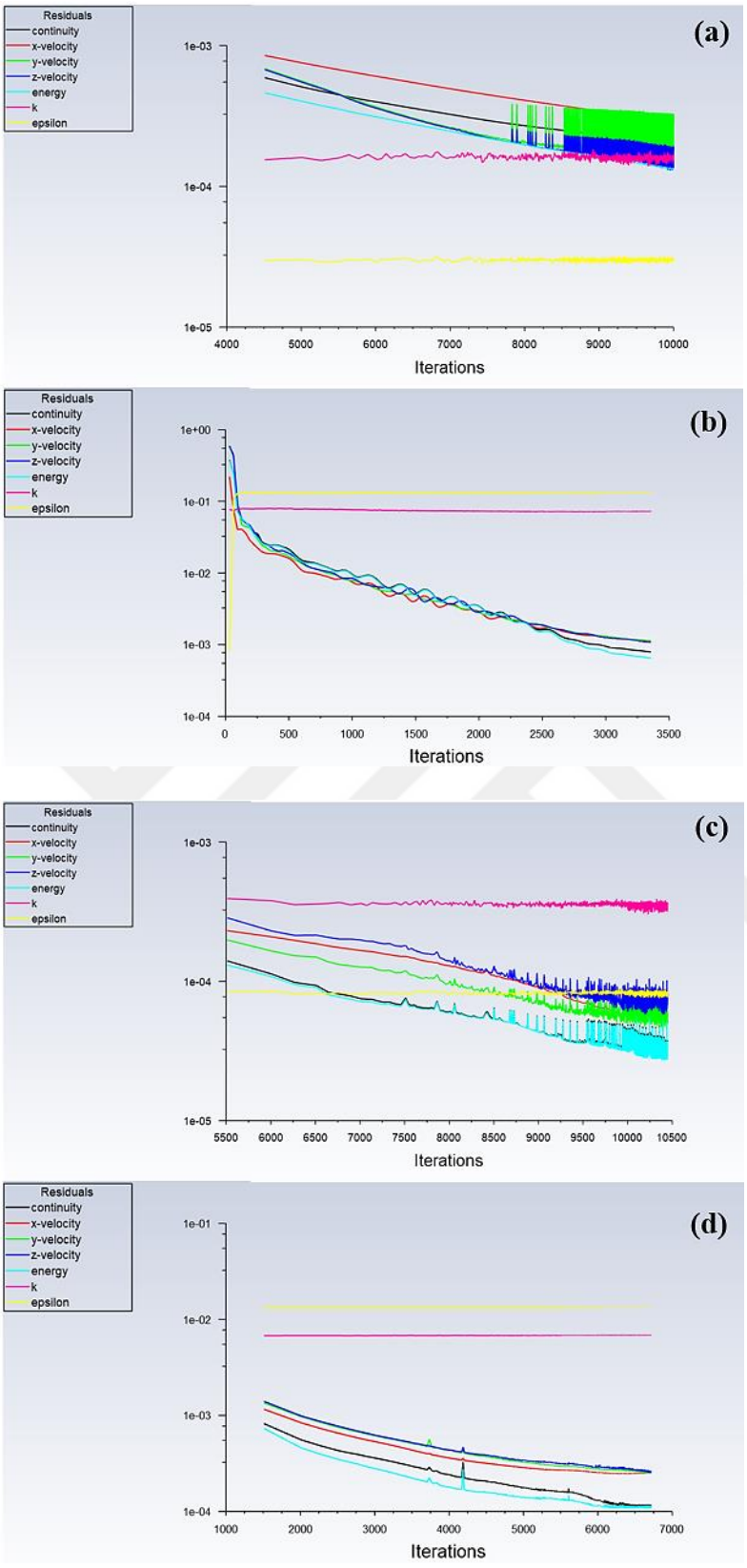


Figure 6.8 Residual values of angles of attack at Mach 1.5 in the k-ε, Realizable turbulence model (AoA values; a: 0°, b: 6°, c: 12°, d: 18°)

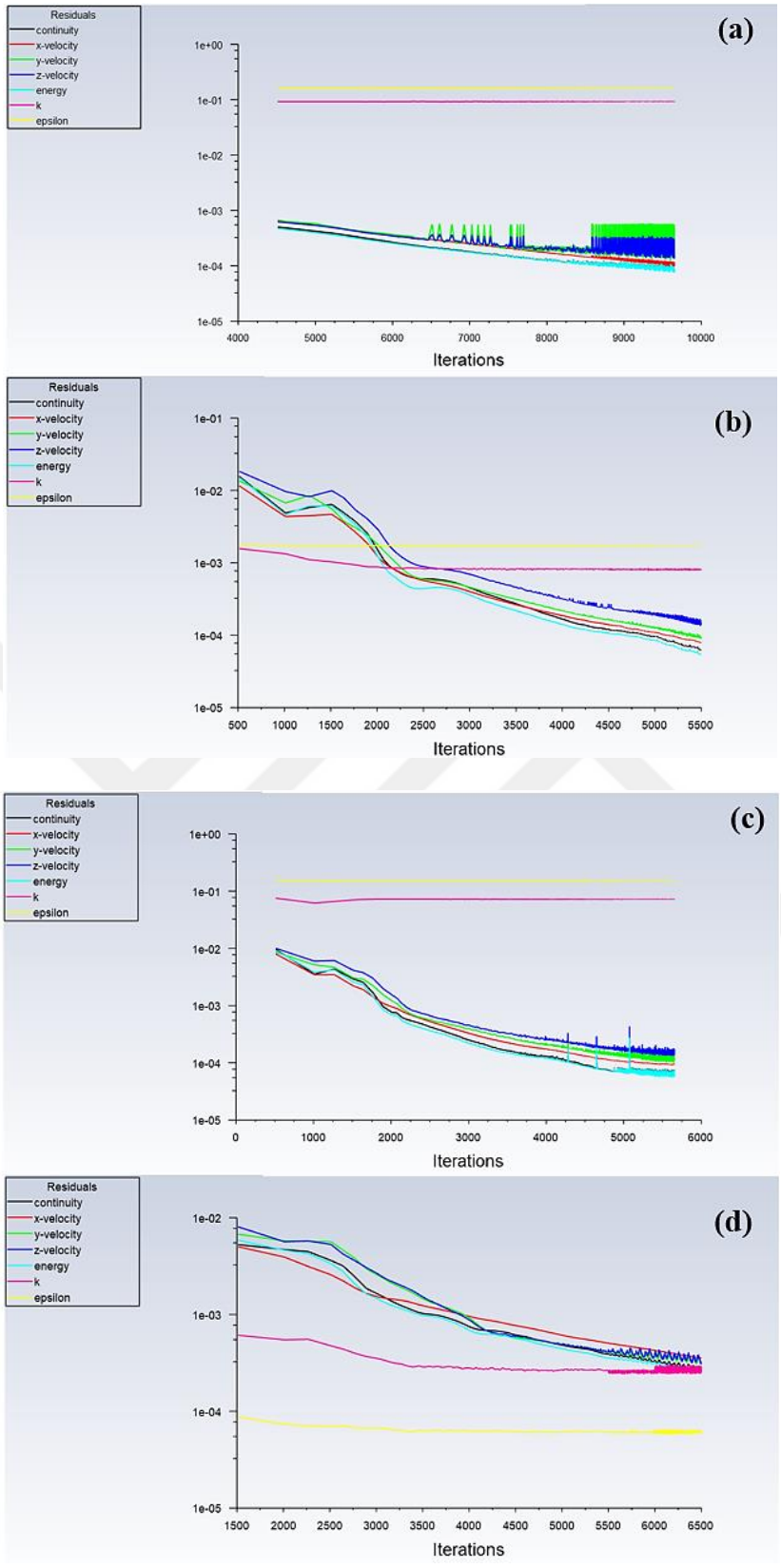


Figure 6.9 Residual values of angles of attack at Mach 2 in the k-ε, Realizable turbulence model (AoA values; a: 0°, b: 6°, c: 12°, d: 18°)

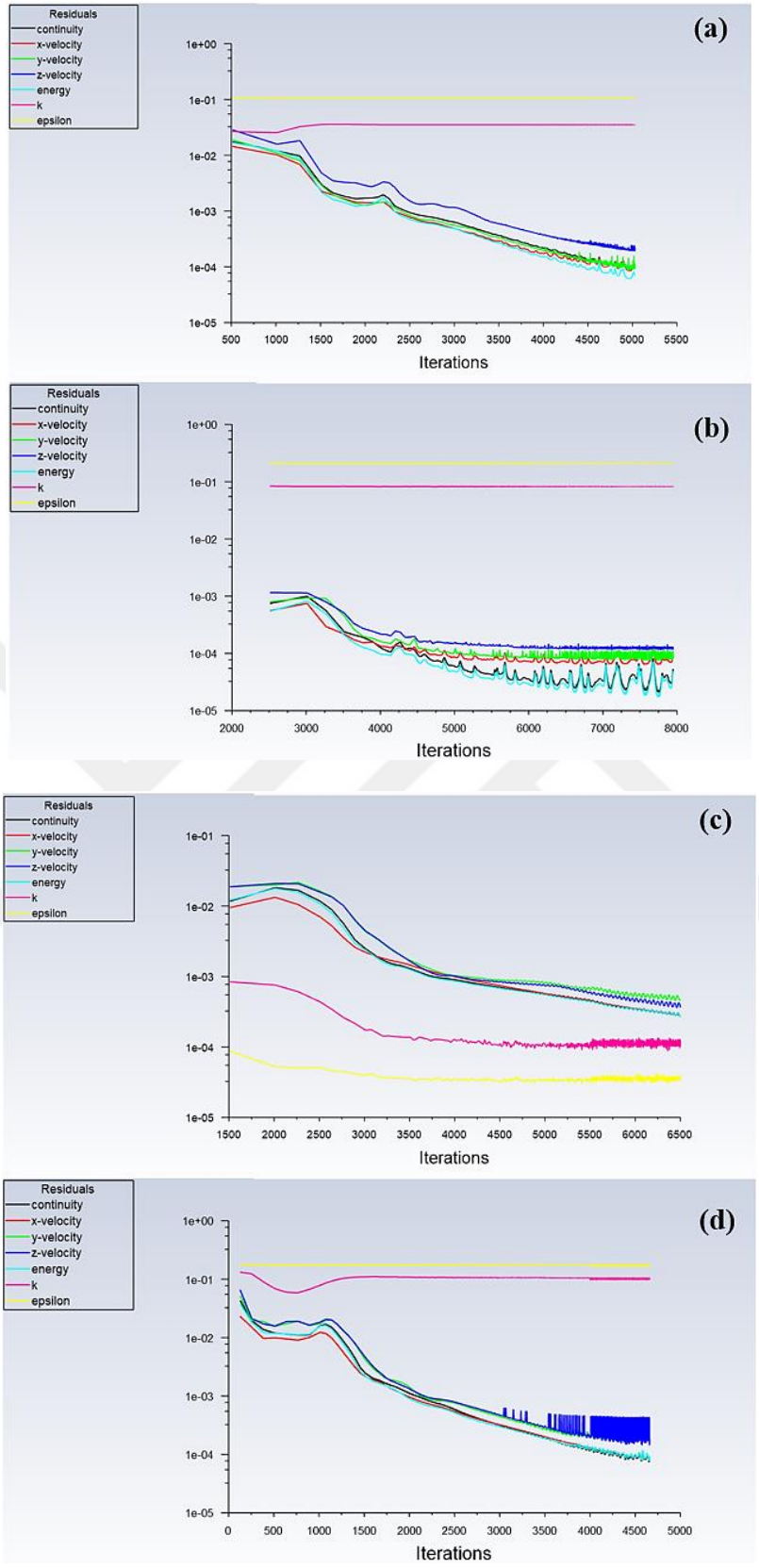


Figure 6.10 Residual values of angles of attack at Mach 2.5 in the k-ε, Realizable turbulence model (AoA values; a: 0°, b: 6°, c: 12°, d: 18°)

After the residual values were observed enough appropriate, the drag coefficient, lift coefficient and moment coefficient values of each turbulence model were examined separately for 0°, 6°, 12°, 18° AoA.

The comparison of the drag coefficient according to Mach numbers for turbulence models is given in Figure 6.11 for 0° AoA, in Figure 6.12 for 6° AoA, in Figure 6.13 for 12° AoA and in Figure 6.14 for 18° AoA.

Figure 6.11 shows that the drag coefficient at 0° AoA is at a minimum at 1.5 Mach in the k-ω, SST and Spalart-Allmaras model, and increases significantly at 2 Mach, while it decreases in the k-ε, Realizable turbulence model. While it was observed that the drag coefficient increased when the supersonic speed increased to 2.5 Mach in the k-ω, SST turbulence models, this value decreased in the k-ε, Realizable and Spalart-Allmaras models.

Figure 6.12 shows that at 6° AoA, the drag coefficient is at its minimum at 1.5 Mach and increases significantly at 2 Mach. While it is observed that the drag coefficient decreases as the supersonic speed increases to 2.5 Mach in the k-ω, SST turbulence model, this value increases in the Spalart-Allmaras and k-ε, Realizable models and the values are close to each other in all three turbulence models at 2.5 Mach.

Figure 6.13 shows that the drag coefficient at 18° AoA increases in the transition from 1.5 Mach to 2 Mach in the Spalart-Allmaras and k-ε, Realizable turbulence models but decreases in the k-ω, SST turbulence model. It is seen that all three turbulence models decrease when transition to Mach 2.5 and the values are close to each other.

In Figure 6.14, it is observed that the drag coefficient increases significantly in the transition from 1.5 to 2.5 Mach at 18° AoA in the k-ε, Realizable and k-ω, SST turbulence models, while it decreases in the Spalart-Allmaras turbulence model.

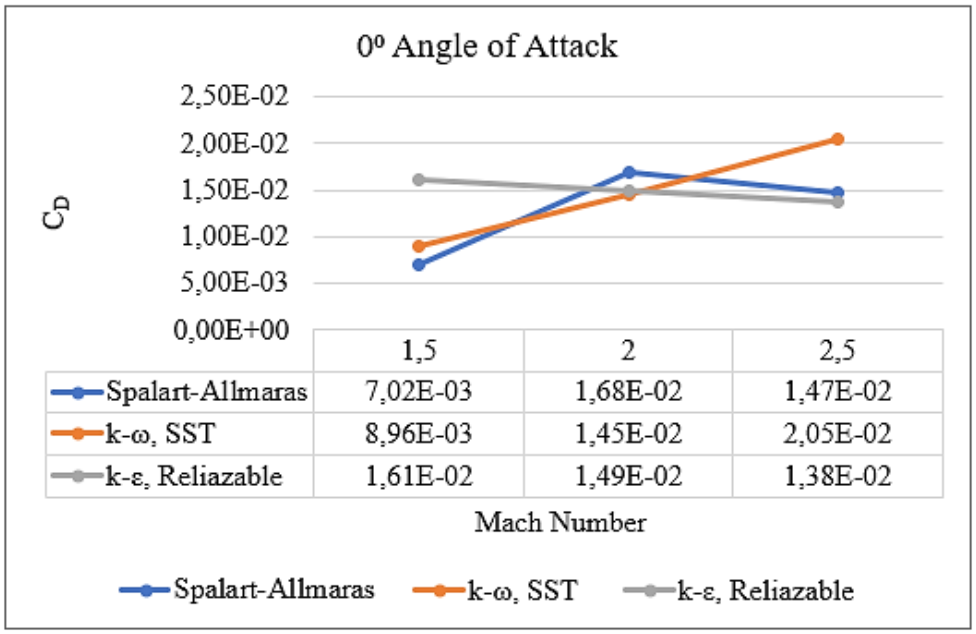


Figure 6.11 Comparison of the C_D at 0° AoA for the k-ε, Realizable, Spalart-Allmaras, k-ω, SST turbulence models at Mach Numbers 1.5, 2, 2.5

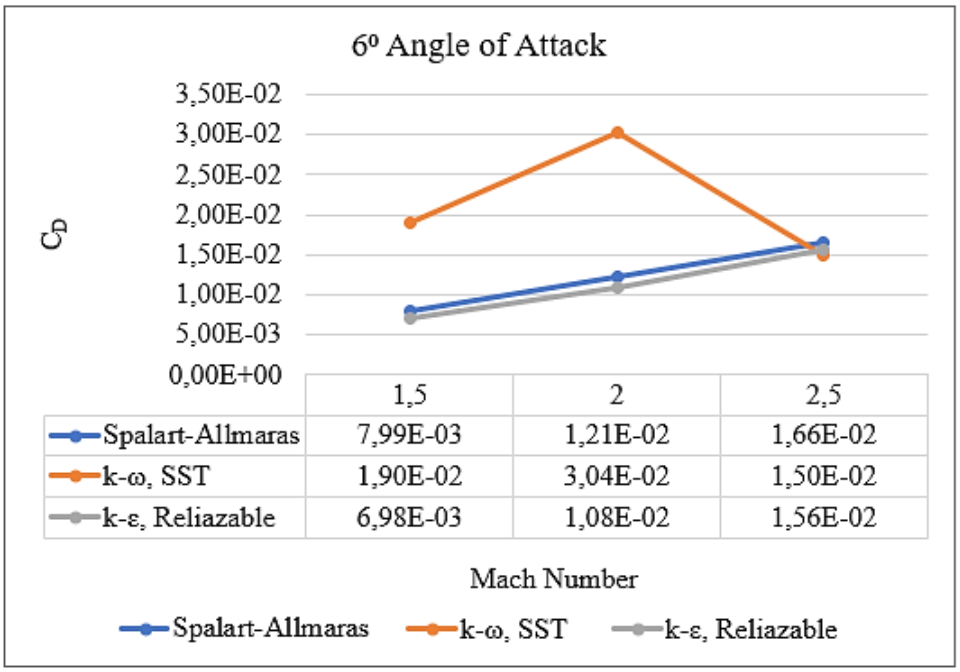


Figure 6.12 Comparison of the C_D at 6° AoA for the k-ε, Realizable, Spalart-Allmaras, k-ω, SST turbulence models at Mach Numbers 1.5, 2, 2.5

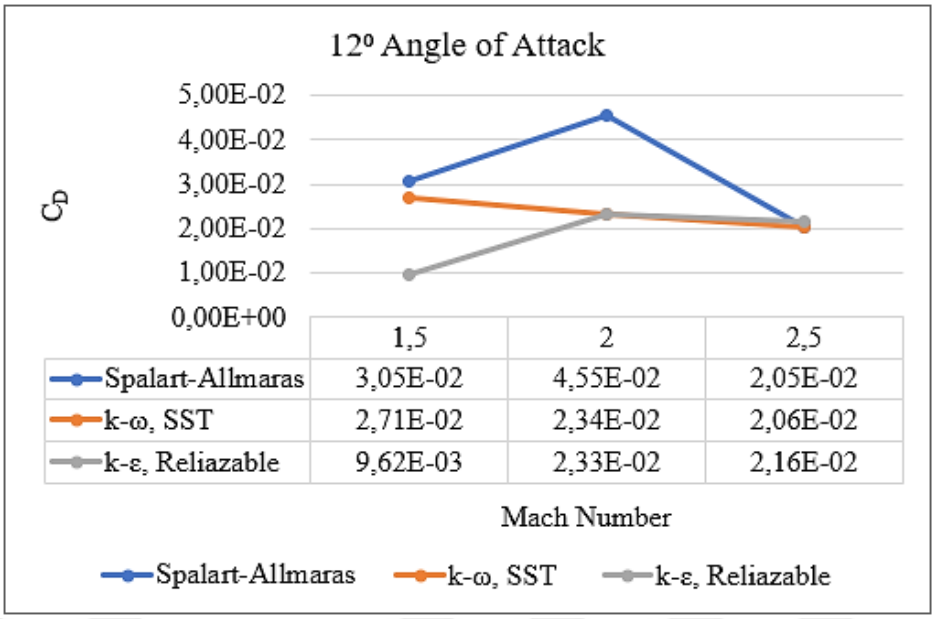


Figure 6.13 Comparison of the C_D at 12° AoA for the k-ε, Realizable, Spalart-Allmaras, k-ω, SST turbulence models at Mach Numbers 1.5, 2, 2.5

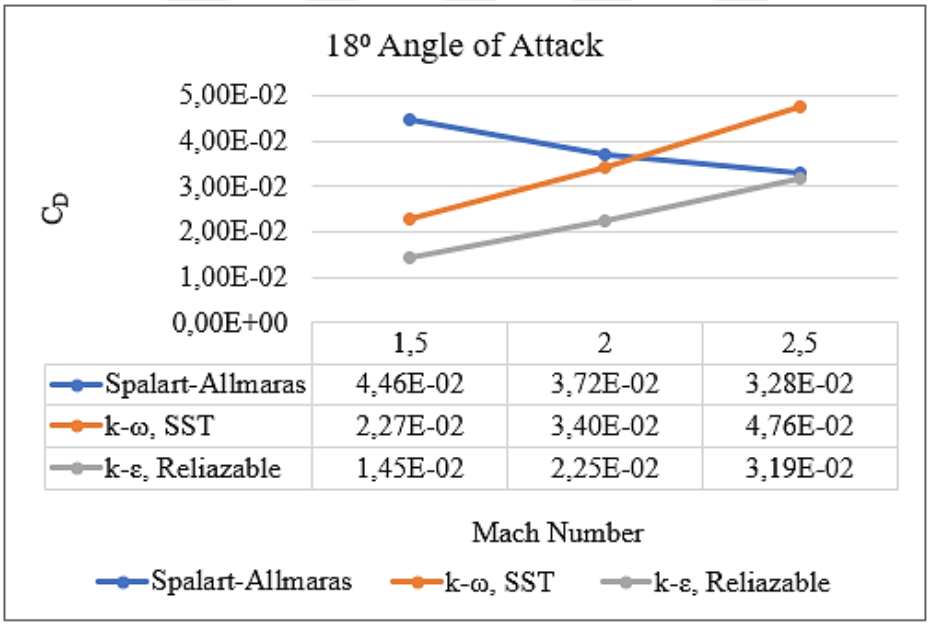


Figure 6.14 Comparison of the C_D at 18° AoA for the k-ε, Realizable, Spalart-Allmaras, k-ω, SST turbulence models at Mach Numbers 1.5, 2, 2.5

Comparison of lift coefficient according to Mach numbers for turbulence models is given in Figure 6.15 for 6° AoA, Figure 6.16 for 12° AoA, and Figure 6.17 for 18° AoA. At 0° AoA, the lift force is zero because the missile continues its flight only in the axial direction.

Figure 6.15 shows that at 6° AoA the lift coefficient is at its minimum at 1.5 Mach and increases significantly at 2 Mach. While it was observed that the lift coefficient decreased as the supersonic speed increased to 2.5 Mach in the k-ω, SST turbulence model, this value increased in the k-ε, Realizable turbulence model and the Spalart-Allmaras model.

Figure 6.16 shows that in the transition from 1.5 Mach to 2 Mach at 12° AoA, the lift coefficient increases significantly in the k-ε, Realizable turbulence model and the Spalart-Allmaras model, while it decreases in the k-ω, SST turbulence model. A decrease in the lift coefficient was observed in each turbulence model during the transition to Mach 2.5, and it was determined that the values were close to each other.

In Figure 6.17, it is seen that the lift coefficient at 18° AoA increases in the transition from 1.5 Mach to 2.5 Mach in the k-ω, SST and k-ε, Realizable turbulence models and decreases in the Spalart-Allmaras turbulence model.

When the drag coefficient graphs are compared with the lift coefficient graphs, a similar graph emerges and the values are seen to be consistent.

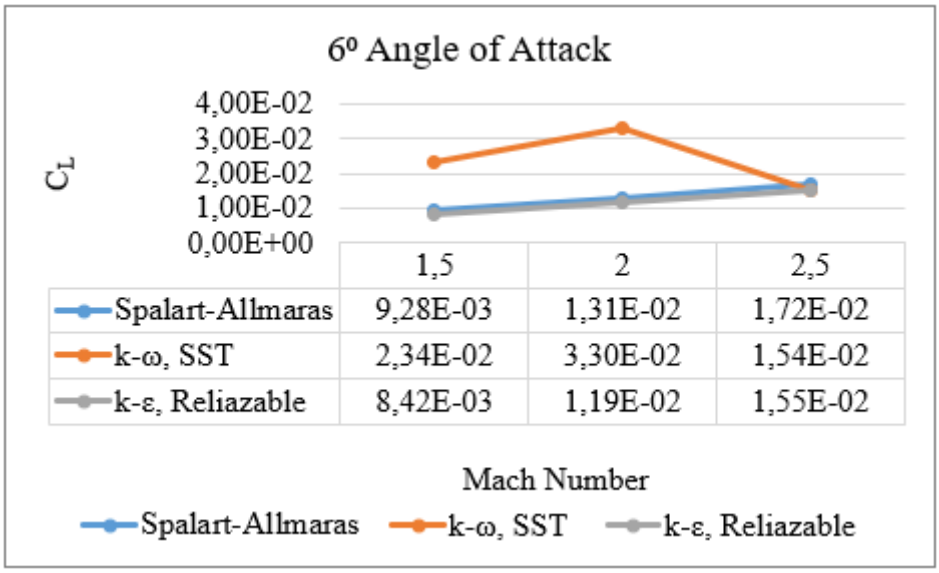


Figure 6.15 Comparison of the C_L at 6° AoA for the k-ε, Realizable, Spalart-Allmaras, k-ω, SST turbulence models at Mach Numbers 1.5, 2, 2.5

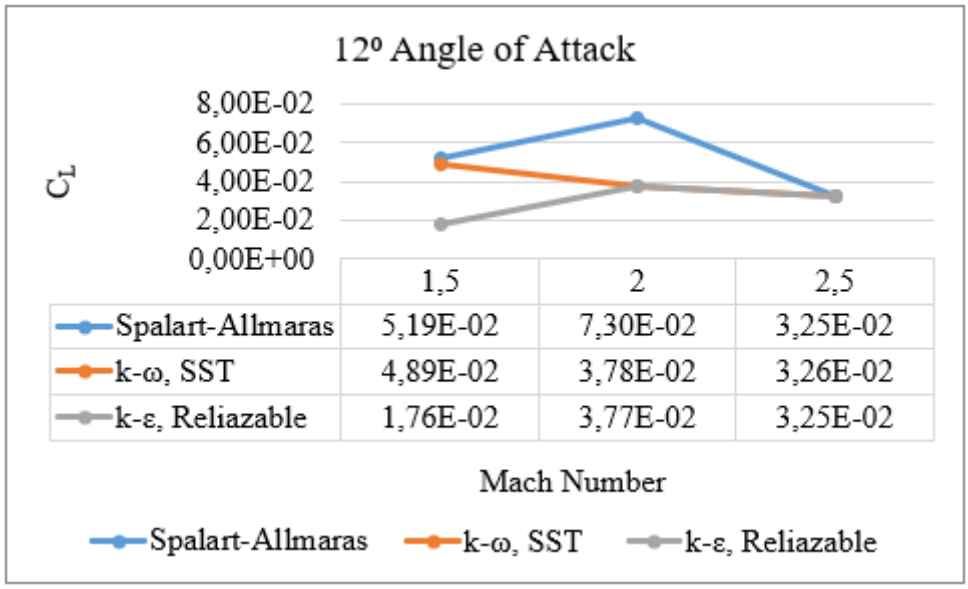


Figure 6.16 Comparison of the C_L at 12° AoA for the k-ε, Realizable, Spalart-Allmaras, k-ω, SST turbulence models at Mach Numbers 1.5, 2, 2.5

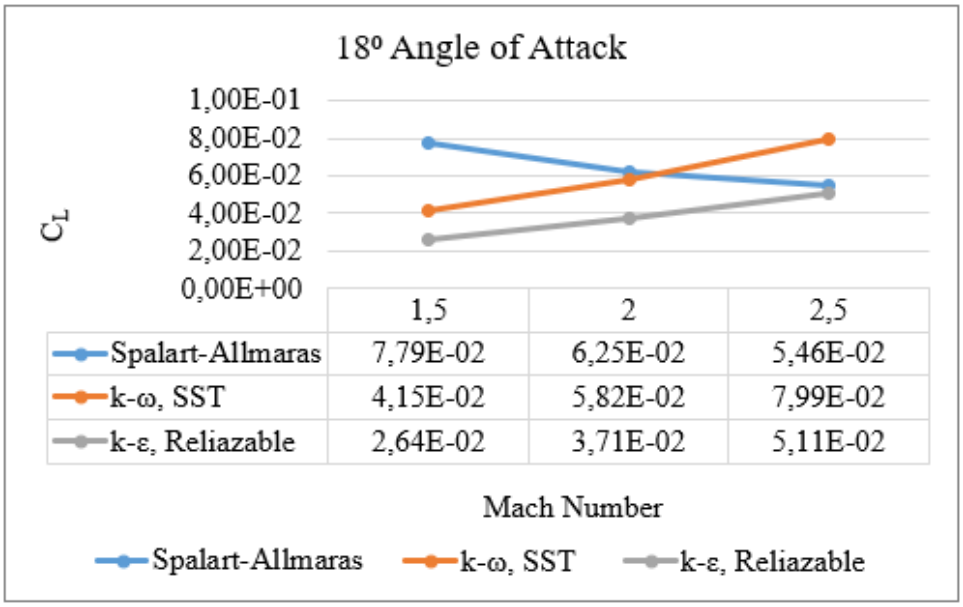


Figure 6.17 Comparison of the C_L at 18° AoA for the k-ε, Realizable, Spalart-Allmaras, k-ω, SST turbulence models at Mach Numbers 1.5, 2, 2.5

Comparison of moment coefficient for turbulence models according to Mach numbers is given in Figure 6.18 for 6° AoA, in Figure 6.19 for 12° AoA and in Figure 6.20 for 18° AoA. At 0° AoA, the moment force of the missile is zero as the missile continues its flight only in the axial direction.

Figure 6.18 shows that at 6° AoA the moment coefficient is at its minimum at 1.5 Mach and increases significantly at 2 Mach. While it was observed that the moment coefficient decreased as the supersonic speed increased to 2.5 Mach in the k-ω, SST turbulence model, this value increased in the k-ε, Realizable turbulence model and the Spalart-Allmaras model.

Figure 6.19 shows that in the transition from 1.5 Mach to 2 Mach at 12° AoA, the moment coefficient increases significantly in the k-ε, Realizable turbulence model and the Spalart-Allmaras model, while it decreases in the k-ω, SST turbulence model. A decrease in the moment coefficient was observed in each turbulence model during the transition to Mach 2.5, and it was determined that the values were close to each other.

In Figure 6.20, it is seen that the moment coefficient at 18° AoA increases in the transition from 1.5 Mach to 2.5 Mach in the k-ω, SST and k-ε, Realizable turbulence models and decreases in the Spalart-Allmaras turbulence model.

When the drag coefficient and lift coefficient graphs are compared with the moment coefficient graphs, similar graphs emerges and the values are seen to be consistent.

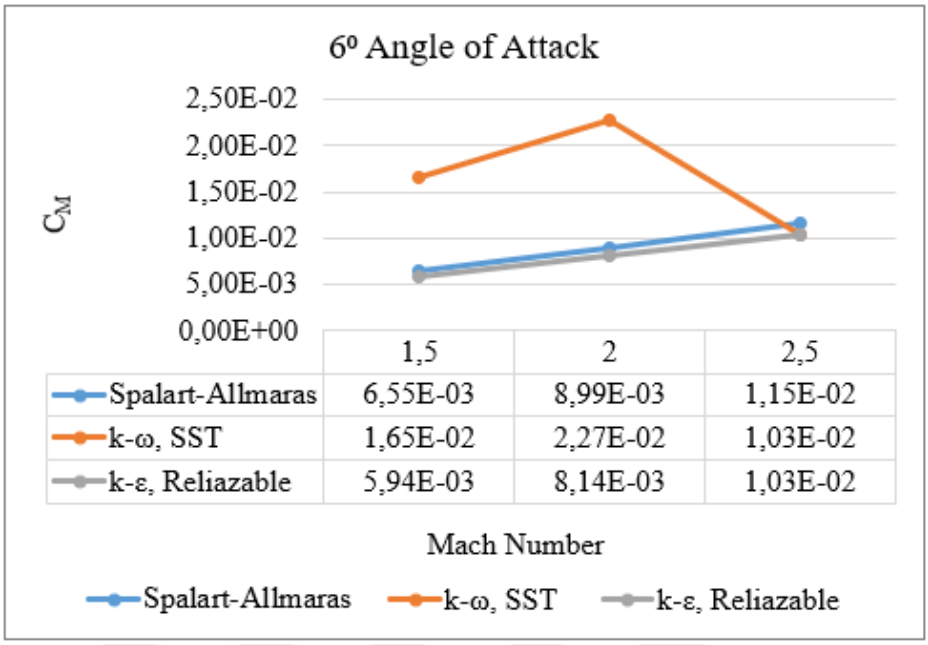


Figure 6.18 Comparison of the C_M at 6° AoA for the k-ε, Realizable, Spalart-Allmaras, k-ω, SST turbulence models at Mach Numbers 1.5, 2, 2.5

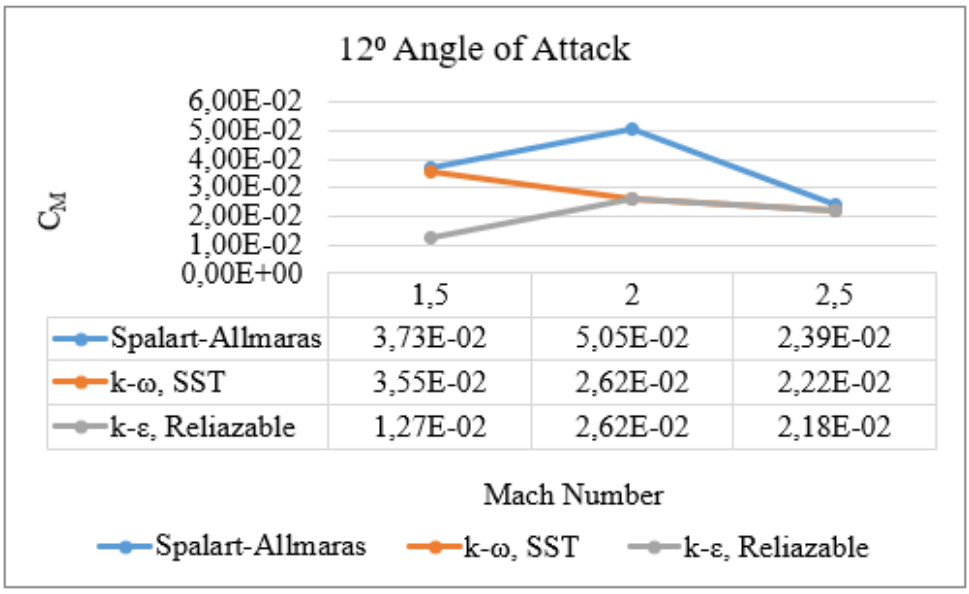


Figure 6.19 Comparison of the C_M at 12° AoA for the k-ε, Realizable, Spalart-Allmaras, k-ω, SST turbulence models at Mach Numbers 1.5, 2, 2.5

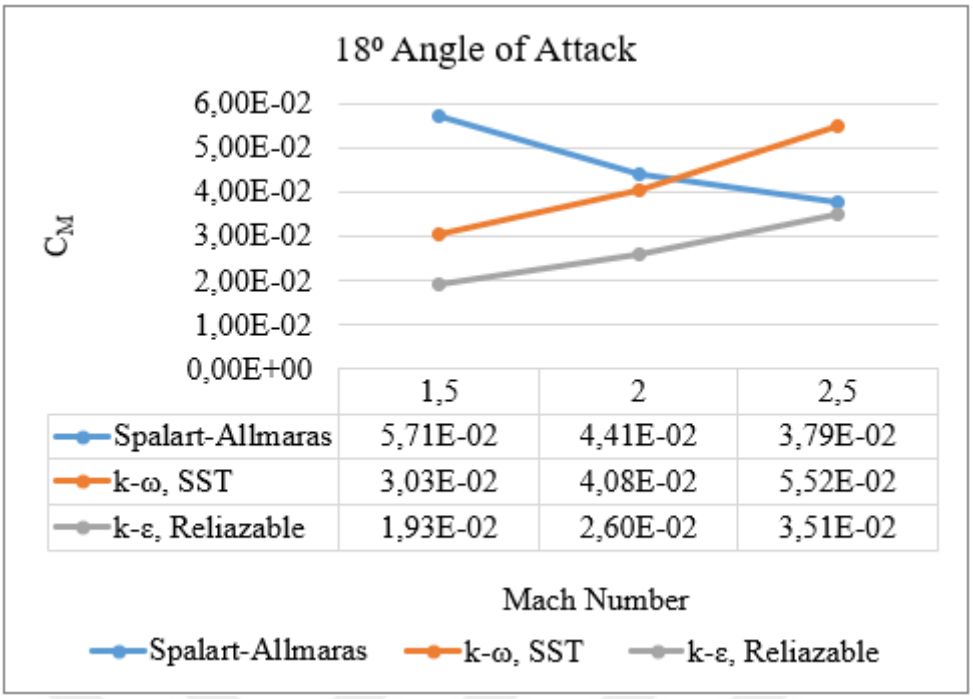


Figure 6.20 Comparison of the C_M at 18° AoA for the k-ε, Realizable, Spalart-Allmaras, k-ω, SST turbulence models at Mach Numbers 1.5, 2, 2.5

The missile's mach contours are displayed to demonstrate how the mach affects the wings, body, and tail of the missile as well as how the flow separates.

Mach contours and Mach values in the Spalart-Allmaras turbulence model are displayed in Figure 6.21 for Mach 1.5, in Figure 6.22 for Mach 2, in Figure 6.23 for Mach 2.5; in the k-ω, SST turbulence model are displayed in Figure 6.24 for Mach 1.5, in Figure 6.25 for Mach 2, in Figure 6.26 for Mach 2.5; in the k-ε, Realizable turbulence model are displayed in Figure 6.27 for Mach 1.5, in Figure 6.28 for Mach 2, in Figure 6.29 for Mach 2.5. When all figures are examined, it can be seen that when the AoA increases, the missile tends to lift in the upward direction, while the drag force in the upward direction increases, and it is exposed to the downward lift force.

Each turbulence model has four cases representing the AoA between 0° and 18° for each Mach number. When all figures are examined, it can be seen that when the AoA increases, the missile tends to lift in the upward direction, while the drag force increases in the upward direction, the Mach number is at its maximum. The Mach number decreases relatively while the lift force increases in the downward direction. The missile's base and nose tip have the lowest Mach numbers. It is

observed that the Mach number differential between the missile nose's upper and lower surfaces rises along with the missile's Mach number. Furthermore, the shock waves' angle between the wave and the missile body decreases as the Mach number rises. Additionally, as AoA increases, the pressure in the lower part of the caudal fin also increases. The low Mach region is visible behind the missile. As the AoA increases, this region stays upward. As a result, the upper and lower portions experience greater pressure differences, which raises the C_L/C_D ratio.

When the Spalart-Allmaras model is compared with the k-ω, SST turbulence model and k-ε, Realizable turbulence model, it is obvious that the single-equation Spalart-Allmaras model cannot calculate the disturbances on the missile surface. It apparent from the Mach number contours that the k-ε, Realizable Enhance Wall Threatment turbulence model and k-ω, SST turbulence model are more suitable for wall calculations.

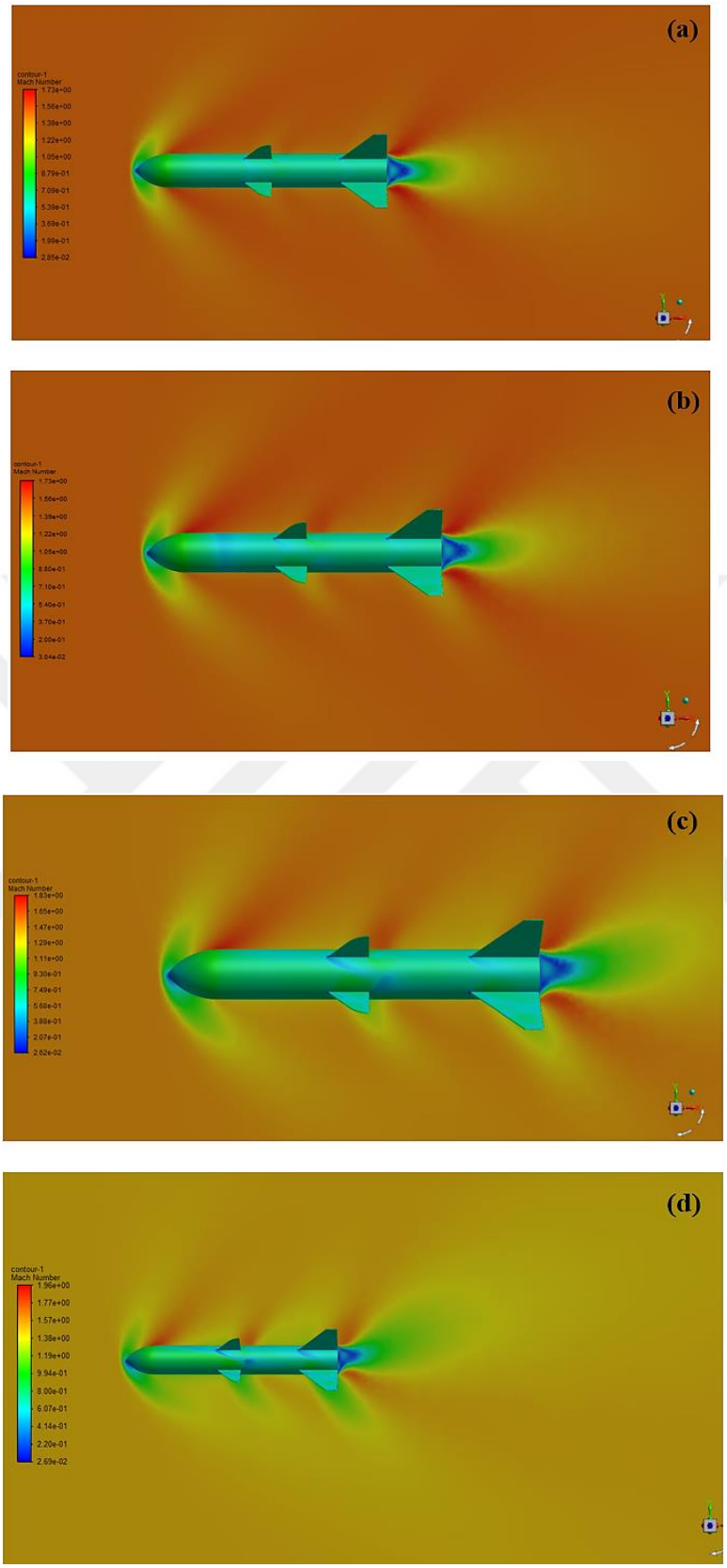


Figure 6.21 Mach contours of angles of attack at Mach 1.5 in the Spalart-Allmaras turbulence model (AoA values; a: 0°, b: 6°, c: 12°, d: 18°)

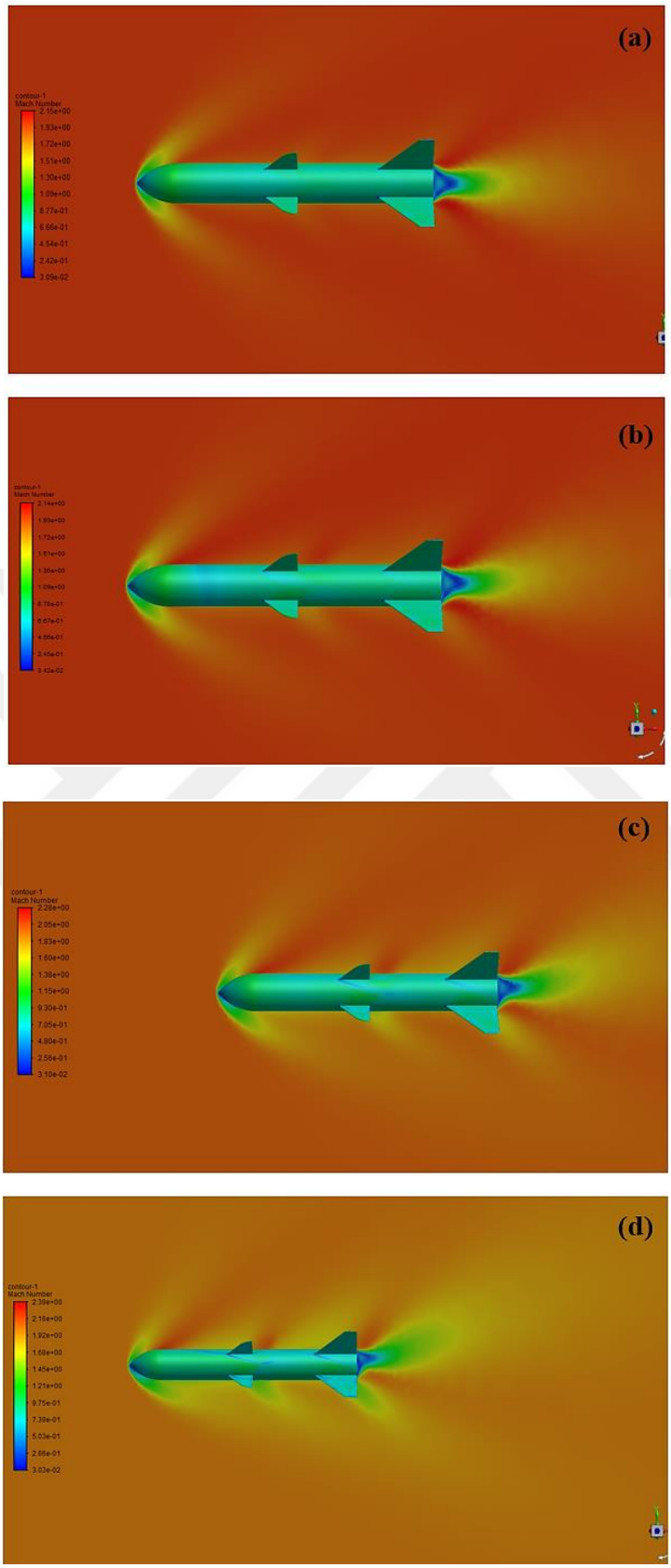


Figure 6.22 Mach contours of angles of attack at Mach 2 in the Spalart-Allmaras turbulence model (AoA values; a: 0°, b: 6°, c: 12°, d: 18°)

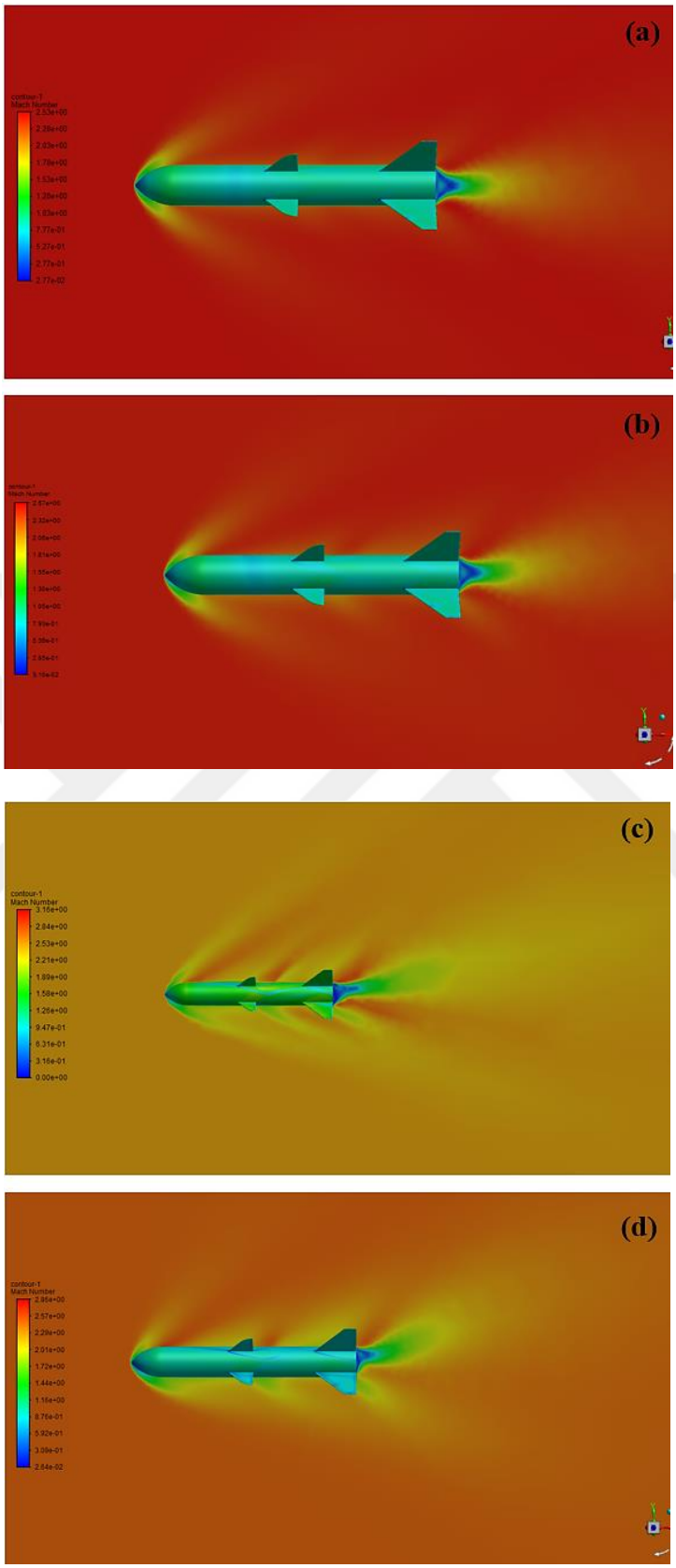


Figure 6.23 Mach contours of angles of attack at Mach 2.5 in the Spalart-Allmaras turbulence model (AoA values; a: 0°, b: 6°, c: 12°, d: 18°)

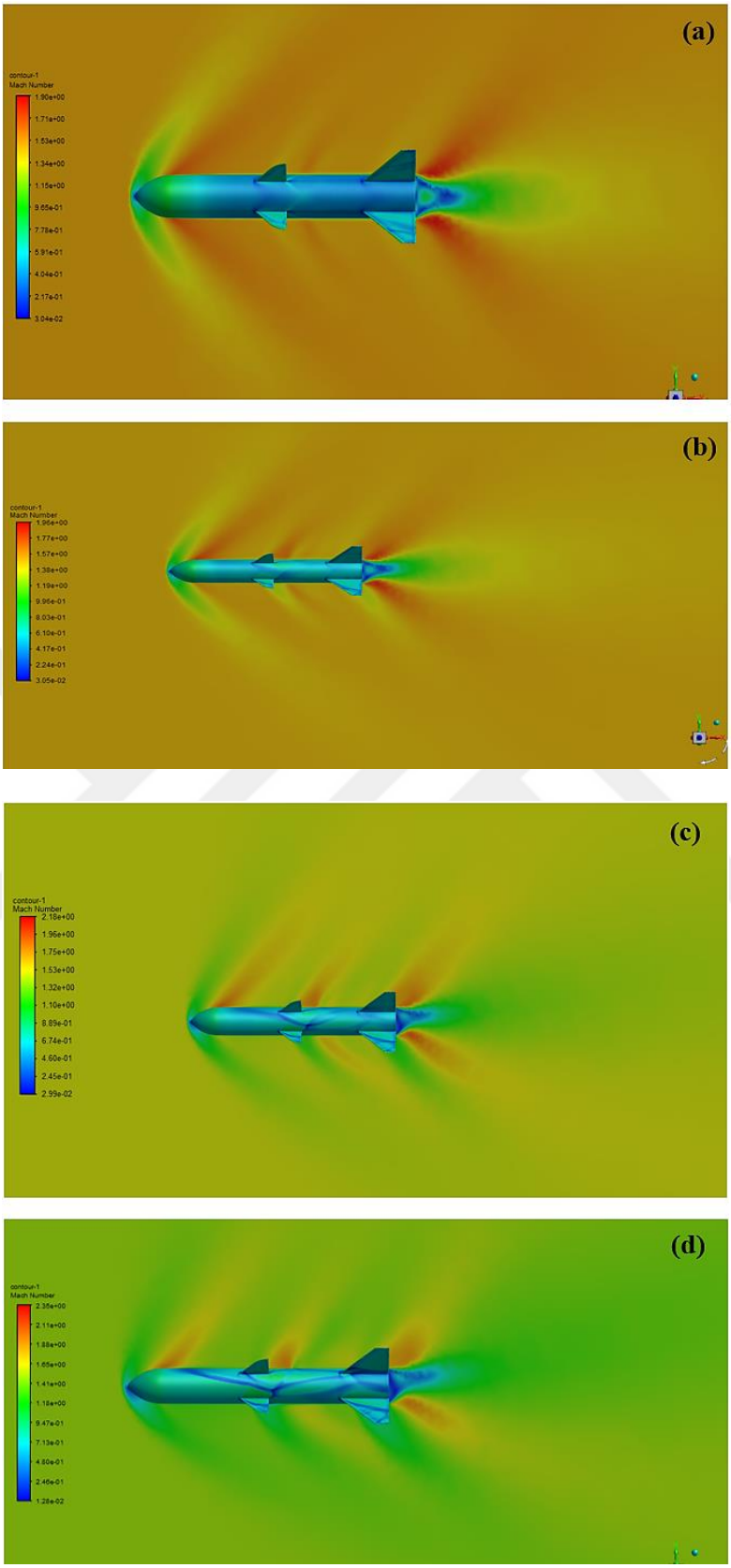


Figure 6.24 Mach contours of angles of attack at Mach 1.5 in the k-ω, SST turbulence model (AoA values; a: 0°, b: 6°, c: 12°, d: 18°)

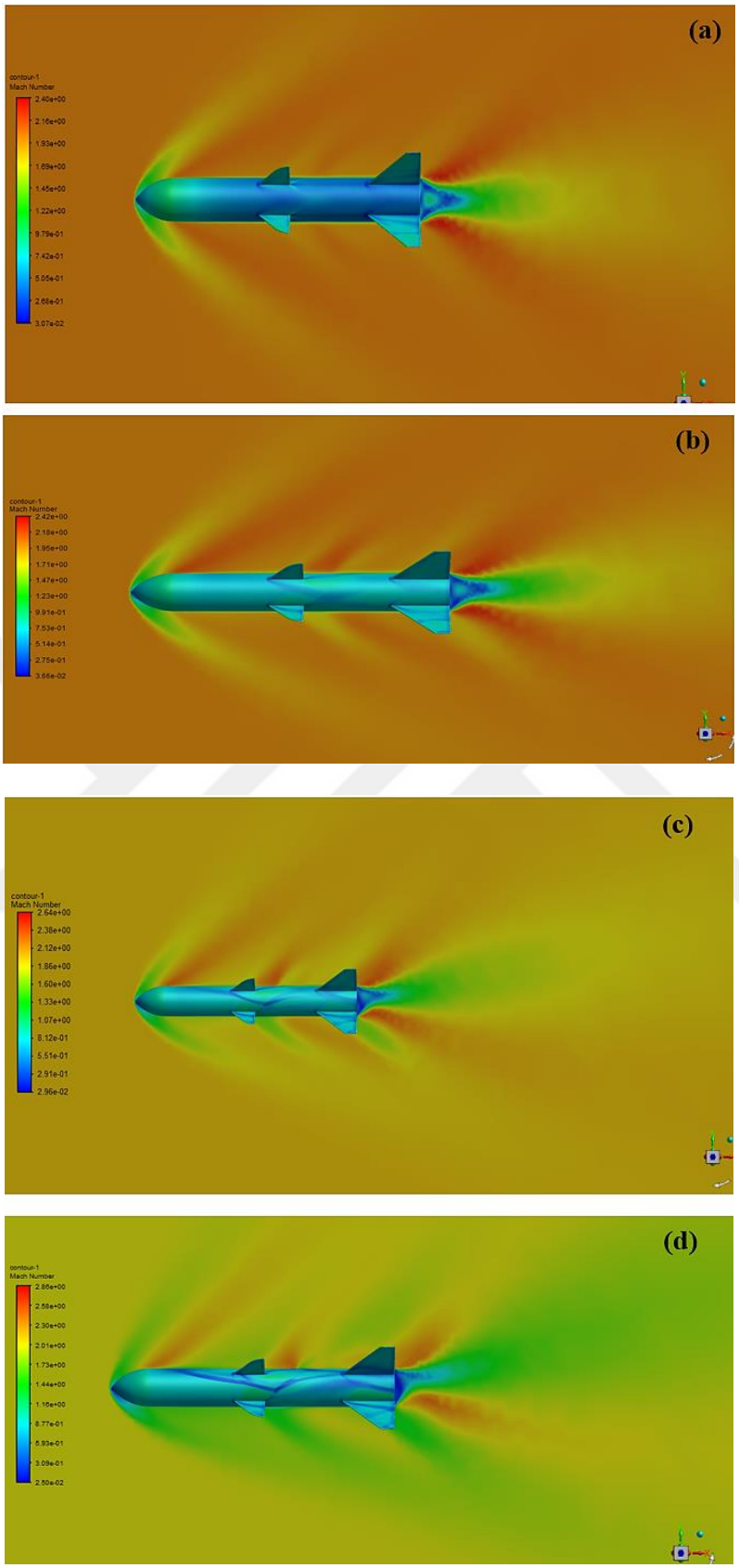


Figure 6.25 Mach contours of angles of attack at Mach 2 in the k-ω, SST turbulence model (AoA values; a: 0°, b: 6°, c: 12°, d: 18°)

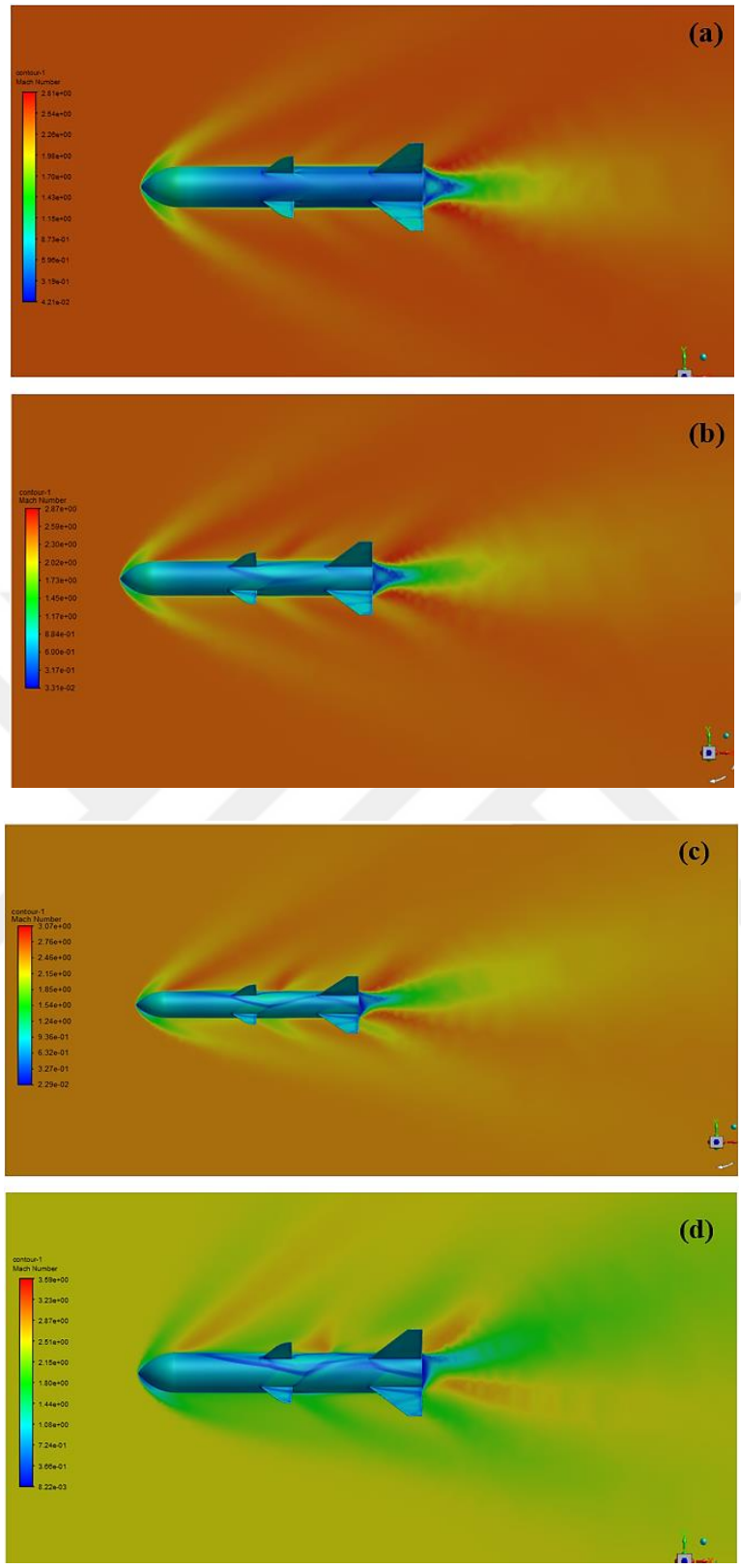


Figure 6.26 Mach contours of angles of attack at Mach 2.5 in the k-ω, SST turbulence model (AoA values; a: 0°, b: 6°, c: 12°, d: 18°)

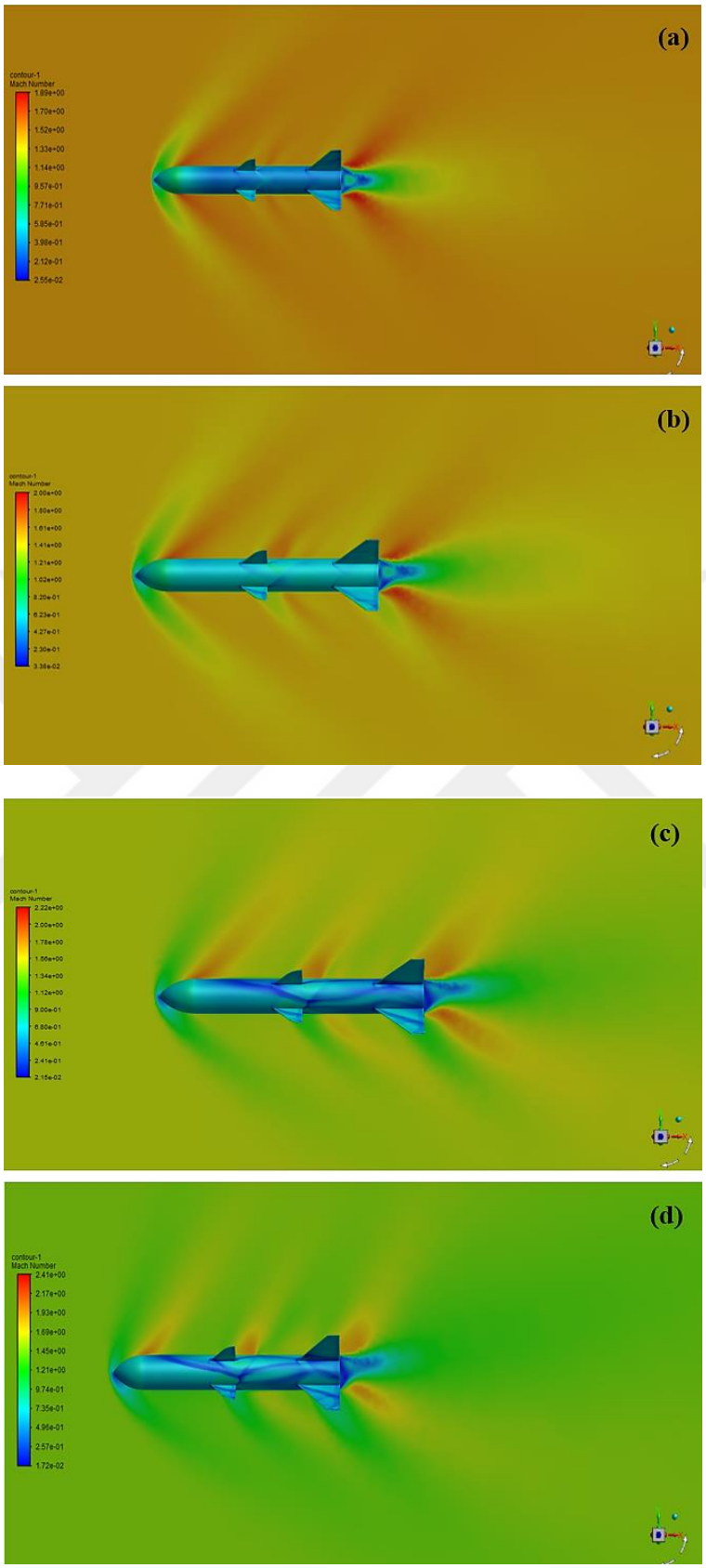


Figure 6.27 Mach contours of angles of attack at Mach 1.5 in the k-ε, Realizable turbulence model (AoA values; a: 0°, b: 6°, c: 12°, d: 18°)

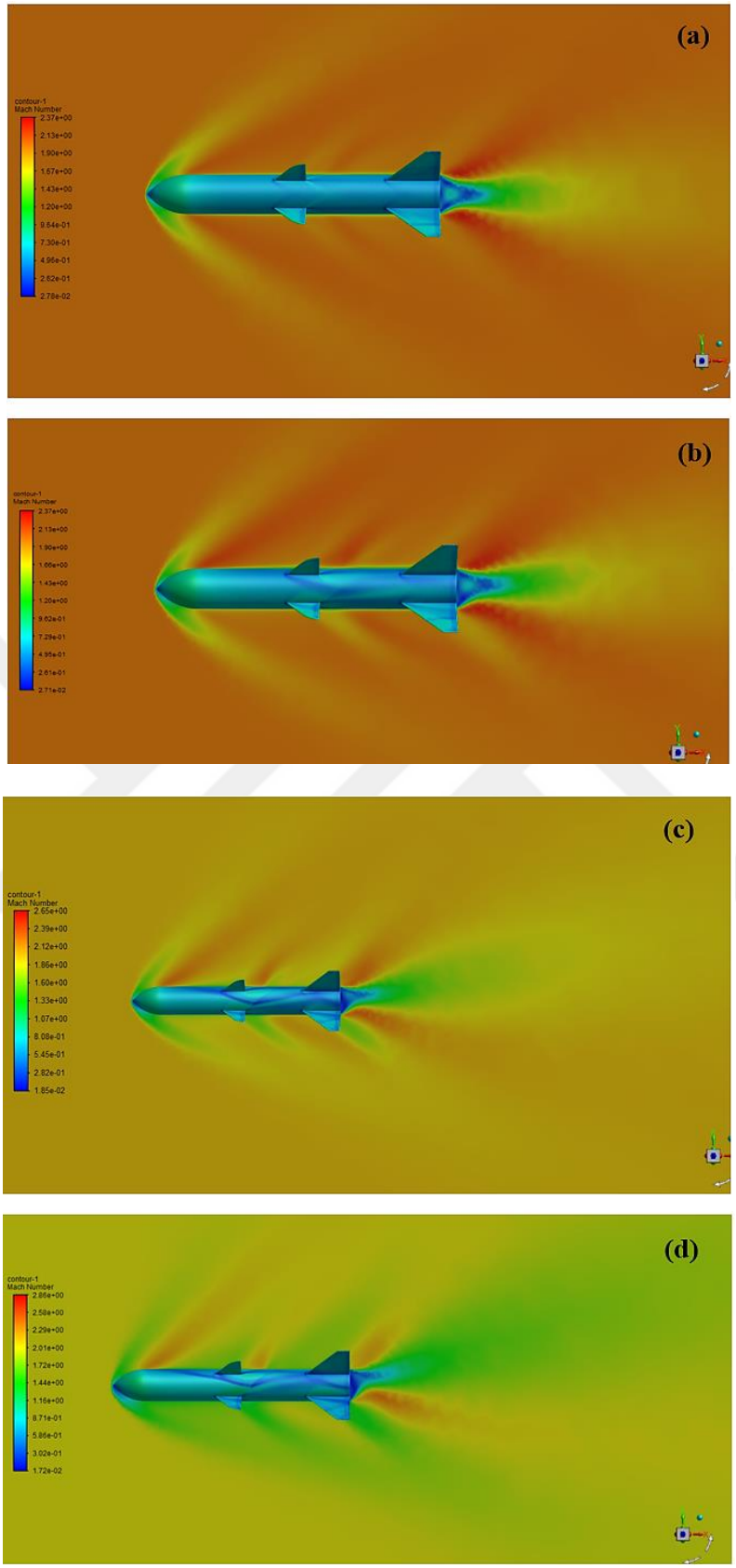


Figure 6.28 Mach contours of angles of attack at Mach 2 in the k-ε, Realizable turbulence model (AoA values; a: 0°, b: 6°, c: 12°, d: 18°)

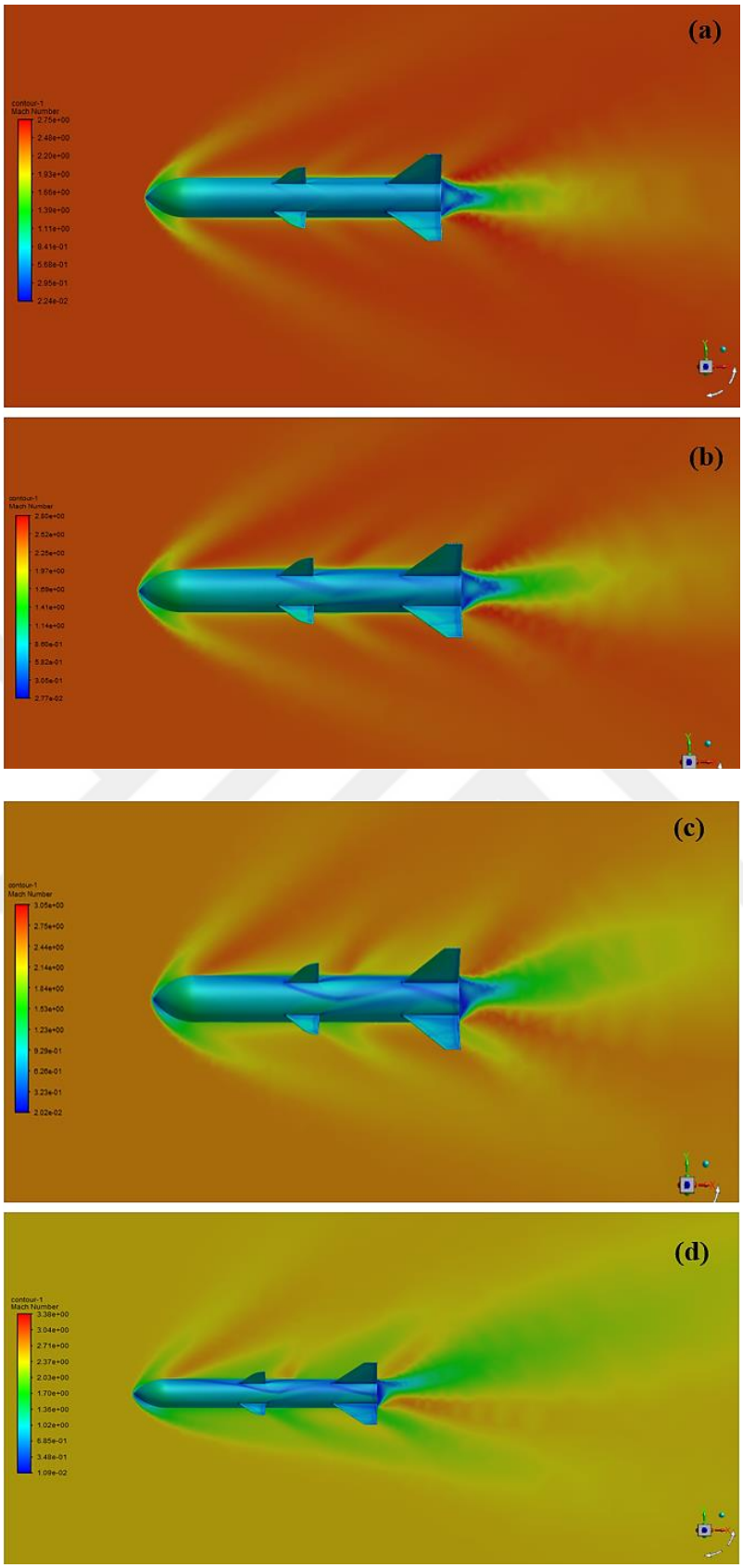


Figure 6.29 Mach contours of angles of attack at Mach 2.5 in the k-ε, Realizable turbulence model (AoA values; a: 0°, b: 6°, c: 12°, d: 18°)

To demonstrate how to alter missile performance at high AoA, the C_L/C_D is shown in the Figure 6.30 for Spalart-Allmaras turbulence model, in the Figure 6.31 for k-ω, SST turbulence model and in the Figure 6.32 for k-ε, Realizable turbulence model represent the C_L/C_D versus 6°, 12° and 18° AoA at the 1.5, 2 and 2.5 Mach numbers. As the Mach number increases, the lift/drag ratio also increases.

Figure 6.30, Figure 6.31 and Figure 6.32 show that the C_L/C_D ratio created for missile performance increases steadily when AoA increases for Mach numbers 1.5, 2 and 2.5, while these values decrease as Mach number increases. In the Spalart-Allmaras turbulence model in Figure 6.30, it is seen that the C_L/C_D value decreases up to 12° AoA at 2.5 Mach.

The k-ω, SST and k-ε, Realizable turbulence models are suitable for solving the near-wall region. The solution of CFD results concluded that the k-ω, SST turbulence model and the k-ε, Realizable turbulence model give similar and sensible results in supersonic flow and high AoA conditions.

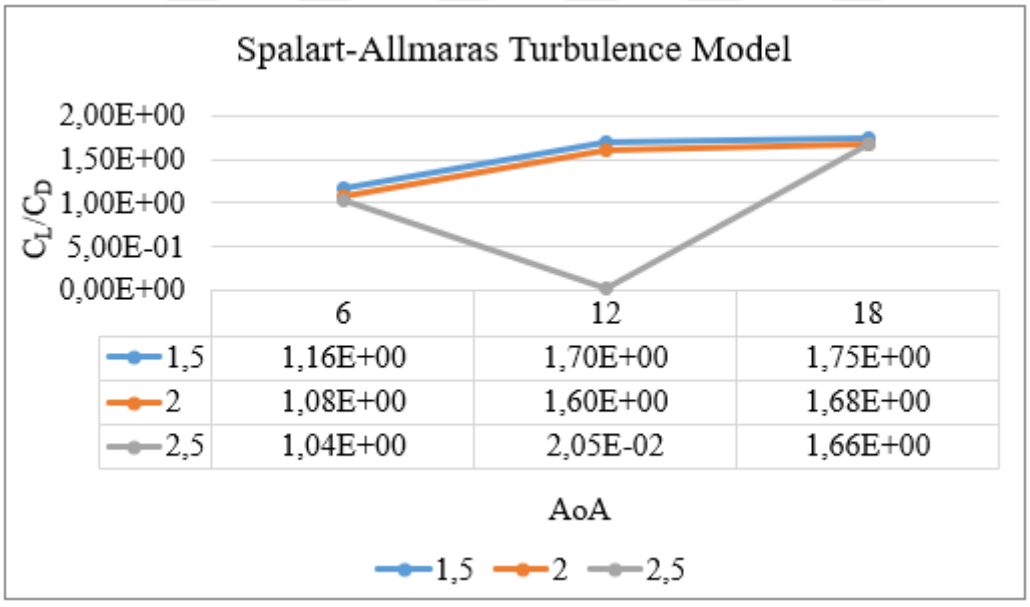


Figure 6.30 C_L/C_D in the Spalart-Allmaras turbulence model for 6°, 12° and 18° AoA at 1.5, 2, 2.5 Mach numbers

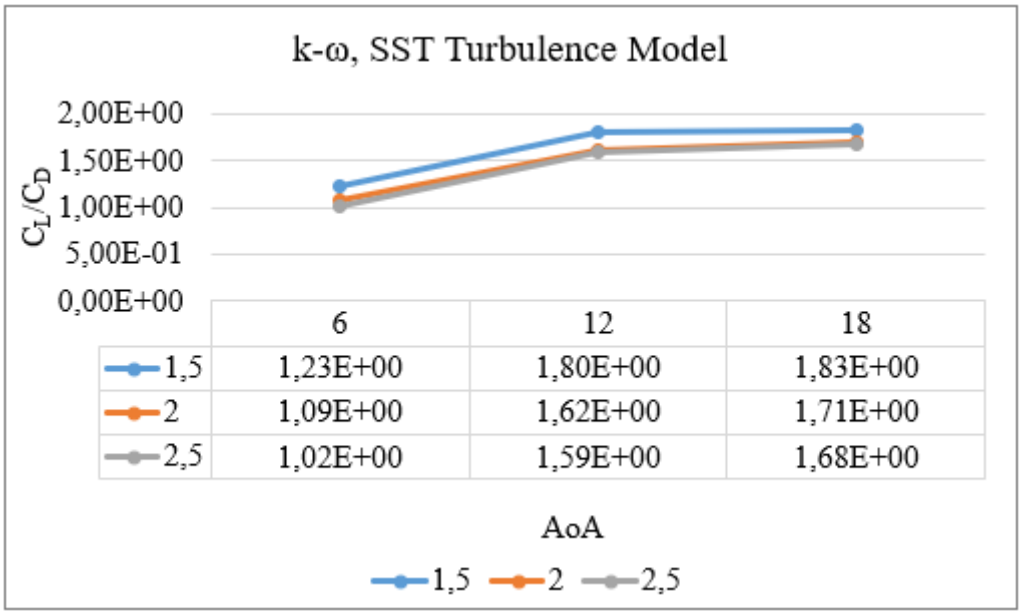


Figure 6.31 C_L/C_D in the k-ω, SST turbulence model for 6°, 12° and 18° AoA at 1.5, 2, 2.5 Mach numbers

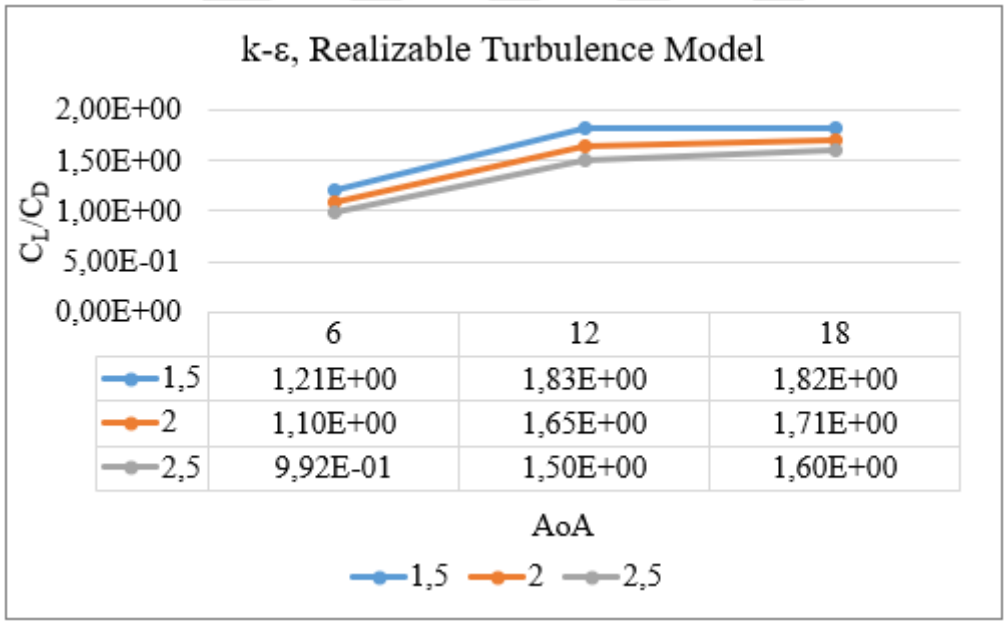


Figure 6.32 C_L/C_D in the k-ε, Realizable turbulence model for 6°, 12° and 18° AoA at 1.5, 2, 2.5 Mach numbers

The Spalart-Allmaras turbulence model (Figure 6.33), the k-ω, SST turbulence model (Figure 6.34) and the k-ε, Realizable turbulence model (Figure 6.35) all illustrate how the missile can move forward when the moment force coefficient is larger than the drag coefficient. The moment coefficient to drag coefficient ratio rises with decreasing Mach number and increasing AoA in each graph.

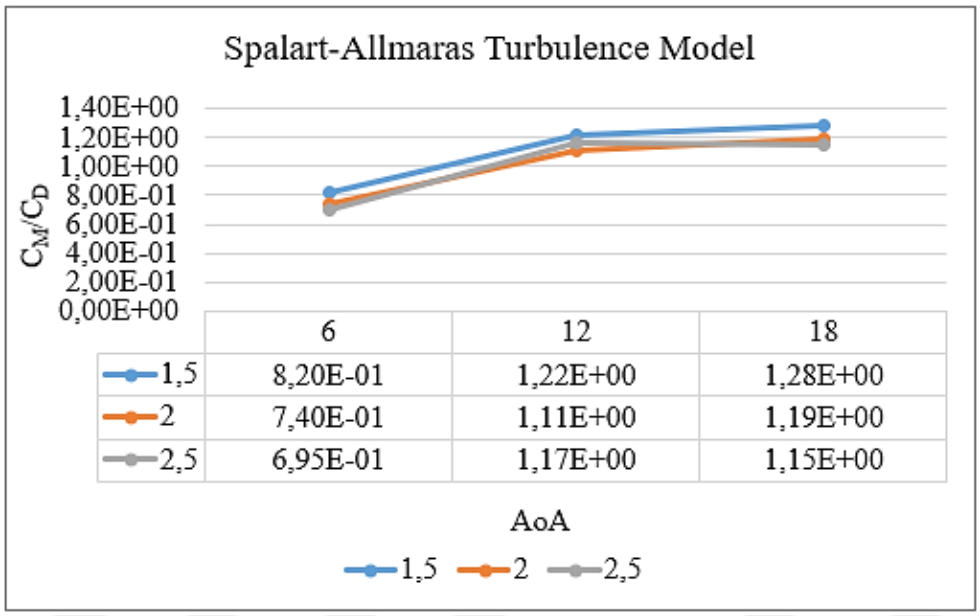


Figure 6.33 C_M/C_D in the Spalart-Allmaras turbulence model for 6°, 12° and 18° AoA at 1.5, 2, 2.5 Mach numbers

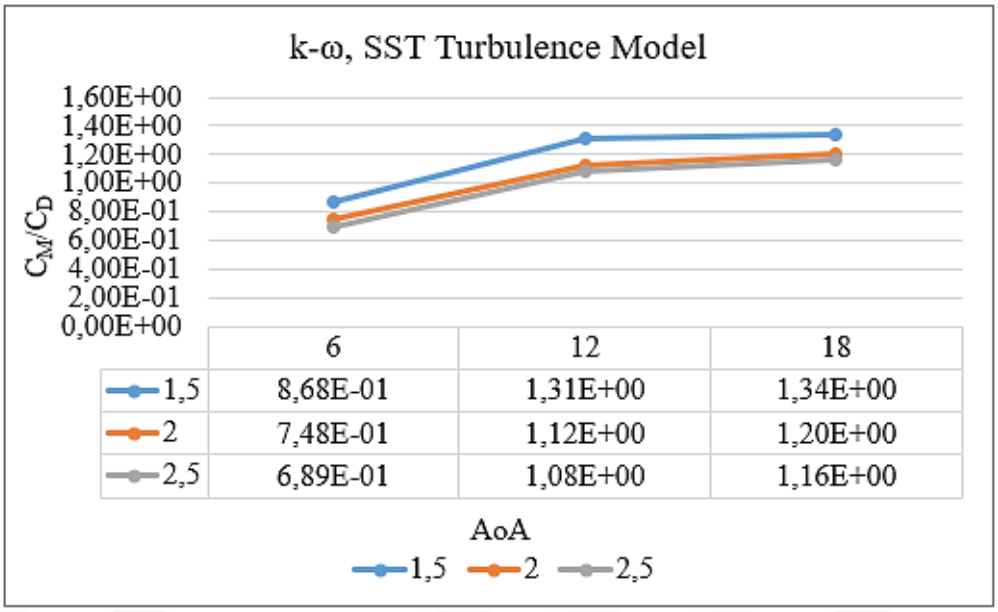


Figure 6.34 C_M/C_D in the k-ω, SST turbulence model for 6°, 12° and 18° AoA at 1.5, 2, 2.5 Mach numbers

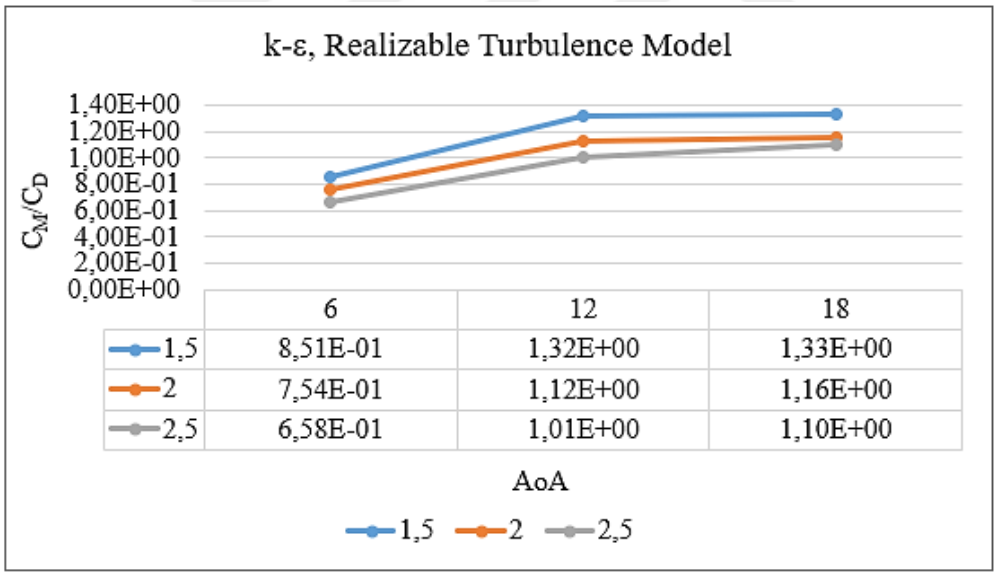


Figure 6.35 C_M/C_D in the k-ε, Realizable turbulence model for 6°, 12° and 18° AoA at 1.5, 2, 2.5 Mach numbers

6.2 Supersonic Nozzle Analysis Results

The solution of CFD results for the nozzle was carried out to observe Mach numbers, Static Pressure and Static Temperature for different throat widths for the k-ω, SST and the k-ε, Realizable turbulence models.

In the solution for 30 mm, 40 mm, 50 mm throat width nozzles, residual values are generated as continuity, x-velocity, y-velocity, energy, k and ω with used k-ω, SST Turbulence model (Figure 6.36) and are generated as x-y velocity, continuity, energy, k and ε for k-ε, Realizable turbulence model (Figure 6.37).

The values converged with the residual values being below 10^{-6} for all data.

In rocket engine design, it is seen that as the nozzle throat width decreases, the Mach number increases with the compression of the air. When the Mach numbers in Figure 6.38, Figure 6.39, Figure 6.40 are compared, nozzles with 30 mm and 40 mm throat widths switch to hypersonic flow. This is undesirable for a supersonic missile. It seems that a nozzle with a throat width of 50 mm is reasonable for both turbulence models in Figure 6.40. For each nozzle is observed transonic field on their throat.

When the temperature contours in Figure 6.41, Figure 6.42 and Figure 6.43 are compared, it is observed that the k-ε, Realizable turbulence model values have higher temperature inputs in the nozzles with 30 mm and 40 mm throat width, although they are solved with the same values, while the temperature input and output in the k-ω, SST turbulence model values are higher in the nozzle with 50 mm throat width.

When the pressure contours in Figure 6.44, Figure 6.45 and Figure 6.46 are compared, the inlet pressures of all nozzles are the same, but the outlet pressures are high in the k-ω, SST turbulence model.

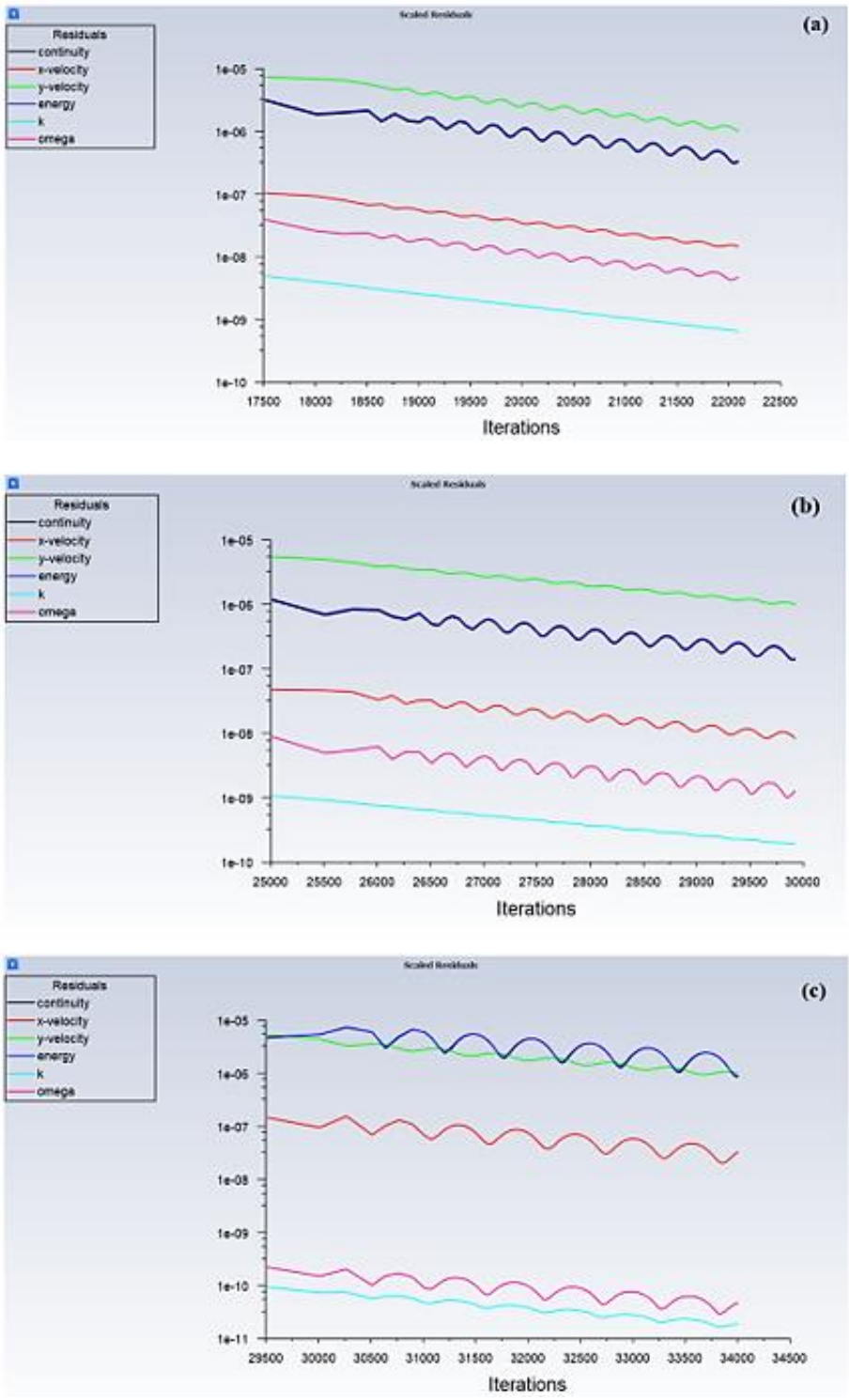


Figure 6.36 Residuals values in the the k-ω, SST turbulence model in nozzle (throat width (mm); a: 30, b: 40, c: 50)

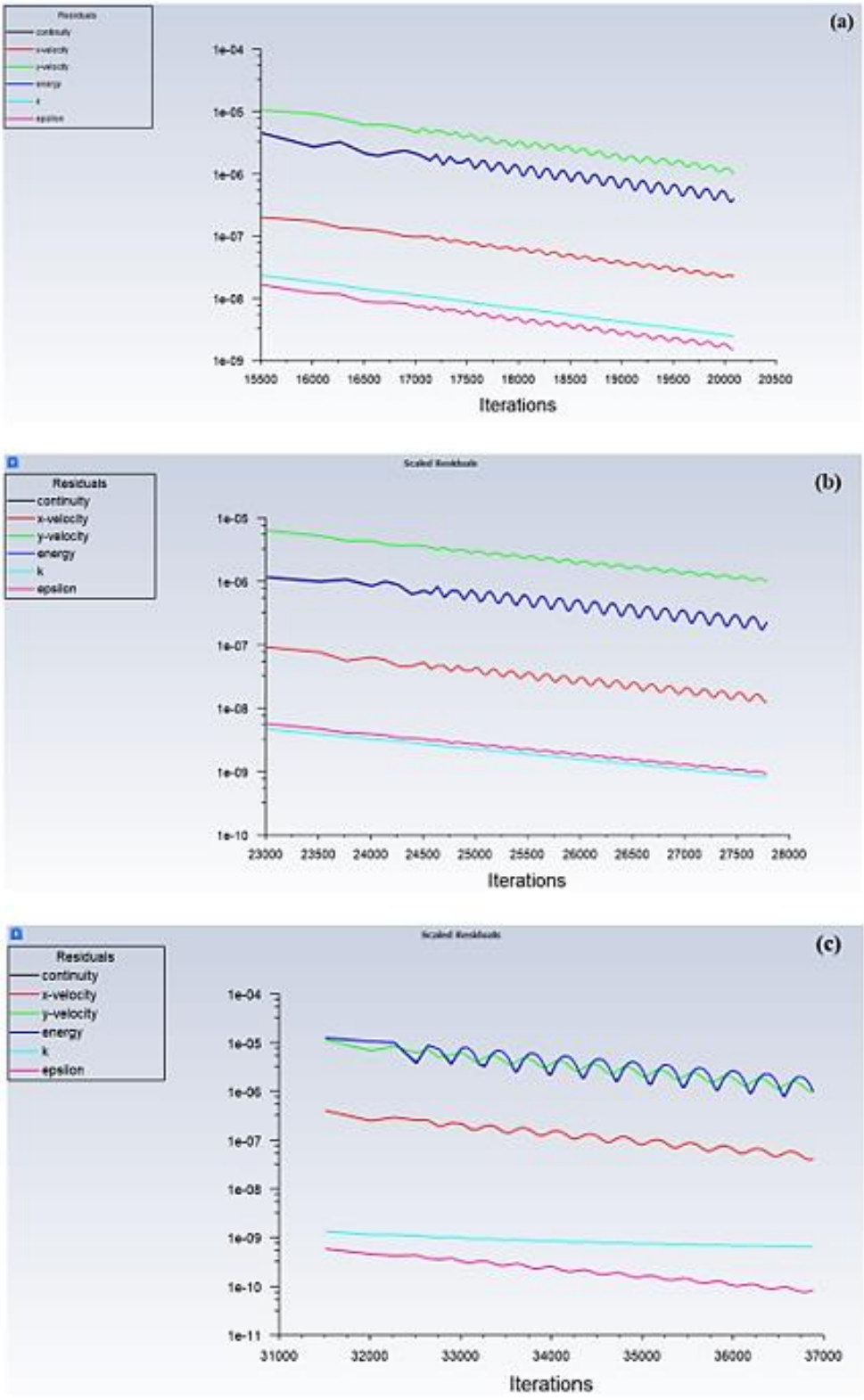


Figure 6.37 Residuals values in the the k-ε, Realizable turbulence model in cone nozzles (throat width (mm); a: 30, b: 40, c: 50)

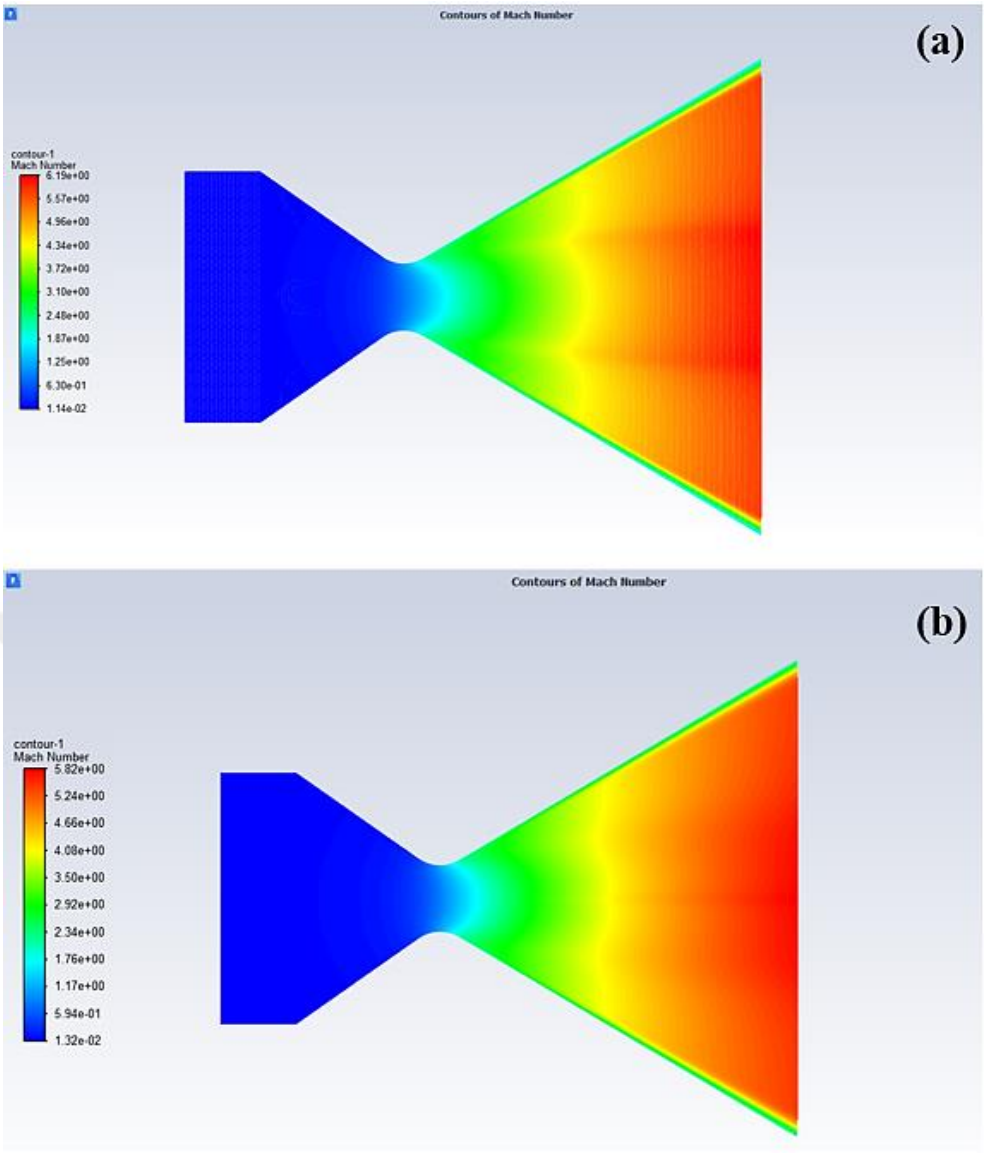


Figure 6.38 Contours of Mach Number in the k-ε, Realizable (a) and k-ω, SST (b) turbulence models in the nozzle with 30 mm throat width

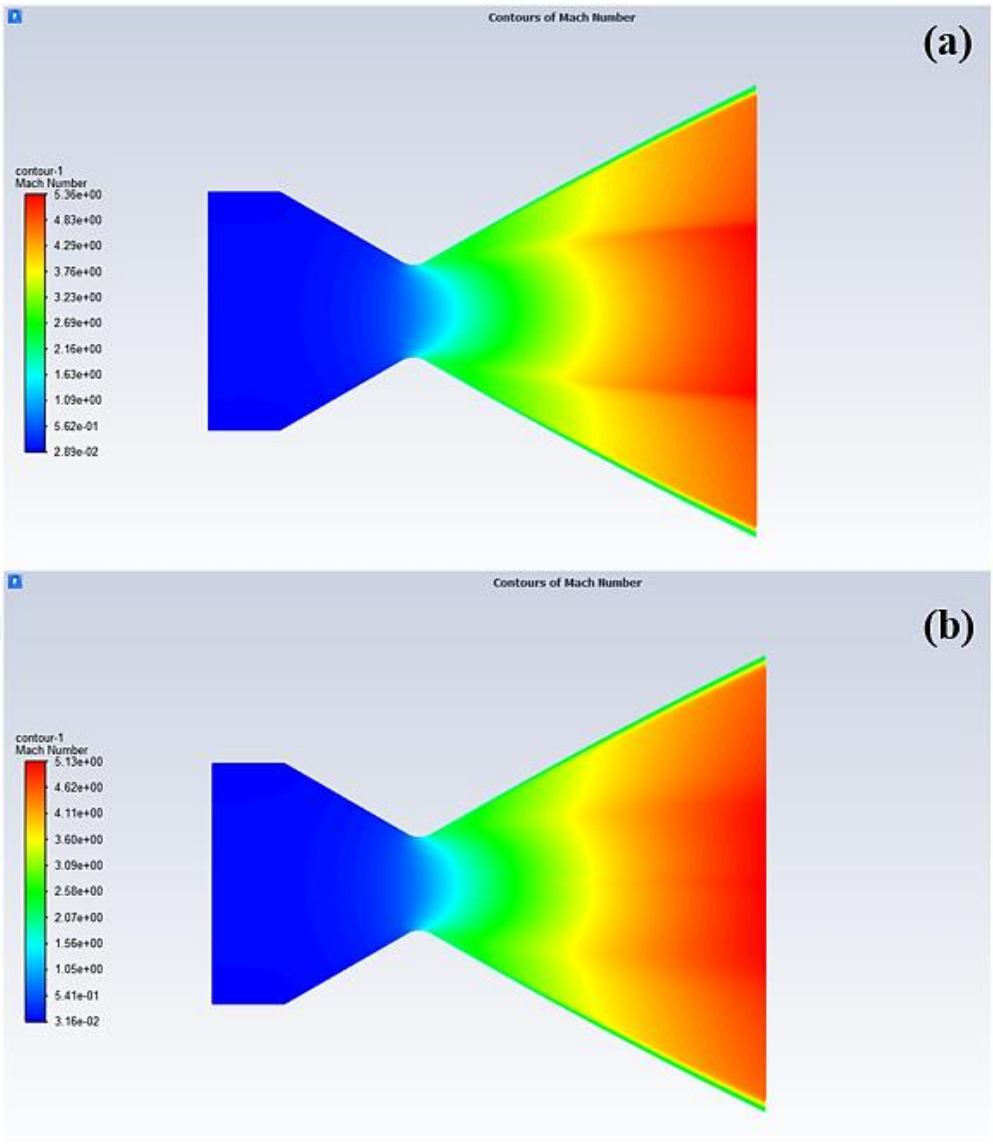


Figure 6.39 Contours of Mach Number in the k-ε, Realizable (a) and k-ω, SST (b) turbulence models in the nozzle with 40 mm throat width

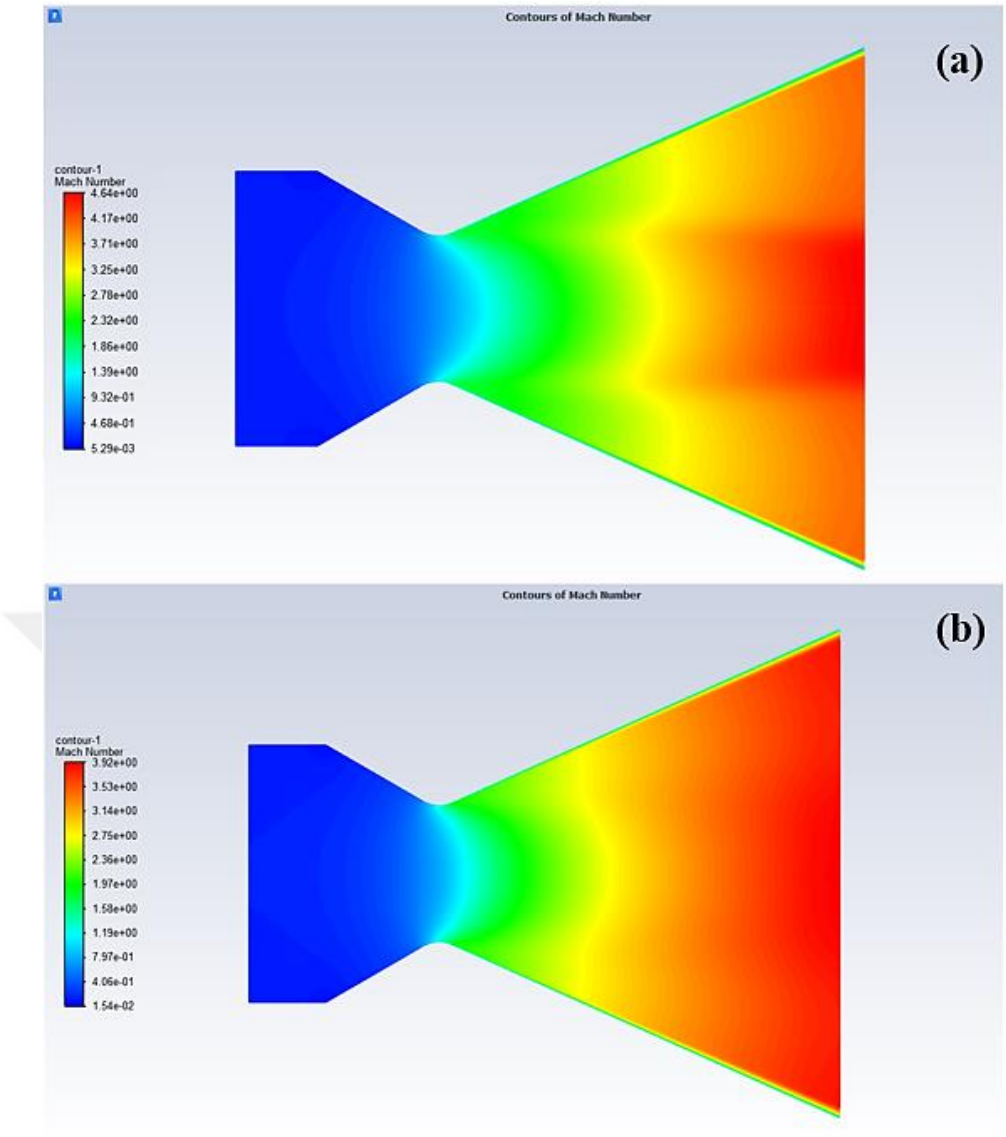


Figure 6.40 Contours of Mach Number in the k-ε, Realizable (a) and k-ω, SST (b) turbulence models in the nozzle with 50 mm throat width

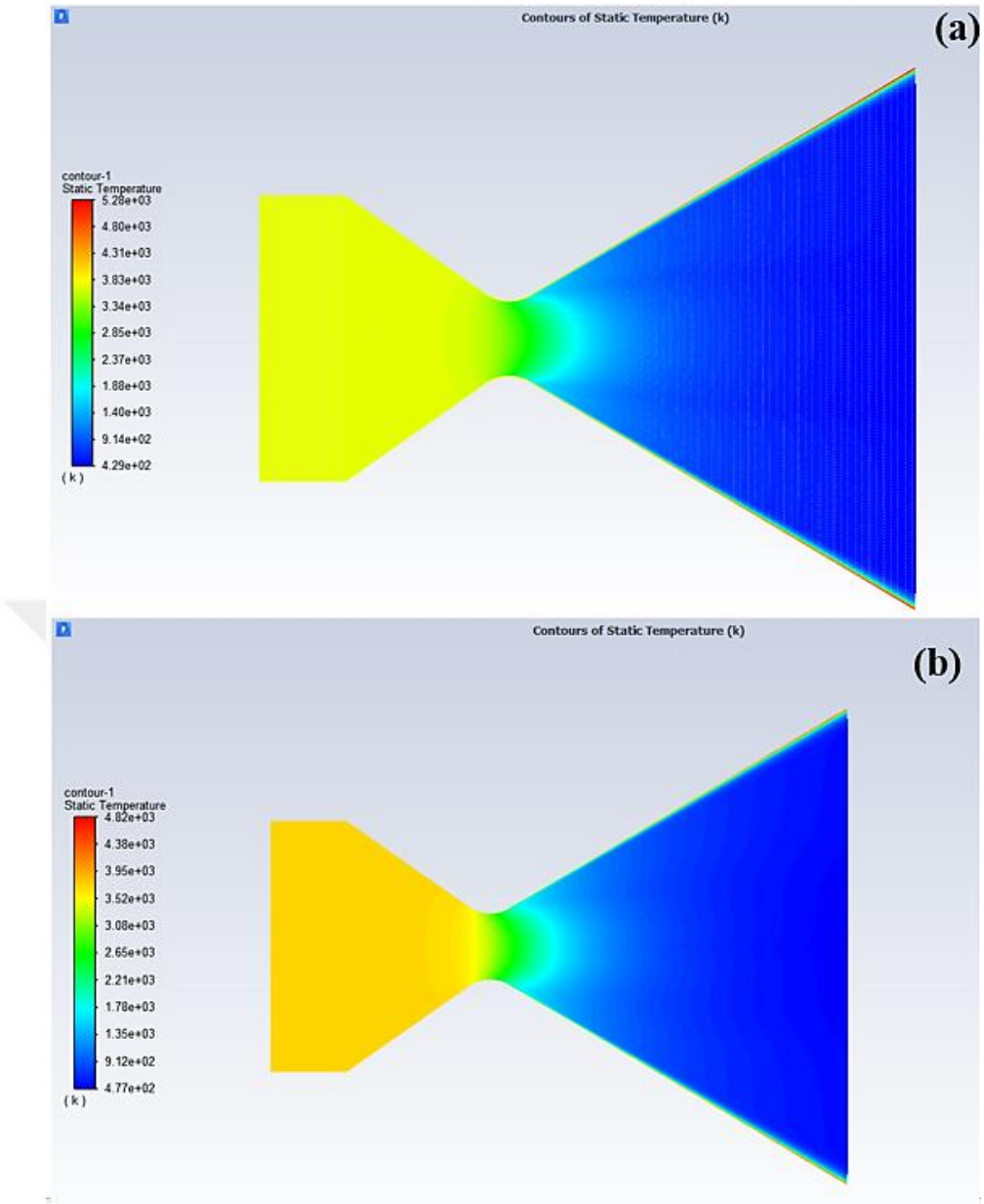


Figure 6.41 Contours of Static Temperature in the k-ε, Realizable (a) and k-ω, SST (b) turbulence models in the nozzle with 30 mm throat width

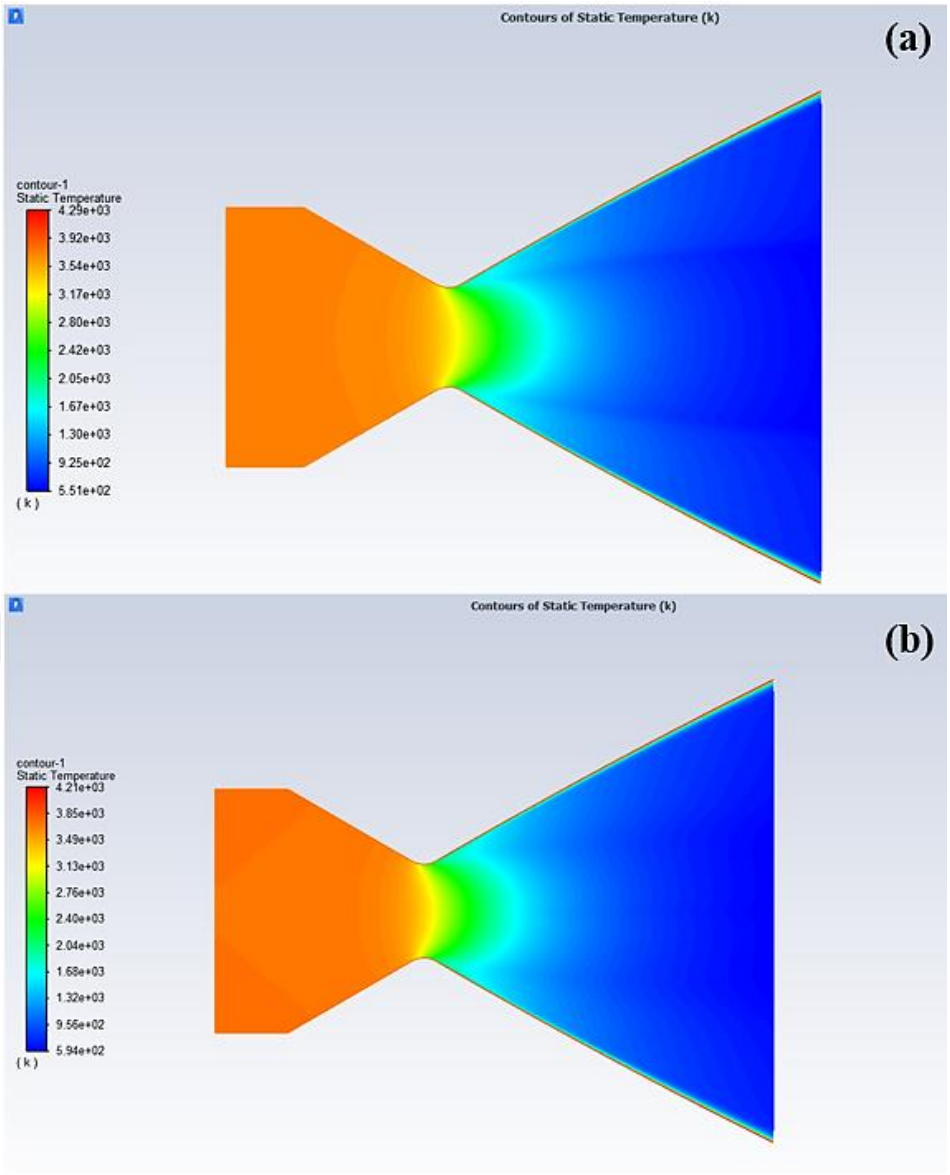


Figure 6.42 Contours of Static Temperature in the k-ε, Realizable (a) and k-ω, SST (b) turbulence models in the nozzle with 40 mm throat width

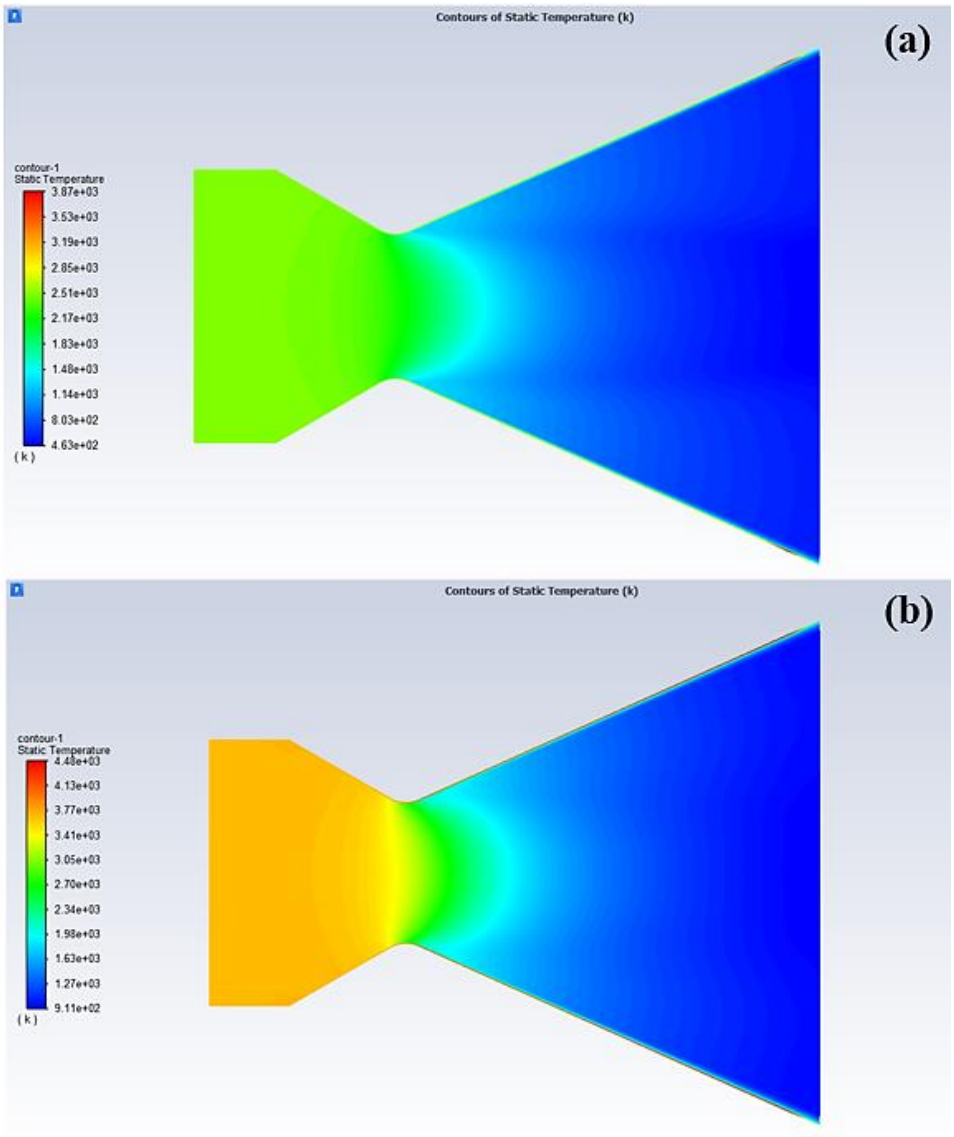


Figure 6.43 Contours of Static Temperature in the k-ε, Realizable (a) and k-ω, SST (b) turbulence models in the nozzle with 50 mm throat width

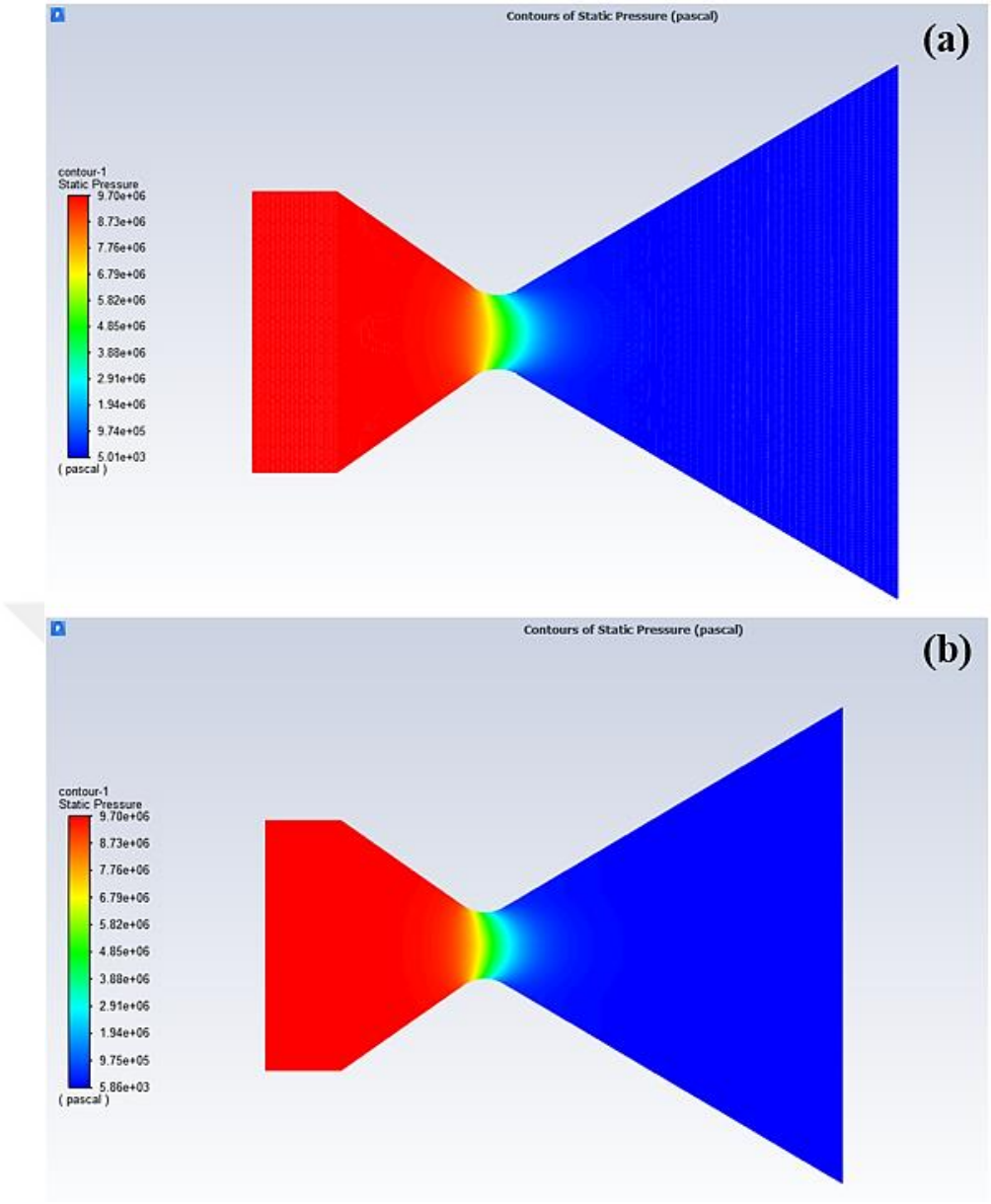


Figure 6.44 Contours of Static Pressure in the k-ε, Realizable (a) and k-ω, SST (b) turbulence models in the nozzle with 30 mm throat width

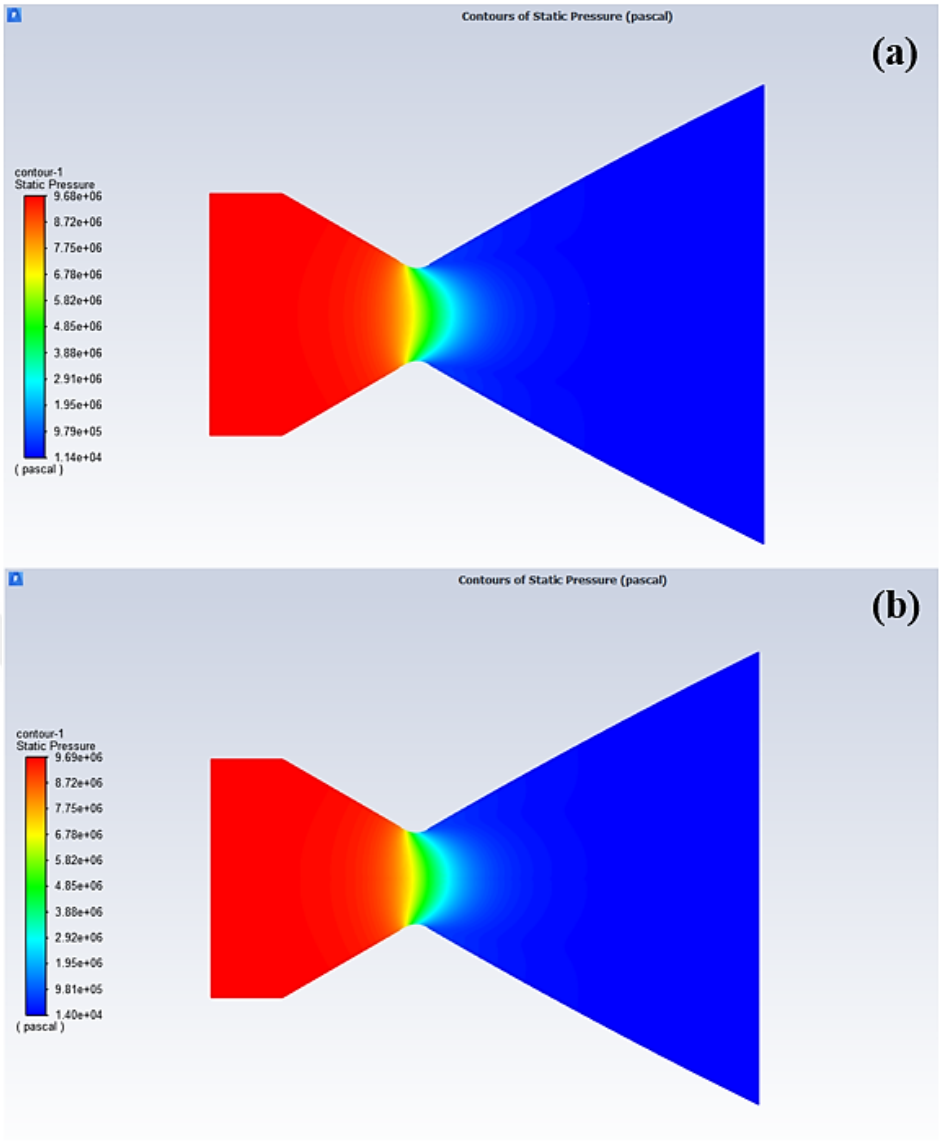


Figure 6.45 Contours of Static Pressure in the k-ε, Realizable (a) and k-ω, SST (b) turbulence models in the nozzle with 40 mm throat width

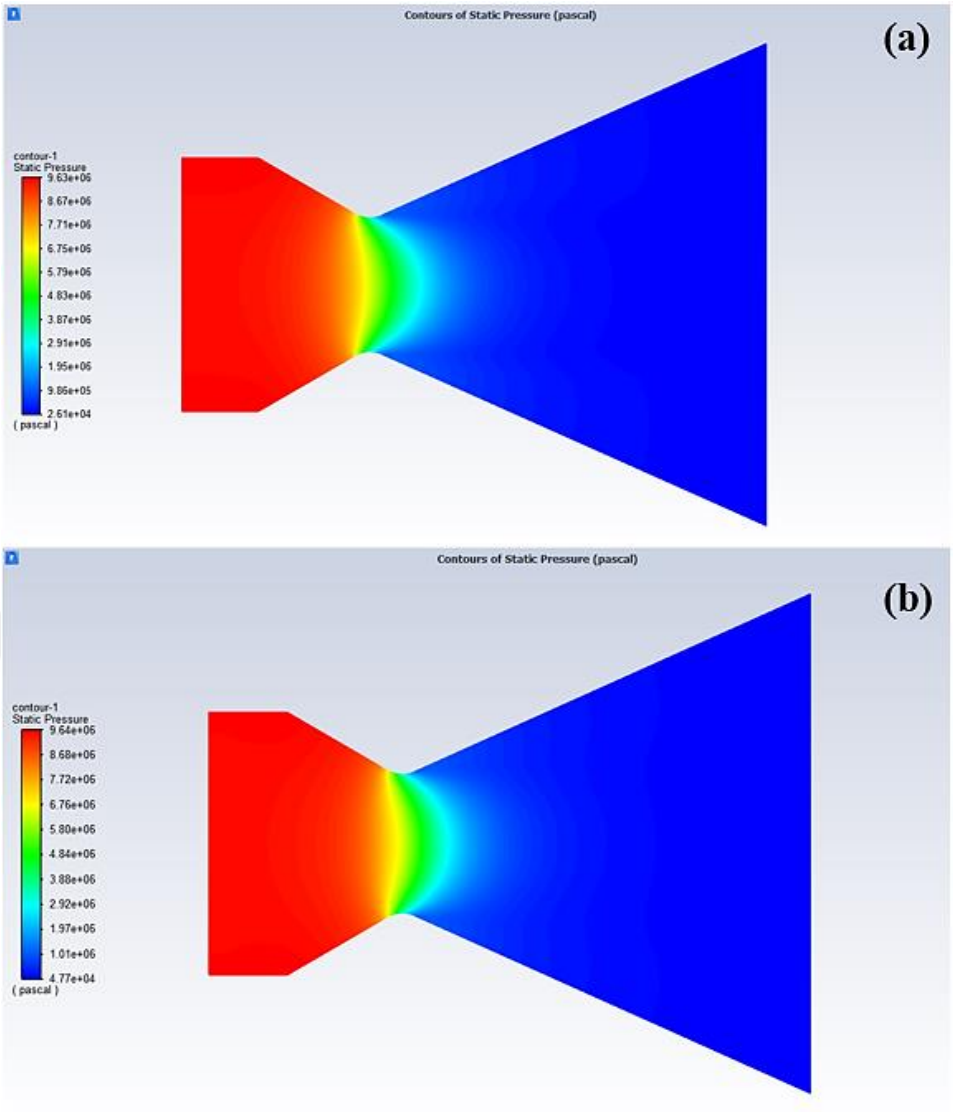


Figure 6.46 Contours of Static Pressure in the k-ε, Realizable (a) and k-ω, SST (b) turbulence models in the nozzle with 50 mm throat width

7
CONCLUSION

This thesis conducted an aerodynamic examination of missiles using a CFD solution, varying the Mach number and turbulence models. The aerodynamic design and CFD analysis of a missile based on the AIM 120 AMRAAM Missile, according to different attack angles and different Mach numbers, to be used in supersonic flows for unmanned aerial vehicles, were carried out.

Using Ansys SpaceClaim, the missile geometry was created at the start of the study, and ANSYS Mesh was used to create a three-dimensional (3D) mesh with hexahedral and tetrahedral structural geometry. For an axi-symmetric misile, between one million and four million mesh elements were created. The friction coefficients on the geometry at 0° AoA were examined in ANSYS Fluent. Between 2.7 million and 3.8 million mesh elements, there was very little variation in the CFD findings of solutions. The mesh element was determined as 2,717,498.

CFD solution was then performed using the Spalart-Allmaras, k-ω, SST and k-ε, Realizable turbulence models. Rocket aerodynamics were studied at 0°, 6°, 12°, 18° AoA for Mach numbers 1.5, 2, 2.5. In addition, C_L to C_D ratio and C_M to C_D ratio were also calculated to display missile performance at high AoA. In missile design analyses, the k-ε, Realizable model and the k-ω, SST model have been used as flow regimes to predict fine-grained meshes with specific local heat transfer or flow separation.

As a first result, although the distributions of C_M/C_D and C_L/C_D ratio graphs in the k-ω, SST turbulence model and the k-ε, Realizable turbulence model gave similar outcomes, it was determined that the k-ω, SST turbulence model that gave the most optimum outcome, since the C_M/C_D and C_L/C_D ratio was expected to be high. When the C_L/C_D ratio are examined which is conducted by Şumnu, Güzelbey and Öğücü in Table 1.1 [1], the results are observed very close according to 18° AoA at the Figure 6.32.

In rocket nozzle design, it is observed that as the nozzle throat width decreases and the air is compressed more, the Mach number increases. It is critical that the Mach

number in the rocket nozzle does not exceed 4.5 Mach. In this study, hypersonic flow was observed in cone nozzles with throat diameters of 30 mm and 40 mm. The cone nozzle with throat diameters of 50 mm was used to perform supersonic flow in accordance with both the k-ε, Realizable turbulence model and the k-ω SST turbulence model, which include the distribution rates of turbulent kinetic energy.

As a second result, the usability of the cone nozzle with 50 mm throat diameter in the supersonic flow regime has been proven by CFD analysis.

REFERENCES

[1] A. Şumnu, İ. H. Güzelbey, and O. Öğücü, "Aerodynamic shape optimization of a missile using a multiobjective genetic algorithm," International Journal of Aerospace Engineering, pp. 1-17, 2020.

[2] Rocket vs. Missile: 2 Important Differences (Complete Guide), https://grammerhow.com/rocket-vs-missile/, 10.10.2023.

[3] B. Srivastava, "Lateral jet control of a supersonic missile-CFD predictions and comparison to force and moment measurements," in 35th Aerospace Sciences Meeting and Exhibit, 1997, pp. 639.

[4] D. López, D. Domínguez, and J. Gonzalo, "Impact of turbulence modelling on external supersonic flow field simulations in rocket aerodynamics," International Journal of Computational Fluid Dynamics, 27(8- 10), pp. 332-341, 2013.

[5] V. K. Shah, K. Ateeb, M. Razzaq, C. Varun, and B. Avinash, "Determination of the optimum nose cone geometrical shape for supersonic missile," Materials Today: Proceedings, 64, pp. 749-754, 2022.

[6] Y. S. Meng, L. Yan, W. Huang, and X. Y. Tong, "Numerical Investigation of the Aerodynamic Characteristics of a Missile," in IOP Conference Series: Materials Science and Engineering (Vol. 887, No. 1, p. 012001), IOP Publishing, 2020.

[7] K. Foelsch, "The analytical design of an axially symmetric laval nozzle for a parallel and uniform jet," Journal of the Aeronautical Sciences, pp. 161-188, 1949.

[8] A. E. Puckett, "Supersonic nozzle design," Journal of Applied Mechanics, 13(4), pp. 265-270, 1946.

[9] B. P. Madhu, G. Mahendramani, and K. Bhaskar, "Numerical analysis on flow properties in convergent–Divergent nozzle for different divergence angle," Materials Today: Proceedings, 45, pp. 207-215, 2021.

[10] R. Ande and V. N. K. Yerraboina, "Numerical investigation on effect of divergent angle in convergent-divergent rocket engine nozzle," Chemical Engineering Transactions, 66, pp. 787-792, 2018.

[11] P. P. Nair, A. Suryan, and H. D. Kim, "Computational study on flow through truncated conical plug nozzle with base bleed," Propulsion and Power Research, 8(2), pp. 108-120, 2019.

[12] A. F. El-Sayed, "Fundamentals of aircraft and rocket propulsion (p. 1010)," London: Springer, 2016.

[13] NASA, Rocket Principles, https://www.grc.nasa.gov/www/k12/rocket/TRCRocket/rocket_principles.html, 03.08.2023.

[14] E. L. Fleeman, "Tactical missile design," Reston: American Institute of Aeronautics and Astronautics, vol. 468, 2006.

[15] SAAB, “IRIS-T short range air-to-air missile.”, https://saab.com/air/ weaponsystems/air-to-air- 193 missile-systems/iris_t/, 02.05.2023.

[16] Raytheon, “AIM-9X Sidewinder Missile.”, https://www.raytheon.com/ capabilities/products/aim-9x, 02.05.2023.

[17] Military.com, “AGM-114 Hellfire.”, https://www.military.com/equipment/ agm-114-hellfire, 02.05.2023.

[18] MBDA Missile Systems, “Brimstone.”, https://www.mbda-systems.com/ airdominance/brimstone/, 02.05.2023.

[19] S. Kumar, “A brief review on Unmanned Combat Aerial Vehicle (UCAV),” Available at SSRN 3593220, 2020.

[20] Raytheon, “AMRAAM Missile.”, https://www.raytheon.com/ capabilities/products/amraam, 02.05.2023.

[21] AIM-7 Sparrow, https://www.globalsecurity.org/military/systems/ munitions/ aim-7.html, 02.05.2022.

[22] Raytheon, “Javelin Weapon System.”, https://www.raytheon.com/ capabilities/products/javelin, 02.05.2022.

[23] Raytheon, “Tomahawk Cruise Missile.”, https://www.raytheon.com/ capabilities/products/tomahawk, 02.05.2022.

[24] L. Pierrot and J. A. Vines, “A Look at Tomorrow's Tactical Air Forces,” Diane Publishing, 1997.

[25] MBDA Missile Systems, “Meteor.”, https://www.mbda-systems.com/air-dominance/meteor/, 02.05.2022.

[26] H. H. Teng and Z. X. Yu, “Analysis of Trajectory of the Projectile Released from Fighter-Aircraft Weapons Bay,” in AIAA AVIATION 2023 Forum, 2023, pp. 4547.

[27] RTX, “AMRAAM Missile.”, https://www.rtx.com/raytheon/what-we-do/air/amraam-missile, 02.05.2022.

[28] Global Defence Corp, “Raytheans’s AIM-120 AMRAAM Slammer”, https://www.globaldefensecorp.com/2020/04/16/raytheons-aim-120-amraam-slammer/, 02.05.2022.

[29] J. N. Nielsen, “Missile aerodynamics-past, present, future,” Journal of Spacecraft and Rockets, 17(3), pp. 165-176, 1980.

[30] R. Nelson, “Flow visualization of high angle of attack vortex wake structures,” in 23rd Aerospace Sciences Meeting, 1985, pp. 102.

[31] E. Wasserstrom, A. Seginer, and Z. Rusak, “Numerical calculation of nonlinear aerodynamics of wing-body configurations,” AIAA Journal, 21(7), pp. 929-936, 1983.

[32] B. Atak, “Slotlu roket/füze modelleri için aerodinamik performans kestirim yöntemlerinin iyileştirilmesi” Doctoral dissertation, Fen Bilimleri Enstitüsü, 2012.

[33] P. Epple, M. Steppert, L. Wunder, and M. Steber, “Verification of torricelli’s efflux equation with the analytical momentum equation and with numerical CFD computations.,” Applied Mechanics and Materials, 871, pp. 220-229, 2017.

[34] L. Rogers, “It's only rocket science: an introduction in plain English,” Springer Science & Business Media, 2008.

[35] D. McLean, “Automatic flight control systems,” Measurement and Control, 36(6), pp. 172-175, 2003.

[36] NASA, “Practical Rocketry”, https://www.grc.nasa.gov/www/k-12/rocket/TRCRocket/practical_rocketry.html, 05.08.2022.

[37] D. A. Shearer and G. L. Vogt, “Rockets: Educator's Guide with Activities in Science, Technology, Engineering and Mathematics,” National Aeronautics and Space Administration (NASA), 2008.

[38] S. Niskanen, “OpenRocket technical documentation,” Development of an Open Source model rocket simulation software, pp. 11-13, 2013.

[39] R. Galejs, “What Barrowman Left Out,” 2018.

[40] O. Dullum, "The rocket artillery reference book," 2010.

[41] R. A. Meyers, “Encyclopedia of physical sciences and technology,” San Diego: Academic Press, 1992.

[42] J. D. Anderson, “Fundamentals of Aerodynamics,” 3rd ed., McGraw-Hill, New York, 2001.

[43] G. P. Sutton and O. Biblarz, “Rocket propulsion elements,” John Wiley & Sons, 2016.

[44] P. A. Bes, “Numerical investigation and flow interactions of a mixed-compression hypersonic inlet,” Doctoral dissertation, Wichita State University, 2014.

[45] H. Schlichting, K. Gersten, H. Schlichting, and K. Gersten, “Exact solutions of the Navier–Stokes equations,” Boundary-Layer Theory, pp. 101- 142, 2017.

[46] U. Piomelli, “Large-eddy simulation: achievements and challenges,” Progress in aerospace sciences, 35(4), pp. 335-362, 1999.

[47] D. C. Wilcox, “Turbulence modeling for CFD,” La Canada, CA: DCW industries, vol. 2, pp. 103-217, 1998.

[48] D. Wilcox, “Turbulence modeling-an overview,” in 39th Aerospace Sciences Meeting and Exhibit, 2001, pp. 724.

[49] B. Baldwin and T. Barth, “A one-equation turbulence transport model for high Reynolds number wall-bounded flows,” in 29th aerospace sciences meeting, 1991 pp. 610.

[50] P. Spalart and S. Allmaras, “A one-equation turbulence model for aerodynamic flows,” in 30th aerospace sciences meeting and exhibit, 1992, pp. 439.

[51] N. C. Markatos, “The mathematical modelling of turbulent flows,” Applied Mathematical Modelling, 10(3), pp. 190-220, 1986.

[52] P. G. Saffman, “A model for inhomogeneous turbulent flow,” Proceedings of the Royal Society of London. A. Mathematical and Physical Sciences, 317(1530), pp. 417-433, 1970.

[53] F. R. Menter, “Two-equation eddy-viscosity turbulence models for engineering applications,” AIAA journal, 32(8), pp. 1598-1605, 1994.

[54] P. Wesseling, “Principles of computational fluid Dynamics,” Springer Science & Business Media, vol. 29, 2009.

[55] F. R. Menter, M. Kuntz, and R. Langtry, “Ten years of industrial experience with the SST turbulence model,” Turbulence, heat and mass transfer, 4(1), pp. 625-632, 2003.

[56] I. Vidanović, D. Cocks, and W. Hofstetter, “Dissipation through localized loss in bosonic systems with long-range interactions,” Physical Review A, 89(5), 053614, 2014.

[57] C. Kopp, “BAe Active Skyflash and AIM-120 AMRAAM,” Australian Aviation, 1994.

[58] Military-Today.com, “AIM-120 AMRAAM Air-to-Air Missile”, https://www.militarytoday.com/missiles/aim120_amraam.html, 02.04.2022.

[59] Volupe, “y+ calculator” https://volupe.se/wall-y-calculator-when-meshing-a-geometry-for-cfd-analysis-this-handy-volupe-calculator-computes-the-height-of-the-first-mesh-cell-off-the-wall-required-to-achieve-a-desired-y-using-flat-plate-boun/, 05.05.2023.

PUBLICATIONS FROM THE THESIS

Conference Papers

1. E. Ç. Kıvrak, Ö. Yücel, and H. Sadıkoğlu, "Aerodynamic Design and Computational Fluid Dynamics (CFD) Analysis of a Supersonic Rocket and Rocket Engine Combustion Chamber," Ankara International Congress on Scientific Research-IX, Ankara/Türkiye, 2023.